ABSTRACT

Title of Dissertation: ESTIMATING SURFACE ELEVATION

BIASES FROM SUBSURFACE SCATTERED

PHOTONS FOR LASER ALTIMETERS

Adam Paul Greeley, Doctor of Philosophy, 2018

Dissertation directed by: Professor James A. Carton
Department of Atmospheric and
Oceanic Science

Three decades of satellite observations have revealed rapid changes in Earth's cryosphere associated with anthropogenic climate change, including decreased extent and volume of Arctic sea ice, mass loss from the Greenland Ice Sheet, mass loss in West Antarctica and the Antarctic Peninsula, and increased outlet glacier discharge in Greenland and Antarctica. NASA's ICESat-2 mission will continue observing these rapid changes by measuring individual photons' round-trip travel times from the satellite to Earth's surface, providing precise estimates of surface elevation, and subsequent mass change for ice sheets and sea ice freeboard in Earth's polar regions. This study investigates the potential bias in ICESat-2 surface elevation estimates from photons that have volume scattered in snow by: (1) measuring the transmission of green light through snow, (2)

developing a method capable of characterizing the effects of volume scattered photons recorded by laser altimeters, (3) applying this method to laboratory measurements of volume scattered photons using the simulation laser altimeter for ICESat-2, and (4) simulating volume scattered photon rage biases using a photon tracking Monte Carlo model.

Transmission measurements show that green light attenuates by one order of magnitude every centimeter in the first four centimeters of snow, suggesting that detecting volume scattered photons originating from laser altimeters is unlikely after photons travel more than a few centimeters in snow. Laboratory measurements using ICESat-2's simulation laser altimeter MABEL (Multiple Altimeter Beam Experimental Lidar), show volume scattered photon return biases of 5 − 10 cm. However, these laboratory measurements revealed a previously unidentified drift in MABEL's ranging on the order of 5 cm, potentially overestimating the volume scattering bias.

Simulations from a single-photon tracking Monte Carlo model developed for this study reveal that approximately 95% of backscattered photons accrue path lengths less than 5 cm. This suggests that while statistically possible for photons to accrue large path lengths, the likelihood of laser altimeters detecting these photons is small.

The results from this work demonstrate that volume scattered photons may be measured by photon counting laser altimeters, but will produce little bias in derived elevation estimates due to their low frequency of measurement.

ESTIMATING SURFACE ELEVATION BIASES FROM SUBSURFACE
SCATTERED PHOTONS FOR LASER ALTIMETERS

by

Adam Paul Greeley

Dissertation submitted to the Faculty of the Graduate School of the
University of Maryland, College Park, in partial fulfillment
of the requirements for the degree of
Doctor of Philosophy
2018

Advisory Committee:

Professor James A. Carton, *Chair*
Professor Sujay Kaushal
Professor Derrick Lampkin
Dr. Thorsten Markus
Dr. Thomas Neumann

Acknowledgements

This dissertation would not have been possible without the help, support, and encouragement of numerous individuals. In particular, my advisors, Tom Neumann, Nathan Kurtz, and Thorsten Markus, have been incredibly supportive and encouraging throughout this entire process, and have made time for discussions that have significantly strengthened this work in the midst of their busy schedules. Thank you also to the as well as the ICESat-2 Project Science Office for supporting this research. While not serving in an official advising capacity, the entire Cryospheric Sciences branch at the NASA Goddard Space Flight Center has been incredible in their openness and willingness to discuss and help with my research. A few individuals were particularly generous with their time and efforts and deserve extra thanks are Mark Shappirio, Bill Cook, Kimberly Casey, and Kelly Brunt.

I also want to thank the Department of Atmospheric and Oceanic Science at the University of Maryland as a whole for their support and help over the past 6 years. I am grateful to my research advisor Jim Carton for exposing me to polar science research and helping guide me toward my current research area, as well as introducing me to Tom Neumann and Thorsten Markus. Additionally, I want to thank Professor Derrick Lampkin for serving on my dissertation committee. His insight and suggestions have improved the quality and strength of this dissertation. As any graduate student in the Department of Atmospheric and Oceanic Sciences knows, Tammy Hendershot is instrumental in any student's ability to navigate the administrative side of a Ph.D. Her assistance throughout this entire process has been

immensely appreciated. My fellow graduate students in the Department of Atmospheric and Oceanic Sciences also deserve thanks for their support and encouragement over the past several years. In particular, Katie Lukens, Allison Ring, and Argie Kavvada have all been supportive and made life as a graduate student fun. I would be remiss if I left out Scott Ozog, who has not only helped me clarify my understanding of lidars, but also helped me keep a balance between research and hobbies over the past several years.

On a more personal note, I want to thank several individuals who have helped me develop as a person and a scientist beyond my official time as a graduate student. Sandra Fary and Michael Turner, both played an important role in exposing me to the scientific method, and fostering my interest in Earth and natural sciences during my primary and secondary education. If not for their patience and passion for teaching science, I would not be doing the work I am today. I would also not be the person or scientist I am today without the support of my parents, who have consistently encouraged me to pursue studies that I enjoy, to persevere in the face of challenge, to explore the world around me, and to ask "why?" without hesitation. Finally, I owe a huge thanks to my wife, Ashley, for her unwavering encouragement over the past few years. Her support and patience over the past several months in particular, has made the realization of this work possible.

Table of Contents

List of Tables

List of Figures

ix

Chapter 1: Introduction

1.1 Background and motivation

Observations over the past three decades show rapid changes associated with anthropogenic climate change occurring in the Earth's cryosphere and that the rate of these changes is increasing. Among these changes are a dramatic decrease in both the spatial extent and total volume of Arctic sea ice (Comiso and Nishio, 2008; Kwok, 2009; Markus et *al.*, 2009), mass loss from the Greenland Ice Sheet (Prichard et *al.*, 2010; Zwally et *al.*, 2011; Ewert et *al.*, 2012; Shepard et *al.*, 2012), warming and mass loss on West Antarctica (Johnson et *al.*, 2008; Rignot, 2008) and the Antarctic Peninsula (Scambos et *al.*, 2000; Holland et *al.*, 2011; Shepherd et *al.*, 2012), and increases in outlet glacier discharge in both Greenland and Antarctica (Scambos et *al.*, 2004; Rignot and Kanagaratnam, 2006; Pritchard and Vaughan, 2007; Rignot, 2008; van den Broeke et *al.*, 2009; Joughin et *al.*, 2010a; Joughin et *al.*, 2010b; Rott et *al.*, 2011). Continued monitoring of these changes at a global, and regional scale is critical to understand the mechanics and processes that drive these changes to reduce uncertainty in the expected impacts.

Space based altimeters provide the ability to measure changes in mass balance for both land and sea ice at global scales. NASA's ICESat (Ice, Cloud and land Elevation Satellite; Schutz et *al.*, 2005) was the first Earth science spaceborne laser altimetry

mission, operating from 2003 to 2009. It provided valuable data and insight into changes in the cryosphere including: rapid mass loss for some outlet glaciers around the margins of the Greenland and Antarctic ice sheets (Pritchard et *al.*, 2009; Zwally et *al.*, 2011); the discovery and mapping of sub-glacial lakes in Antarctica (Fricker et *al.*, 2007; Smith et *al.*, 2009); thinning of grounded tributaries associated with thinning of ice shelves in Antarctica (Prichard et *al.*, 2012); attribution of one third of sea level rise between 2003 and 2009 to mass changes in mountain glaciers and ice caps (Moholdt et *al.*, 2010; Gardner et *al.*, 2011; Gardner et *al.*, 2012; Moholdt et *al.*, 2012; Gardner et *al.*, 2013); and a 0.6 m decrease in Arctic Ocean multiyear sea ice thickness and more than 40% loss of multiyear sea ice (Kwok et *al.*, 2009).

NASA's ICESat-2 mission (Markus et *al.*, 2017), the successor to ICESat, is expected to provide continued observation of these rapid changes, but with improved technology allowing for further advances in our understanding of cryospheric changes. With six laser beams to ICESat's one, ICESat-2 will be able to measure cross-track slope, allowing for separation of slope effects from elevation changes on an orbit-by-orbit basis. ICESat-2 will also provide increased and more detailed along track sampling with a ~15 m laser footprint compared to ICESat's 70m, and a sampling rate of 10 kHz resulting in laser pulses every 0.7 m at the surface in contrast to ICESat's 170m surface pulse separation. Additionally, ICESat-2 will be the first time a spaceborne visible wavelength laser altimeter will use single-photon detection as the primary means of ranging for estimating elevation changes in Earth's surface.

With these advances come new challenges. Unlike ICESat's 1064 nm wavelength laser, for which any surface penetrating photons were quickly absorbed by snow and ice, ICESat-2's 532 nm photons will be weakly absorbed by snow and ice and may result in photons not scattered directly off the surface traveling significant distances in snow and ice before scattering out and back to detection systems. This volume scattering would delay the arrival of photons relative to photons scattered directly from the surface and produce a bias toward lower elevation estimates if not accounted for in surface elevation retrieval algorithms. Understanding how 532 nm wavelength photons scatter within snow and ice, and how often these sub-surface scattered photons are detected by altimeter systems, is therefore necessary to produce accurate and precise surface elevation measurements and subsequent estimations of mass changes for ice sheet mass and sea ice freeboard.

1.2 Dissertation organization and synopsis

This dissertation focuses on understanding how individual photons travel through snow and how they are detected by photon counting laser altimeter systems. This is addressed through the following steps: (1) measuring the transmission of green light through snow and its dependence on snow depth and snow grain size, (2) identifying a suitable method for characterizing the shape of laser pulses from altimeters so that the effect of volume-scattered photons can be identified and quantified in photon returns, (3) measuring photon returns from a laser altimeter in a laboratory so the effect of volume-scattered photons can be isolated, and (4) modeling the paths of

individual photons in snow to quantify their path lengths, their physical depth within the snow, and the frequency with which they are measured by laser altimeters.

Chapter 2 examines the transmission of 543 nm green laser light through snow, and its dependence on snow grain size, in a laboratory setting. I also quantify light absorbing impurity concentrations in our snow. Attenuation of light in the snow depends on snow grain size, particularly below 7 cm snow depth, where smaller snow grains attenuate light more than larger snow grains. The results show that green light attenuates approximately one order of magnitude per centimeter in the top four centimeters of snow, and approximately one order of magnitude every two centimeters below four centimeters, depending on snow grain size. This suggests that photons transmitted by laser altimeters that enter snow are unlikely to travel more than a few centimeters and return to the instrument.

Chapter 3 assesses the limitations of using histograms to characterize the pulse shapes of laser altimeters, and proposes a more robust method to describe MABEL's impulse response using an exponentially-modified Gaussian distribution. I also provide standard error estimates for arithmetic mean and standard deviation calculations, and for exponentially-modified Gaussian parameters using a Monte Carlo sensitivity analysis. I go on to analyze photon returns from a sea ice lead as a case study for estimating precision uncertainty associated with sample size for the arithmetic mean and standard deviation, and for the exponentially-modified Gaussian parameters. I use these estimates of precision uncertainty to calculate the minimum number of photons

required to find both Gaussian and exponentially-modified Gaussian distribution parameters with 1-sigma uncertainty within 3 cm of the parent population values.

In chapter 4, I make laboratory measurements using MABEL (Multiple Altimeter Beam Experimental Lidar) to explore the effect of volume scattering of green light photons by measuring photon returns from snow. Comparing these photon returns to those from a Spectralon reflectance standard allows me to isolate the effect of volume-scattered photons on MABEL's pulse shape. I also use several different snow grain size distributions to ascertain if volume scattering within snow is affected by the snow grain size. These measurements indicate that the effect of volume-scattered photons measurably affects MABEL's pulse shape and causes it to shift between 5 cm and 11 cm away from the altimeter indicating a range bias. I also measure the time-varying stability of MABEL's pulse shape and find that there is significant drift in location parameters, such as the arithmetic mean and the exponentially-modified Gaussian mu parameter, up to approximately 5 cm.

Chapter 5 uses Monte Carlo model simulations of individual photons to determine the path length distribution of photons that are backscattered out of snow and thus able to be received by a laser altimeter system such as MABEL. The model takes into account such parameters as snow grain size, the scattering phase function for snow, and light absorbing impurity concentrations in the snow. The model is able to reproduce transmission measurements similar to the laboratory measurements made in chapter 2, providing confidence that the scattering processes within the model are

realistic. The backscattered photon path length distributions show that while it is possible for backscattered photons to accrue path lengths greater than 1 m, nearly all have much shorter path lengths of up to 10 cm. Additionally, while some photons are able to travel several centimeters into the snow, the overwhelming majority only scatter within the first 1 to 2 cm before being scattered out of the snow. For laser altimeter systems like ATLAS (Advanced Topographic Laser Altimeter System) on ICESat-2, which are expected to measure approximately 10 photons from snow surfaces, this suggests that on average one of these photons may be expected to have been volume-scattered, but that it will most likely have a path length of a few centimeters and have come from the top 1 to 2 cm of snow. This suggests the effect of volume-scattered photons will be minimal, and will most likely impart less than a centimeter of bias to surface elevation estimates.

In summary, this work demonstrates that the effect of volume-scattered photons on elevation estimates using a photon counting laser altimeter will not produce a significant effect on elevation estimates on a shot-by-shot basis. In most cases, the effects of surface roughness and surface slope will mask any bias resulting from volume-scattered photons. For very flat and smooth snow surfaces, it may be possible to aggregate enough photons to observe the effects of volume scattering. Given enough volume-scattered photons, characterization of snow grain size may be possible.

Chapter 2: Transmission of Visible Wavelength Light Through Snow

2.1 Introduction

The deployment of the ATLAS (Advanced Topographic Laser Altimeter System) instrument on ICESat-2 (Ice Cloud and land Elevation Satellite-2; Markus and others, 2017) will bring new opportunities, as well as challenges to the interpretation of spaceborne laser altimetry. In contrast to the 1064 nm waveform ranging laser of its predecessor, ICESat's GLAS (Geoscience Laser Altimeter System), ATLAS will use photon counting and a green laser (532 nm) to measure elevation changes in ice sheets, glaciers, and sea ice by ranging from the satellite to the Earth's surface. In contrast to 1064 nm photons, which are strongly absorbed by snow and ice, 532 nm photons are only weakly absorbed. This weak absorption at 532 nm could result in photons from ATLAS not scattered directly off the surface, to travel significant distances in snow and ice before scattering out and back to detection systems. This volume scattering delays the arrival of photons relative to photons scattered directly from the surface. This could produce a bias toward lower elevation estimates if not accounted for in surface elevation retrieval algorithms. Understanding how 532 nm wavelength photons scatter within snow and ice, and how often these sub-surface scattered photons are detected by altimeter systems, is necessary to produce accurate and precise surface elevation measurement.

Transmission of light through snow and ice is one of the fundamental properties for understanding how photons scatter within snow and ice. While snow albedo in the visible spectrum has been analyzed and discussed extensively (Bohren and Barkstrom, 1974; Grenfell and Maykut, 1977; Wiscombe and Warren, 1980; Warren, 1982), transmission of visible spectrum radiation through snow and its dependence on grain size has been less comprehensively studied. Several studies have explored the transmission properties of snow in the field (Warren and others, 2006; Perovich, 2007). These methods are well suited for measuring transmission through naturally deposited snow, but not for isolating the factors that may influence transmission, such as snow grain size. Studies such as Sergent and others (1987) have analyzed the transmission of snow in a laboratory environment, but like field studies, don't control for the effect of snow grain size. This paper explores the role of grain size on the total transmission and scattering of 532 nm light in snow in a controlled laboratory setting. In this paper, we define narrow-beam attenuation as the measurement of radiant flux loss from a narrow, collimated beam due to absorption and scattering while passing through snow; we use this term interchangeably with 'attenuation.' We present transmission profiles for several grain size distributions, calculate narrow-beam attenuation coefficients from these measurements, and discuss the effect of grain size on transmission of visible light through snow. We also spectrally quantify the optically absorbing impurity load in our snow samples, as this also influences the transmission of light in snow. The results from this study will be useful in assessing the degree to which photons from laser altimeter systems scatter within snow before reemerging, the associated implications for snow and ice surface elevation estimates,

9

and the potential for coincident estimation of surface snow grain size from returned photons.

2.2 Methods

Our goal was to measure the transmitted intensity of green light from a laser through snow at various depths, and use these intensities to calculate the depth-dependent attenuation. We also evaluated the dependence of attenuation on snow grain size by making several intensity measurements with different grain size distributions. To prevent melting, we kept the snow sample at sub-zero temperatures while measurements were taken. The SIRF (Snow and Ice Research Facility) at NASA's Goddard Space Flight Center contains a walk-in freezer with a hatch (a small door in the wall of the freezer), which allowed us to maintain the necessary temperature-controlled environment for the snow samples, as well as a room-temperature environment for the electronic and optical equipment used in the experiment. The overall experimental design is depicted in Figure 2.1.
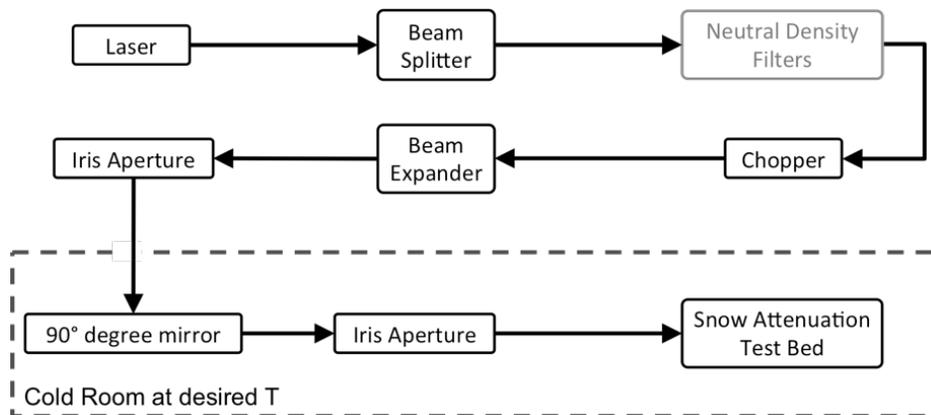
Figure 2.1: Experiment schematic

10

2.2.1 Optical Bench and Test Bed Design

While ATLAS uses a 532 nm laser, we used a readily available continuous wave He-Ne 543 nm laser, which has sufficiently similar optical properties for snow as 532 nm (Grenfell and Maykut, 1977; Nolin and Dozier, 1993), as the green light source for our experiment. We turned off the ambient lighting while taking measurements to reduce the potential for light from other sources affecting our results. The laser beam in our experimental set up first passed through a beam splitter to pick off part of the beam to monitor the transmitted laser power. The primary beam then passed through a chopper wheel connected to a lock-in amplifier, which we used to measure light intensity. The chopper wheel allowed us to make low intensity measurements more accurately by allowing the amplifier to reject any discrete frequencies or noise voltages not equal to the reference frequency produced by the chopper wheel. After the chopper wheel, the primary beam passed through a beam expander to increase the beam diameter from approximately one millimeter to two centimeters. Following the beam expander, an iris aperture trimmed the edges of the expanded beam, yielding a one-and-a-half-centimeter diameter trimmed beam with approximately uniform intensity across its width. Expanding the beam ensured it was larger than a single snow grain, thereby preventing "shadowing" of adjacent snow grains from the laser beam, which would produce a less diffuse scattering of light within the snow sample.

At this point, the laser beam left the optical bench outside the cold room and passed into the freezer via the hatch. The freezer's internal temperature was held at -15°C, +/- 1°C. We placed a Styrofoam board across the hatch to reduce airflow into the

freezer and allow the laser beam to pass into the freezer through a four-centimeter diameter hole. Once in the freezer, the laser reflected off a 90° tilt mirror to change orientation from horizontal (parallel to the ground) to vertical so that the beam was normal to the snow surface. A final iris aperture after the tilt mirror created a circular beam with a final diameter of 1.1 cm.

We designed the test bed that held the snow sample as a piston. It consisted of a cardboard tube with an interior radius of 10.16 cm and a wooden disk inside the tube. However, unlike a typical piston where the disk moves within a stationary cylinder, we designed the cylinder to move relative to the stationary disk. We mounted three solid-state photo-diode detectors (each with an active light detection area of 3.6 mm by 3.6 mm square) into the wood disk: the first directly in the center, the second 1/3rd the radius of the disk from the center (3.3 cm from the center), and the third 2/3rd the radius (6.6 cm) of the disk from the center. We increased the depth of snow the laser beam passed through before reaching a detector by moving the tube up, adding more snow, and leveling the snow at the rim of the tube. A depth scale next to the cardboard tube measured the depth of the snow with an accuracy of ±0.5 mm. All surfaces within the tube, including the wooden disk, were painted black to reduce scattering off the cylinder walls and simplify boundary conditions.

For transmission measurements with relatively little snow above the detectors, a neutral density filter was placed in the laser beam path (after passing through the beam splitter) to prevent saturation of the detectors. The detectors produced a voltage

proportional to the intensity of incident light. The lock-in amplifier measured this voltage, which was subsequently recorded by a data logger. In addition to recording the voltages from the detectors under snow, the data logger also recorded the air temperature 3 cm above the snow sample, and the voltage from the detector monitoring laser power outside the freezer. We measured light intensity at a given depth for at least four minutes with the data logger recording values every 0.4 seconds. This resulted in at least 500 values of detector voltage per depth, which reduced the effect of noise in our measurement system.

2.2.2 Snow Physical Properties

Our snow was originally collected at Summit, Greenland in 2008 and used to pack ice cores for transport to the United States. Separating the snow into different grain size distributions involved "de-sintering" the snow first. After sitting for extended periods of time (i.e., more than two weeks), the snow sintered and was not easily broken apart into individual grains. We found that the finest grating on a standard household box cheese grater was exceptionally efficient at returning sintered and aggregated snow to individual snow grains (Figure 2.2).
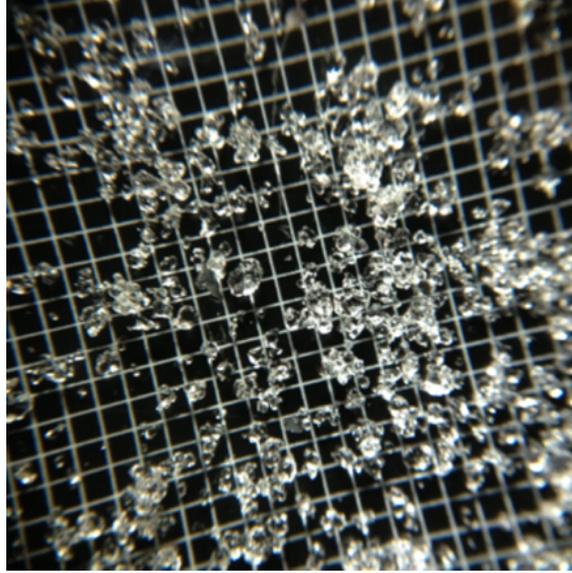
Figure 2.2: Individual snow grains after passing through a standard box cheese grater to break up aggregated snow grains. The white lines in the background are 1 mm grids on a snow classification card.

Once de-sintered, the snow was placed on a vertical stack of Gilson geological sieves (brass frame with stainless steel woven wire mesh) with the following mesh openings (from top to bottom): 2.0 mm, 1.4 mm, 1.0 mm, and 0.5 mm. The sieves did not undergo treated to clean them prior to use. The distributions of snow grain diameters with short names are shown in Table 2.1.

Table 2.1: Snow grain diameters in a sieved distribution with associated short name, minimum and maximum mesh openings used for sieving each snow grain distribution, and the associated SSA

Distribution short name	Minimum diameter (mm)	Maximum diameter (mm)	Minimum diameter SSA $(m^2 \cdot kg^{-1})$	Maximum diameter SSA $(m^2 \cdot kg^{-1})$
small	0	0.5	0	5.5
medium	0.5	1.0	5.5	2.8
large	1.0	1.4	2.8	2.0
unseparated	0	2.0	0	1.4

14

While the minimum diameter for the small snow grain distribution is given as zero, the vast majority of snow grains have diameters between 0.3 and 0.5 mm. Sieving the small snow grain distribution through a 0.3 mm grating yielded very little snow with diameters smaller than 0.3 mm. As such, we decided it was sufficient to leave all snow grains with diameters less than 0.5 mm together in one distribution. Snow and ice chunks larger than 2.0 mm were not used for our experiments. The sieved snow was stored in plastic bags within cardboard boxes in the cold room. Snow stored in the sealed boxes began undergoing noticeable radius of curvature metamorphosis (Colbeck, 1983; Colbeck, 1987) after approximately two weeks. As a result, we re-sieved the snow every two weeks to minimize the effect of snow metamorphosis and ensure the snow grain size distributions remained consistent during transmission measurements.

In addition to physically separating our snow into the grain size distributions listed in Table 1, we also calculate the specific surface area (SSA) to simplify comparisons of our work with other studies that use SSA to quantify *in situ* measurements of snow grain size. Grenfell and Warren (1999) present a method to represent non-spherical ice particles as a collection of independent spheres (their equation 7) by converting the geometric mean radius of infinite cylindrical ice crystals to an area-weighted "effective radius" (r_{eff}):

$$r_{eff} \; = \; r_g exp^{2.5 ln(\sigma_g)^2} \quad \text{or} \quad r_{eff} \; = \; 1.737 r_g \qquad (2.1)$$

where r_g is the geometric mean radius for a cylindrical snow crystal, σ_g is the fixed geometric standard deviation corresponding to the value "typically obtained for the size distributions (when converted to equal-volume/area spheres) which we [Grenfell and Warren] measured in photographs of falling ice crystals collected on 100 days in the winter of 1992 at the South Pole…". Since our snow is old and heavily metamorphosed, the snow grains are more rounded and spherical than cylindrical. As such, we propose calculating the effective snow grain radius (r_{eff}) with an adjusted value for the fixed geometric standard deviation (σ_g) of 1.3; halfway between the value for cylindrical crystals and a sphere. The formula for calculating the effective radius then becomes:

$$r_{eff} \;=\; 1.188 r_g \tag{2.2}$$

Gallet and others (2009) present a method (their equation 1) for converting effective snow grain size to SSA:

$$SSA \;=\; \frac{6}{\rho_{ice} d_{eff}} \tag{2.3}$$

where ρ_{ice} is the density of ice (917 kg·m^{-3} at 0°C) and d_{eff} is the effective diameter of the sphere. Using these two equations we convert the minimum and maximum bounds of our snow grain distributions to SSA in Table 2.1.

We added snow to the volume between the wooden disk and the walls of the tube by sieving loose snow above the test bed using the 2.0 mm spaced sieve. This ensured any remaining grain clusters or ice chunks did not enter the test bed. Using a straight edge, we leveled the surface of the snow to the top of the cardboard tube. Once transmission measurements were completed, the snow density was measured using a snow density probe near the top and bottom of the snow. After several consecutive transmission and associated density measurements, we determined that snow density did not change detectably each time snow was put in the test bed (Figure 2.5). As a result, we did not measure snow density following every transmission measurement, but ensured each grain size distribution had at least two density measurements.

To organize our transmission measurements, we grouped a series of intensity measurements made at successively deeper snow depths (e.g., from a depth of 0 cm (no snow) to 10 cm, at 1 cm intervals) into a transmission "profile." Light intensity was measured at increasing depths until we either ran out of snow to add to the test bed, or the system noise exceeded the intensity signal in the lock-in amplifier. We measured at least three transmission profiles for each grain size to account for any variations in the snow as it was sieved into the test bed (see Appendix for more details).

2.2.3 Impurities in Snow

While the snow remained visibly clean throughout the experiments, trace element protective gear was not used during collection or use of the snow. To qualitatively assess the impurity loading in the snow used for our measurements, we measured the surface reflectance of the snow using a (350 - 2500 nm) Analytical Spectral Device (ASD) portable field spectroradiometer. Since nominal clear-sky conditions outdoors in Maryland would typically cause the snow to melt rapidly, we made snow reflectance measurements in the SIRF. We did, however, collect a series of snow reflectance measurements outdoors using the sun for illumination (not shown here) to compare to our SIRF measurements. In addition, we quantitatively assess our snow's optically absorbing impurity load by filtering melted snow, and comparing the spectral transmission of these filters against those from calibrated filters to estimate the equivalent black carbon (BC) concentration present in our snow grain distributions.

2.2.3.1 ASD Measurements

The ASD measured snow surface radiance from the snow surface over wavelengths from 350-2500nm (visible (Vis), near-infrared (NIR), and short-wave infrared (SWIR)). The field spectroradiometer's fiber optic contains nineteen 100-micron fibers for the Vis and NIR, nineteen 200-micron fibers for the SWIR (1001-1830 nm), and nineteen 200-micron fibers for the SWIR2 (1831-2500), which are randomly distributed in the fiber optic bundle. To simulate solar illumination, we used a

broadband light source to illuminate the snow while collecting reflectance measurements. When placing the fiber optic bundle above a target surface, we positioned the light source to avoid surface shading from the fiber bundle. We placed 10 cm of snow in the same test bed used for transmission measurements while acquiring surface reflectance measurements. A 12" x 12", calibrated, lossless, diffuse Spectralon reflectance standard was placed at the same height immediately next to the snow sample to ensure an identical ground field of view. We used an aluminum rod with a pistol-grip mount at one end to position the fiber optic bundle in a nadir view 18 cm above the snow surface, which resulted in a ground field of view of approximately 8.5 cm. The other end of the rod was connected to a pivot, which we used to move the fiber optic cable back and forth over the snow and Spectralon samples. To ensure the view angle of the fiber bundle was nadir relative to the snow surface, we leveled both the target surfaces and the aluminum rod. We encompassed a roughly 3' sphere around both the snow and Spectralon in blackout cloth to minimize the ASD measuring light scattered off surfaces other than the intended target (Figure 2.3). While measuring the reflectance of one surface (snow or Spectralon), we prevented the ASD from collecting light scattered from anything other than the desired target by covering the non-target surface with blackout foil.
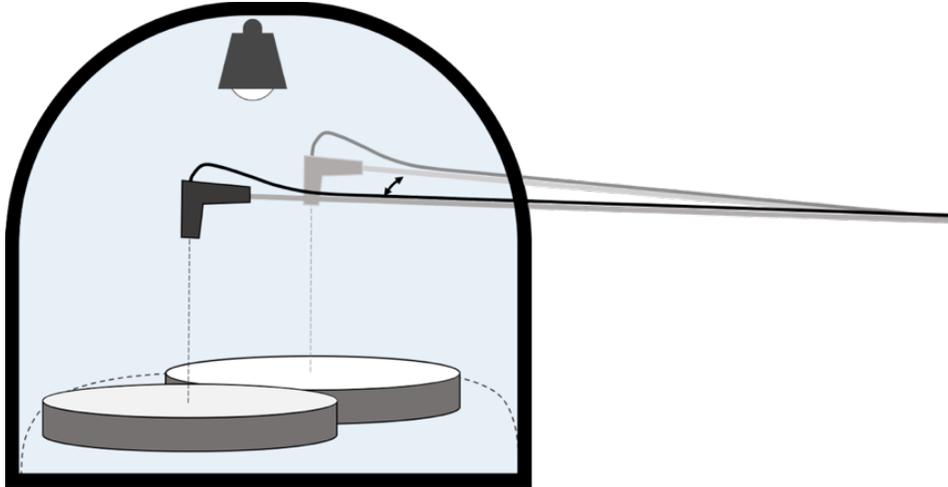
Figure 2.3: Schematic of hyperspectral measurements set-up. The circular disc in the front-left represents the snow in our experimental test bed, while the rear-right disk is the Spectralon target. We mounted the ASD viewing fiber in a pistol grip on an aluminum rod, which we moved laterally between the two target surfaces. In this schematic the black pistol grip (on left) indicates the ASD viewing fiber position during snow measurements, while the grey pistol grip (on right) shows the ASD viewing fiber position for Spectralon measurements. The light source, snow, and Spectralon targets were surrounded with blackout cloth to reduce stray light reflecting off the floor and walls of the SIRF.

We generated our snow surface reflectance signatures by recording several consecutive snow and Spectralon reflectance measurements. Each reflectance measurement is an average of 25 consecutive individual ASD scans of the target surface (made every 0.2 seconds). The bidirectonal reflectance factor, hereafter referred to as reflectance, was calculated by taking the ratio of the snow surface reflected radiant flux to the calibrated Spectralon reference panel reflected radiant flux (Nicodemus and others, 1977; Martonchik and others, 2000; Schaepman-Strub and others, 2006). To account for variability due to light and power, atmospheric conditions in the freezer and user operation we averaged 10 reflectance measurements to produce a representative reflectance signature for each target surface (i.e., snow of small grain size, medium grain size, large grain size.

2.2.3.2 Impurity Filtration

In addition to estimating the relative impurity loading in our snow with hyperspectral reflectance measurements, we made quantitative measurements to assess the optical impurity for four groups of snow: the three sieved snow grain distributions (small, medium, and large), and unsieved snow that we did not use during our experiments, which acts as our control. To measure the optical loading in each of our four sample groups we melted between 500 and 1000g of snow and filtered 20 – 200 mL of melt water through a 0.4 μm nucleopore filter following the method initially described in Clarke and Noone (1985) and improved upon in Doherty and others (2010). After drying our filters, we measured the transmission spectrum of each filter and fit these to spectra from a set of calibrated standard filters with known amounts of (BC). The absorption cross-section of particles on the filters is then divided by the mass of melt water passed through the filter to calculate the absorption coefficient (k_{abs}). Using the relationship:

$$k_{abs} = \beta_{abs}C,\qquad\qquad (2.4)$$

we can calculate the mass of BC per unit mass of snow (*C*) given the mass absorption cross-section (β) of BC. Following Doherty and others (2010), we calculate the equivalent BC in our snow to compare with *in-situ* measurements of BC (i.e., equivalent BC is the amount of BC needed in the snow to produce the wavelength-integrated total light absorption from 300 – 750 nm).

2.3 Results

2.3.1 Transmission Measurements

We measured the intensity of transmitted light reaching the central detector at a given depth for each snow grain size distribution at least three times to characterize variability from sieving snow into the test bed. We then combined these measurements into a mean intensity profile (thick lines in Fig 2.4) for each snow grain size distribution and calculated the associated two-sigma error (shaded area). We normalized all intensities to the measured surface (no snow) intensity for each profile measurement to allow for comparison between profiles.
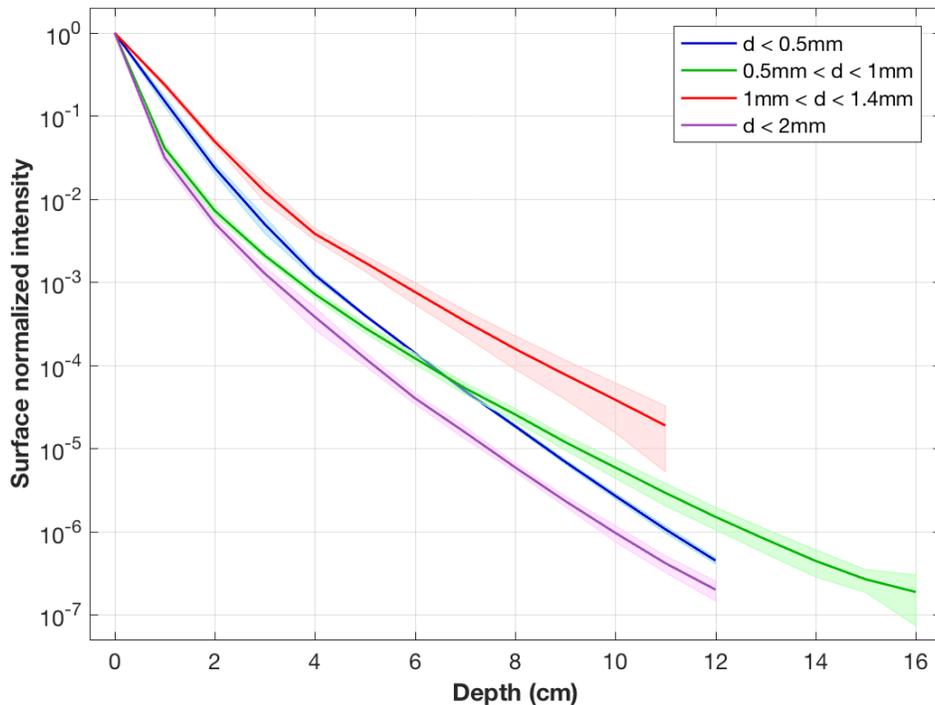
Figure 2.4: Transmission of green laser light (543 nm) through snow of differing grain sizes. The intensity of light at a given depth is relative to the surface (no snow) intensity for each profile. Dark lines indicate the weighted mean of observations for a given profile, with the light shading denoting the 2-sigma uncertainty associated with the weighted mean.

Our measurements show that snow grain size affects the absolute intensity of light reaching a given snow depth. These differences are most pronounced at depths greater than approximately four centimeters. Smaller snow grains attenuated the light at greater depths more than larger snow grains. The exception to this was intensities measured for snow from the un-separated distribution, which had the lowest measured intensities of all snow grain size distributions at all depths we measured. We also measured the snow density for both shallow and deep depths, as well as all snow grain size distributions, and found no significant change in density, as shown in Figure 2.5.
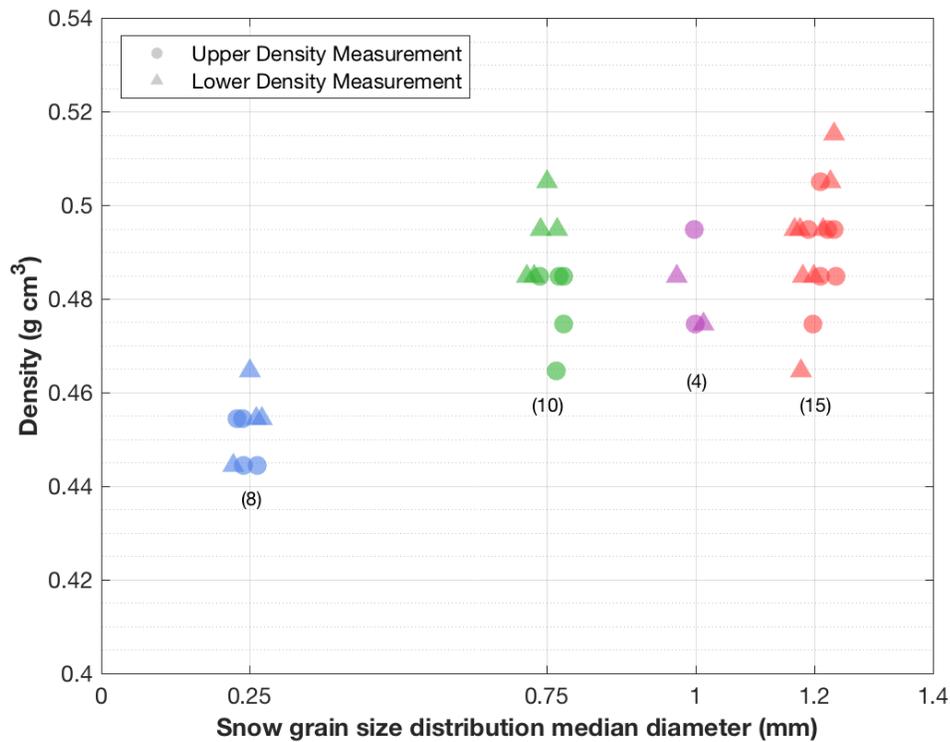
Figure 2.5:   Measurements of snow density for all snow grain size distributions. We introduced random jitter in the values of the median grain diameter (x-axis) so that repeated density values would be easily visible and not overlap each other.
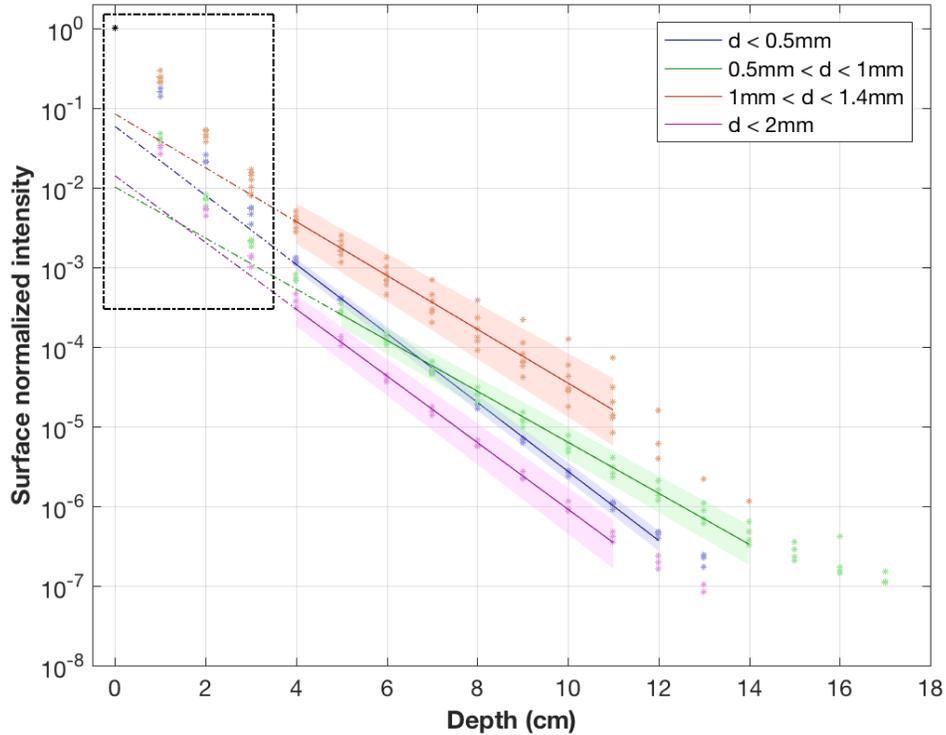
Figure 2.6: Best-fit lines for green laser light (543nm) attenuation through snow of differing grain sizes. Shaded areas correspond to a 2-sigma equivalent uncertainty associated with each color's respective best-fit line. Colored stars are the individual intensity observations, which are combined to make the heavy solid lines in Fig. 5 following the methodology described in Appendix A. Best-fit lines do not include lower regions where observations were not consistently obtainable, or shallow snow where the rate of attenuation is not constant.

In addition to the amount of light transmitted at a given depth, our results also show that snow grain size affects the rate light attenuates with depth. Light intensity attenuates exponentially with depth at a relatively constant rate below four centimeters, but the rate varies at shallower depths (black box in Figure 2.6). Smaller snow grains attenuated light more rapidly with increasing depth than larger snow grains below approximately four centimeters as can be seen by the blue line crossing over the green line. Due to the variable rate of attenuation in shallow snow, we only fitted an exponential trend to intensity measurements at depths greater than four centimeters (Figure 2.6). We also only fit to depths with the same number of data

points at each depth. The uncertainty for these fits (shaded regions) is characterized by the two-sigma error associated with our measurement of the snow depth and the variability in intensity measurements following the weighted total least-squares method (Krystek and Anton, 2007).

We also measured light intensities at the side detectors at least once per snow grain size distribution. This allows us to better characterize the scattering properties of the snow. An example of an intensity profile for all three detectors using snow grains from the medium size distribution is shown in Figure 2.7.
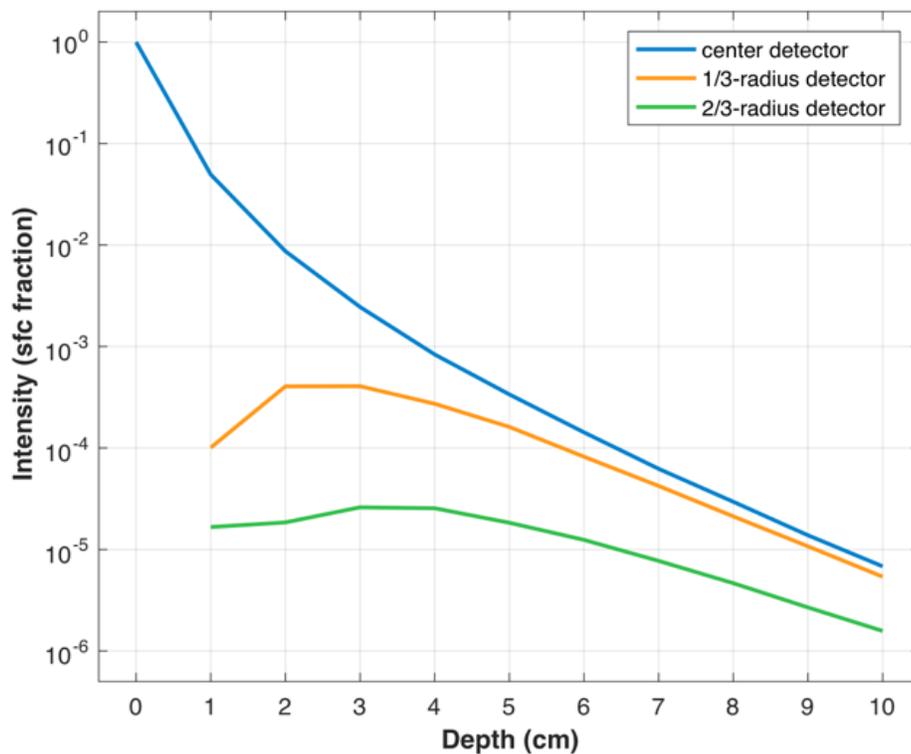
Figure 2.7: Laboratory measurements of transmission for snow with grain diameters between 0.5mm and 1.0mm for three detectors: the first (blue) located at the center of the test cylinder, the second (orange) 1/3 the radius of the cylinder, and the third (green) at 2/3 the radius of the cylinder.

2.3.2 ASD Measurements

Our snow reflectance measurements made in the SIRF (Figure 2.8) display a characteristic maximum in reflectance for each grain size distribution near 700 nm, along with a local maximum at approximately 1100 nm and increasing absorption in the near infrared and short-wave infrared wavelengths as expected for snow (e.g., Pope and Rees, 2014). We also observe lower reflectance at 400 nm relative to 700 nm in our measurements. Consistent with previous studies, in which reflectance is dependent on snow grain size (Nolin and Dozier, 1993; Nolin and Dozier, 2000), our reflectance measurements show snow from the smallest grain size distribution having
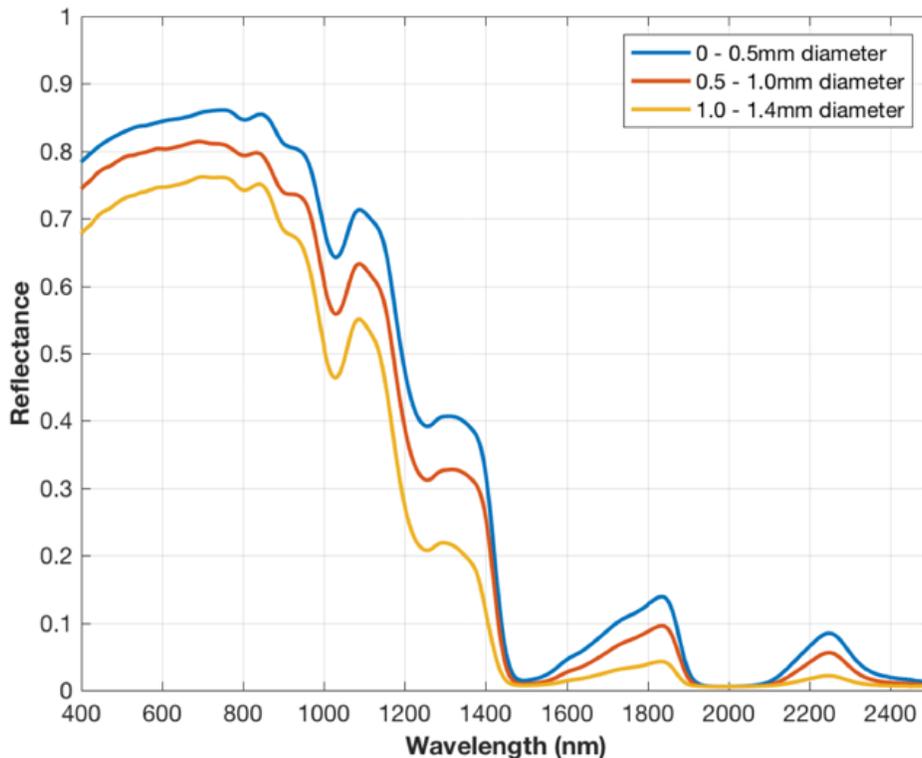
Figure 2.8: Spectral reflectance from snow with different snow grain distributions: d < 0.5 mm (blue), 0.5 mm < d < 1.0mm (red), 1.0 mm < d < 1.4 mm (yellow).

the largest reflectance and snow from the largest grain size distribution having the lowest reflectance.

2.3.3 Filtration Measurements

Measurements of the BC loading in our snow are shown in Table 2.2. Our control snow (snow we set aside and never used for experiments) had nearly two orders of magnitude more BC than is found in clean snow from Summit, Greenland (Chyleck P and others, 1995; Doherty and others, 2010). The BC in our sieved samples of snow was approximately three orders of magnitude more than expected for clean dry snow from Summit. We also note that for the sample groups separated by grain size, BC concentrations increase with decreasing grain size.

Table 2.2: Mean equivalent black carbon concentration for sample group

Distribution short name	C_{BC}^{equiv} (ng g^{-1})	C_{BC}^{equiv} (ppm$_{mass}$)
small	2381	2.381
medium	1824	1.824
large	1020	1.020
CONTROL	120	0.120

2.4 Discussion

2.4.1 Transmission Measurements

Our data show a clear dependence on grain size for green light transmission through snow. The amount of transmission can be divided into two regimes based on depth: (1) the near surface where the attenuation rate is relatively high due to photons scattering out of the snow (Warren, 1982) compared to (2) the interior, which is defined by a lower attenuation rate as the attenuation coefficient approaches an asymptotic value representative of a semi-infinite medium (Figure 2.9). However, cross-over of transmission profiles in the near-surface regime make determining the snow grain size distribution from transmission data alone difficult without *a priori*
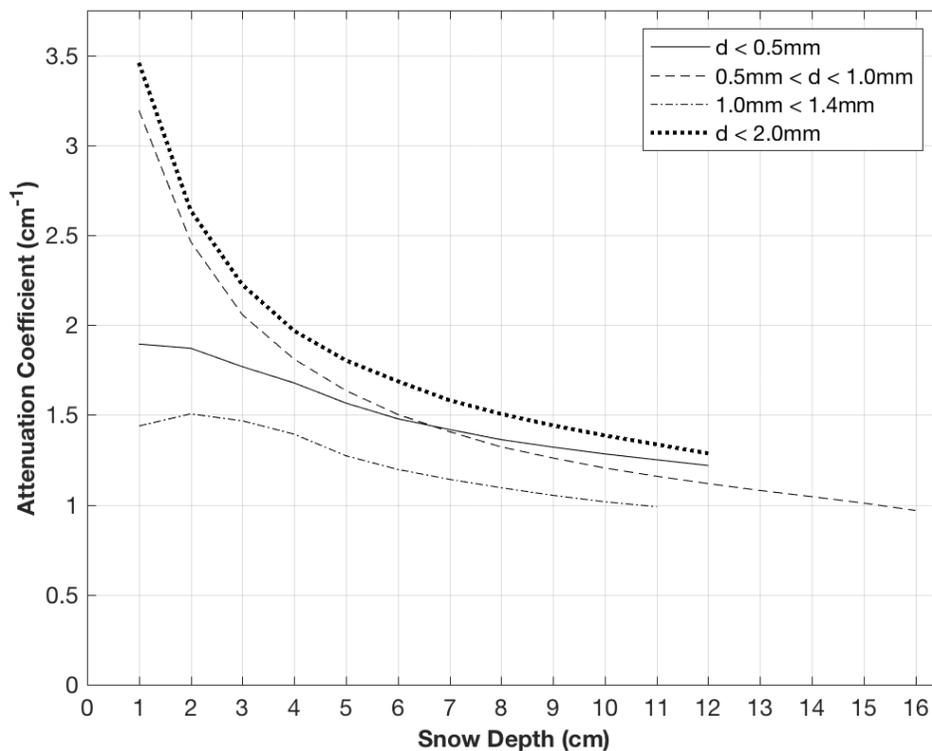
Figure 2.9: Variations in snow attenuation coefficient with depth

knowledge. We note that here and for the rest of the study, we define the narrow-beam attenuation coefficient as the decay factor derived from the ratio of transmitted radiant flux at a given depth to the radiant flux at the surface of the snow using a narrow, collimated beam as the illumination source, and where the loss in transmitted radiant flux is due to absorption and scattering while passing through snow. We use the term 'narrow-beam attenuation coefficient' interchangeably with 'attenuation coefficient.'

The near surface regime extends from the surface to approximately four centimeters deep and is characterized by a decreasing rate of attenuation as depth increases. This decrease in rate of attenuation in this shallow layer may be explained by photons scattering out of the snow before being scattered toward the detector (Warren, 1982). For example, if a photon traveling down into the snow were to reach a depth of one centimeter and then be scattered backward toward the surface, it would only have one centimeter worth of snow in its path to change its direction back down toward the detector before exiting the snow and leaving the experiment. By comparison, a photon that had reached a depth of four centimeters into the snow before being scattered upward would have four times as many scattering opportunities for its direction to be changed back to a downward trajectory and thus be more likely to remain in the snow. The more photons that remain in the snow, the greater the probability that a photon is measured by the detectors at the bottom of the snow. The increased rate of photons leaving the snow, as well as a higher incidence angle of light at the detectors, results in lower intensities measured by the 1/3rd- and 2/3rd-

radius detectors at shallow depths. More photons scattering out of the snow at the snow-air boundary at shallow depths, relative to deeper snow, results in few photons reaching the detectors at the bottom of the test bed, making it appear as though the light at shallower depths is attenuated more than at deeper depths. A quantitative analysis of this observation is the subject of a future publication.

In contrast to the near surface regime, the interior regime is defined as the area where the rate of photon loss is independent of the snow-air boundary. That is, photons in the interior regime are lost due to scattering out of the direct beam and subsequently absorbed by the test bed walls or floor, or absorbed in the snow grains (i.e., absorption by the ice itself or impurities in the ice).

Since light attenuation in snow is exponential when optically far from boundaries (Bohren and Barkstrom, 1974), we fit an exponential curve (solid colored lines in Figure 2.6) to light intensities in the interior region, away from the surface boundary, where the attenuation rate is constant. Our data show that large diameter snow grains attenuate light less than snow grains with smaller diameters. Larger snow grain diameters result in fewer scattering events for the same geometric scattering distance traveled by photons, providing fewer opportunities for individual photons to be absorbed or be deflected away from the detector. However, this observation is complicated by comparing the transmission through the medium snow grain distribution against transmission through the small snow grain distribution above and below 7 cm snow depth. Above 7 cm, the small snow grains transmit more light than

the medium snow grains, while below 7 cm they transmit less light than the medium snow grains. (Figure 2.6). This cross-over in transmission profiles creates ambiguity between different grain sizes and renders them inseparable using only transmission data. The reason for this cross-over is not obvious from the transmission profiles alone, but is likely related to the higher concentration of light absorbing impurities in the small snow grain distribution relative to the larger snow grain size distributions (Table 2.2).

In the interior regime, the three grain size distributions (small, medium, and large) seem to behave according to the following pattern; the more scattering surfaces per unit volume, the greater attenuation of 543 nm light with depth. We would then expect that the transmission profile for the snow grain distribution containing all three of the above constrained distributions (the unseparated distribution) to lie somewhere between the transmission profile of the smallest grain size distribution and the profile of the largest grain size distribution. However, we see that its transmission profile is below that of even the lowest snow grain distribution profile (Figure 2.4). Since all data were collected following the same protocol, this leaves us to speculate that the high rate of attenuation associated with the profile containing all grain sizes may be due to the ratio of different grain sizes present in the same snow sample. We note that the rate of attenuation in the first 2 – 3 cm of the profile for all grain sizes (the purple line in Figure 2.4) seems to closely follow the attenuation rate for snow grain diameters from the medium grain size distribution (green line in Figure 2.4), before changing to attenuate at the nearly the same rate as the small grain size distribution

31

from 4 – 10 cm. The small and medium grain size distributions make up the majority of all snow grain diameters present in our snow (data not shown). We suggest that the rates of attenuation observed for the combined snow grain size profile is dominated by the attenuating effects present in these two constrained grain size distributions. An experiment could be designed to test the relative influence of these two constrained size distributions on the combined transmission profile by mixing snow from these two distributions in various proportions (e.g., 10% of snow by volume from the small grain size distribution with 90% snow by volume from the medium grain size distribution), and measuring the resulting transmission profiles.

We also measure significantly lower transmitted light intensities at depth than other studies (Warren and others, 2006; Perovich, 2007). The primary source for this difference is that field studies (Warren and others, 2006; Perovich, 2007; Grenfell and others, 1994) rely on the sun as their illumination source, which illuminates the entire surface of their snow cover, whereas we used a collimated laser beam 1 cm in diameter to illuminate our snow. As a result, the light reaching our detector was only from a very small illuminated area on the surface of the snow, rather than a completely illuminated snow surface, thereby decreasing the overall amount of light reaching our detector. This provides a simplified boundary condition for our experiment, as the incident light at our snow surface is both collimated and coherent, and makes our transmission measurements more analogous to those made by Sergent and others (1987), which measured transmission for very shallow layers of snow in a laboratory setting, but used a diffuse light source. While using a collimated beam for

our illumination source does not provide for direct comparison with the aforementioned field studies that relied on natural sky illumination, this approach does provide a good analog for laser altimetry.

2.4.2 ASD Measurements

Our measurements of snow reflectance made in the lab (Figure 2.8) compare well with the reflectance measured outdoors using the sun as the illumination source (not shown). This suggests that our laboratory reflectance measurements (hereafter, we refer only to reflectance measured in the laboratory) are analogous to field reflectance studies. However, our measured snow reflectance is lower than field and modeled reflectance for pure or freshly fallen snow. This is not surprising as our snow is old, heavily metamorphosed, and contains a considerable amount of impurities relative to fresh, non-polluted snow. For example, Figure 2.8 shows a decrease in reflectance from approximately 700 nm to 400 nm for all grain sizes, which is indicative of the presence of absorbing particles such as soot or dust in our snow, consistent with analogous model calculations of spectral albedo for snow with impurities (Warren and Wiscombe, 1980; Hadley and Kirchstetter, 2012; Kokhanovsky, 2013; Kaspari and others, 2014), as well as field studies (Qunzhu and others, 1983; Aoki and others, 2000; Bøggild and others, 2010; Pope and Rees, 2014; Casey and others, 2012; Casey and others, 2017; Skiles and Painter, 2016). This qualitatively suggests that while our snow is not as clean as freshly fallen snow or snow collected in a pristine environment, it is also not characterized by the low reflectance of snow heavily contaminated with dust, volcanic ash, soot, or biota (Gautam and others, 2013; Skiles

and others, 2016; Pope and Rees, 2014; Casey and others, 2017; Khan et al., 2017; Painter et al., 2001; Takeuchi et al., 2009; Hodson and others, 2017; Cook and others, 2017).

There are several other factors that may have influenced our measurements of snow reflectance. One is that our snow is old and heavily metamorphosed, which is likely to result in lower reflectance than fresh snow (Qunzhu and others, 1983). While it has been keep frozen since being collected at Summit, Greenland in 2008, it has undergone several temperature changes and been handled extensively. As such, it has lost much of its fractal structure in favor of irregularly rounded grains. A second is that most of our snow grains are larger than those observed in-situ, which has the effect of lowering snow reflectance (Nolin and Dozier, 2000). Typical fresh snow grain diameters found in the interior of Antarctica are on the order of 0.3 mm or less (Gay and others, 2002; Scambos and others, 2007), and less than 0.5 mm in central Greenland (Lyapustin and others, 2009).

2.4.3 Filtration Measurements

To more quantitatively assess the optical impurity load in our snow, we made laboratory measurements of equivalent BC. Doherty and others, 2010 found equivalent BC loading at the surface of dry Summit snow to be 4.0 ng·g^{-1}; just under two orders of magnitude less than the 120 ng·g^{-1} measured in our unsieved Summit control snow. Averaging the measured equivalent BC loading for all three size distributions of the snow that we used for all of our experiments shows an additional

order of magnitude more impurity loading, 1742 ng·g⁻¹, than our un-used control snow. This suggests that impurities were accumulating in the snow as we experimented on it, likely from repeatedly sieving and grating the snow, as well as loading and emptying the snow from the test bed. Additionally, it is likely impurities were uniformly mixed throughout our snow samples during experiments as a result of regular sieving. Natural snow with similar loading of equivalent BC to our control snow (100 – 300 ng·g⁻¹) can be found in at several sites in central and eastern Russia, where the high concentrations of BC for these sites is likely due to their relatively close proximity to urban areas (Doherty and others, 2010). In comparison, snow collected in Northern China contained concentrations of equivalent BC an order of magnitude larger than our control snow (Wang and others, 2013). In contrast to the impurities from these *in situ* sites, most of the impurities added to our snow during experimentation likely came from our sieves, the test bed used for transmission measurements, and from the gloves used to handle the snow. These measurements confirm our snow contains more impurities than expected for pure snow at Summit, Greenland, but is not completely out of bounds for BC concentrations found in natural snow.

2.4.4 Potential Bias Sources

Before taking transmission measurements, we anticipated and characterized several potential sources of bias in the experiment design. First, we addressed the sensitivity of the photo-diode detector to variations in temperature due to the freezer's cooling cycles. We characterized this by continuously illuminating a detector located in the

35

freezer with the laser beam, and measuring the detected intensity as the freezer cycled on and off several times. During these cooling cycles the temperature fluctuated by 5°C. We also measured a large temperature change by lowering the freezer temperature from -5°C to -20°C to determine if the environment's ambient temperature affected the detector's measuring efficiency. During these tests, a detector outside the freezer picked off a fraction of the laser beam using a beam splitter cube so we could correct for fluctuations in the laser power. The temperature inside and outside the freezer was measured using a thermocouple wire and sampled at the same rate as the photo-diode light intensity. In both temperature tests, there were no measurable fluctuations in the detector-measured intensities associated with changes in the freezer's temperature.

A second potential source of bias was photons reflecting off the walls and floor of the test bed, thereby biasing measurements of the direct transmission of light through the snow. We explored this potential source of error in two ways: through the color of the walls, and the proximity of detectors to the walls. For both tests, we oriented the laser beam so it was normal to the surface of the wooden disc the detectors were embedded in (i.e., parallel to the cylindrical cardboard walls of the test bed) and centered such that the walls were equidistant from the laser beam in all directions. We tested the influence of the walls' proximity to the detectors by first centering the laser beam directly over the central detector, filling the test bed with 8 cm of snow, and then measuring the transmitted light intensity. We then moved the laser beam directly over the detector located 3.3 cm from the center of the test bed and again measured the

transmitted light. Finally, we moved the laser over the detector 6.6 cm from the center of the test bed and measured the transmitted light once more. We then covered with walls and floor of the test bed with white paper and repeated the measurements at the three detector locations (0 cm, 3.3 cm, and 6.6 cm) to test the influence of the wall color. In all six trials, we were unable to measure a change in the intensity measured at the center detector, or any of the side detectors, leading us to conclude that any influence due to proximity or color of the test bed walls or floor on our measurements of direct transmission of light through the snow was outside the precision of our experiment design to measure.

A third source of uncertainty in our measurements is the range of snow grain diameters. The snow was sieved to physically constrain snow grain diameters as described in the methods section. While this approach has the advantage of physically separating the snow by size, it does not describe the physical shape of the snow grains completely. For example, an irregular or elliptically shaped snow grain could be described as having an equivalent spherical diameter were it to occupy a sphere of the same volume, or area (Grenfell and Warren, 1999). For perfectly spherical snow grains, the sieve mesh size would be an appropriate constraint for the physical snow grain diameters. However, our snow grains, while generally rounded, were not perfectly spherical. As such, elongated or irregularly shaped snow grains may have passed through the mesh and moved into a smaller snow grain diameter distribution than a snow grain of equivalent spherical diameter would. This is to say that for non-spherical snow grains, the sieve mesh only filters snow grains by their smallest axial

diameter. The result is that rather than having a uniform number of snow grain diameters distributed across a given snow grain diameter range, there will be relatively fewer snow grains of equivalent spherical diameter toward the lower end of the diameter range and relatively more snow grains of equivalent spherical diameter at the upper end of the diameter range than the number of snow grains with diameters in the middle of the diameter range.

2.5 Conclusions

In this study, we found that the transmission of 532 nm light from a narrow, collimated beam is dependent on snow grain size. The rate at which light attenuates is not constant in the top 4 cm of snow due to the snow-air boundary, but approaches a constant value, consistent with a semi-infinite medium, below 4 cm. As a result, light intensity attenuates at a rate of approximately one order of magnitude per centimeter in the top 4 cm of snow, and approximately one order of magnitude every 2 cm at snow depths greater than 4 cm. In the interior region of our snow, optically far from any boundaries, larger snow grains attenuate light less than smaller snow grains. We believe this is a result of larger snow grains providing fewer scattering events for the same geometric distance as smaller snow grains. Our transmission measurments were also affected by light absorbing impurities in the snow. This likely contributed to the cross-over in transmission profiles for the small and medium snow grain size distributions, as well as the low transmission values of the unsieved snow grain

distribution. While the impuritiy loading in our snow was much higher than typical values found at Summit, Greenland, it was within the levels found in less pristine natural snow environments, and is likely to contain lower amounts of impurities than margin areas of ice sheets.

These results also provide constraints for the transmissive properties of snow for 532 nm light that are applicable for understanding the likelihood of photons to be received by a laser altimeter, such as ATLAS, after scattering within snow. Based on our measurments, we expect less than 0.01% of incident photons to exit the snow surface after traveling to a depth of 2 cm, and less than 0.00001% of photons that reach a depth of 5 cm. This suggests that photons from laser altimeters that enter the snow are not likely to travel great depths and still escape the snow to be received by the instrument, and those that do will likely come from the top few centimeters of snow.

Chapter 3: Fitting an Exponentially-Modified Gaussian

Function to Returns from Photon-Counting Lidars

3.1 Introduction

ICESat-2 (Ice, Cloud, and land Elevation Satellite-2) will carry NASA's next-generation laser altimeter, ATLAS (Advanced Topographical Laser Altimeter System) to measure the changing elevation of Earth's ice sheets, glaciers and sea ice (Markus et *al.*, 2017). This marks the first time a photon-counting space-based lidar will be used for precision terrestrial ranging to determine elevation. To prepare for this new method of measuring Earth's surface height, NASA developed MABEL (the Multiple Altimeter Beam Experimental Lidar; McGill et *al.*, 2013), an aircraft based photon-counting laser altimeter that uses 1064 nm and 532 nm wavelength laser light to measure elevation. Designed as a simulator for ATLAS, MABEL has flown over a variety of surface targets including ice sheets (Brunt et *al.*, 2014), glaciers (Brunt et *al.*, 2016), sea ice (Kwok et *al.*, 2014; Farrell et *al.*, 2015), inland and coastal waters (Jaskinski et *al.*, 2016), as well as boreal forests and ecosystems (Awadallah et al., 2014; Glenn et *al.*, 2016; Gwenzi and Lefsky, 2014) to develop and test algorithms for estimating surface elevations from photon returns (Brunt et *al.*, 2016). The underlying principle of laser altimetry is common to all altimeters: measuring the time it takes for a pulse of light to travel from the altimeter, to the surface, and back.

Full-waveform altimeters such as ATLAS's predecessor, GLAS (Geoscience Laser Altimeter System) on ICESat (Schutz et *al*., 2005), ATM (Airborne Topographical Mapper; Krabill et *al*., 2002), G-LiHT (Goddard's Lidar, Hyperspectral and Thermal Imager; Cook et *al*., 2013), and LVIS (Laser Vegetation Imaging Sensor; Blair et *al*., 1999) all record the time-varying intensity of returning laser pulses using a high-frequency digitizer. The photon-counting based approach ATLAS and MABEL use to measure target surfaces requires different retrieval methods to ensure precise and accurate surface elevation estimates from returning photons.

While a single measurement from a full-waveform lidar system is sufficient to make a single elevation measurement, photon data from several shots must be aggregated to make a single elevation measurement using a photon-counting lidar. Common to both types of lidar is the need to characterize the effects of the instrument on the recorded light pulse; that is, the instrument impulse response function. In this paper, we develop a new method to characterize photon-counting lidar data, and use the method to understand the instrument impulse-response function for MABEL, and apply the method to field data collected with MABEL. Using a Monte Carlo model, we also examine the extent to which discrete samples of photon data accurately describe the parent population as a means to assess the accuracy of elevation estimates using photon data.

3.2 Motivation

The instrument impulse response function characterizes the cumulative effects of the entire instrument on the measurement. For example, the transmitted pulse of light itself has some duration; ATLAS and MABEL both emit a ~1.5 nanosecond long pulse. As such, the duration (or temporal shape) of the light pulse must be considered when measuring surface elevation. When the transmitted light pulse reaches the surface, physical properties such as slope, surface roughness, and volume scattering, cause the reflected, or scattered, light pulse to spread out in time. We refer to these combined effects as the surface impulse response function, or SIRF. The recorded return pulse is then the convolution of the transmitted pulse, the SIRF, and the effects of the receiver optics and electronics. A recorded return of a non-divergent pulse from a perfectly specular surface would contain only the effects of the transmitting and receiving optical and electronic components of the instrument (i.e., the instrument impulse response function, or IIRF).

An ideal method for characterizing the IIRF would be to measure the transmit pulse as it leaves the instrument, as the transmitted pulse shape is the dominant term in the IIRF. Many full-waveform laser altimeters including GLAS, ATM, G-LiHT, and LVIS, record the shape of the transmitted laser pulse as it leaves the altimeter with a high-frequency digitizer. Given the short-duration of the transmitted pulse, and the rapid pulse repetition frequency, ATLAS will not measure the shape of individual

transmitted pulses. As a result, we are left to determine the IIRF from returning photons, which is complicated by the effects of the SIRF.

The fact that photon-counting altimeters detect individual photons makes measuring the shape of any single laser pulse difficult compared to full-waveform altimeters. Photon-counting altimeters must use low intensity light to avoid saturating their detectors (Degnan, 2002), or incur substantial dead time effects. ATLAS for example, records up to only approximately 10 surface return photons per pulse, depending on the surface (Markus et *al*., 2017). With such a small number of photons, and short temporal pulses, it is difficult to accurately describe the shape of a single pulse using the recorded photon data. In addition, it is difficult to discriminate signal photons from background photons. Therefore, photons from several shots are often aggregated in a histogram (Brunt et *al*., 2016) to construct a pulse shape which is analogous to the pulse shape measured by a full-waveform altimeter. Given enough photons and an expectation of the pulse shape's underlying distribution (i.e., the transmitted pulse shape), we can reconstruct the IIRF of a photon-counting laser altimeter if the SIRF is known.

Accurately characterizing a laser altimeter's IIRF is necessary to understand the effects of surface features such as slope, surface roughness, or volume scattering, on received photons and the elevation estimates derived from them. Laboratory measurements show that MABEL's pulse shape is asymmetric with an extended tail. This asymmetric pulse shape with extended tail is not unique to MABEL, having also

43

been observed in other laser altimeter systems such as the Lunar Orbiter Laser Altimeter (LOLA) on NASA's Lunar Reconnaissance Orbiter (LRO) spacecraft (Smith et *al*., 2010). However, identifying and properly characterizing the asymmetric and trailing edge of MABEL's pulse shape is important because volume scattering in snow is expected to spread out, or broaden, the returning pulse shape (Greeley et al., 2017). The asymmetric pulse shape is due to the use of an active Q-switch within both the MABEL and ATLAS lasers to produce short duration laser pulses. Q-switching requires a buildup of photons within the laser cavity to a threshold before exiting the laser cavity. When the Q-switch opens, the leading edge of the pulse growth rate is much larger than the laser cavity decay rate due to the large number of photons that build up prior to the Q-switch opening. This causes a rapidly rising pulse. Once the peak of the laser pulse is reached, the intensity of the pulse decreases at the slower laser cavity decay rate, thereby elongating the trailing edge of the laser pulse (Seigman, 1986). As a simulator for ATLAS, MABEL provides an opportunity to explore how best to quantitatively describe the impulse response function of a Q-switch based photon-counting laser altimeter.

Since photon-counting systems provide individual photon times of flight, as opposed to a digitized record of surface-reflected intensity, a primary consideration is the number of laser pulses, or photons, to aggregate such that the pulse shape becomes apparent. Although not used to describe the pulse shape, a common method for aggregating photon data is to generate a histogram (Dabney et *al*., 2010; Krichel et al., 2010; Awadallah et al., 2014; Brunt et *al*., 2014; Herzfeld et al., 2014; Kwok et

al., 2014; Young et *al.*, 2015; Brunt et *al.*, 2016; Yu et *al.*, 2016). Once photons have been aggregated into a histogram, the histogram can then be used to estimate surface elevation in a qualitatively similar process to that employed by waveform altimeters. While forming a histogram is straight-forward, histogram-based approaches suffer from several limitations, including degradation in the resolution of the data due to binning the photons into discrete time range bins, and dependence of the location and width of the histogram bins on the histogram shape. Further, the "significance" of any one histogram bin's height is related to the number of photons in the bin. Therefore,
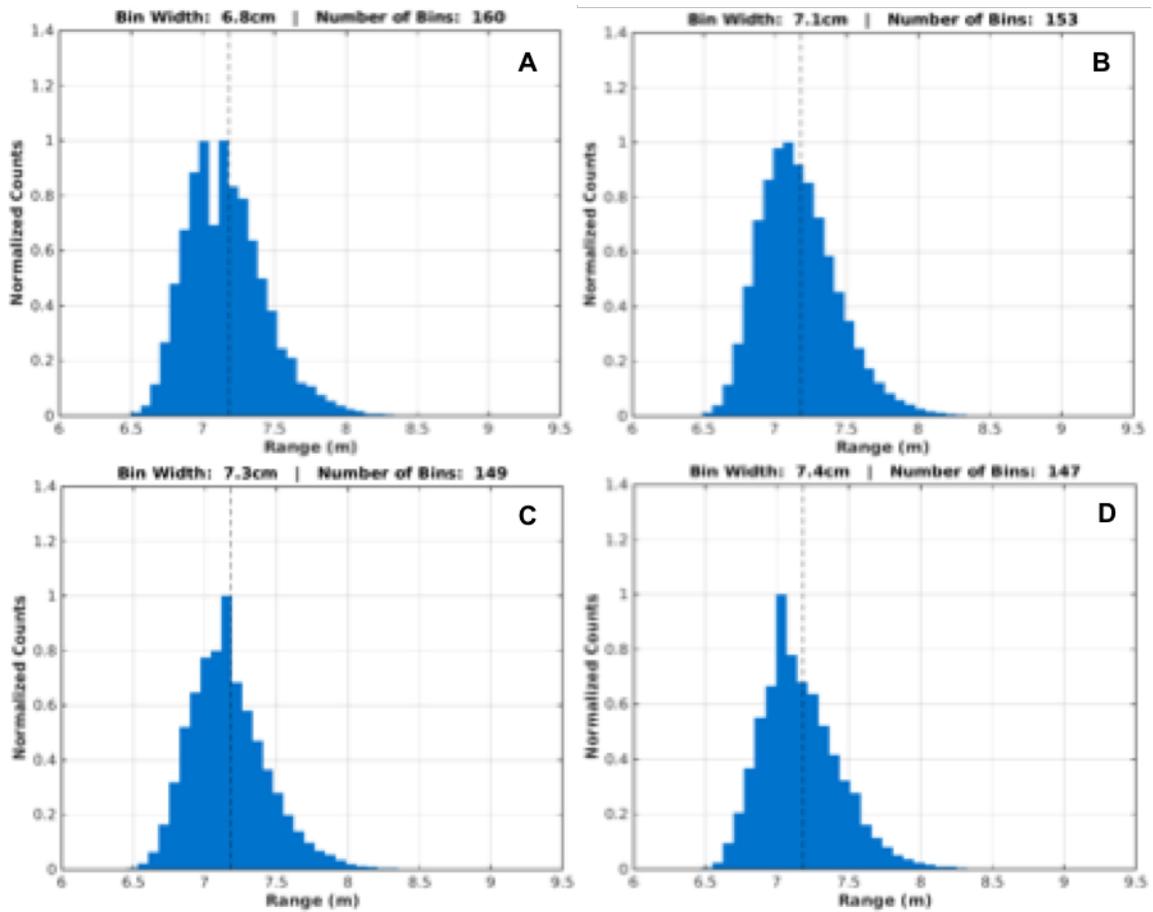
Figure 3.1: Normalized number of photons returning within the specified range bin. The vertical dashed line is the mean range of all photons used to construct the histogram and is the same in each panel. The histograms were calculated using identical data

the specific numeric value of any specific bin compared with adjacent bins may be more a function of the choice of bin location and width than any underlying physics. Additionally, since many shots along a potentially varying surface may be aggregated to accumulate enough photons to reasonably represent the underlying distribution, the resulting distribution inherently aggregates variations in surface response due to variations in surface properties (e.g., changes in elevation, slope, surface roughness, atmosphere, etc.). The limitations of histograms can be demonstrated using MABEL photon returns from a flat surface, such as a Spectralon reflectance panel. The dependence of the histogram shape on histogram bin width is illustrated in Figure 3.1. In all four panels, the same data is used, only the width of the histogram bins has been changed. In panel A, a double peak is visible. In contrast, panel B shows a smooth histogram as expected from a flat surface. In panels C and D, a sharp peak is visible, but changes location by approximately 11 cm due to an increase in the histogram bin widths of 1 mm. These plots provide an illustration of the variability of in histogram shape due to changes in histogram bin width.

A more complete view of the variability in histogram shape due to subjective changes in the properties that define histograms (i.e., bin width and bin location) is illustrated in Figure 3.2. For both panels in Figure 3.2, we randomly select 1000 MABEL photon returns from a Spectralon reflectance panel to generate histograms with unit area. In panel A, the black dots correspond to the top and center of histogram bins for a series of histograms with bin widths ranging from 2.5 cm to 25 cm. For panel B, the black dots are the top and center of histogram bins for a series of histograms with a

46
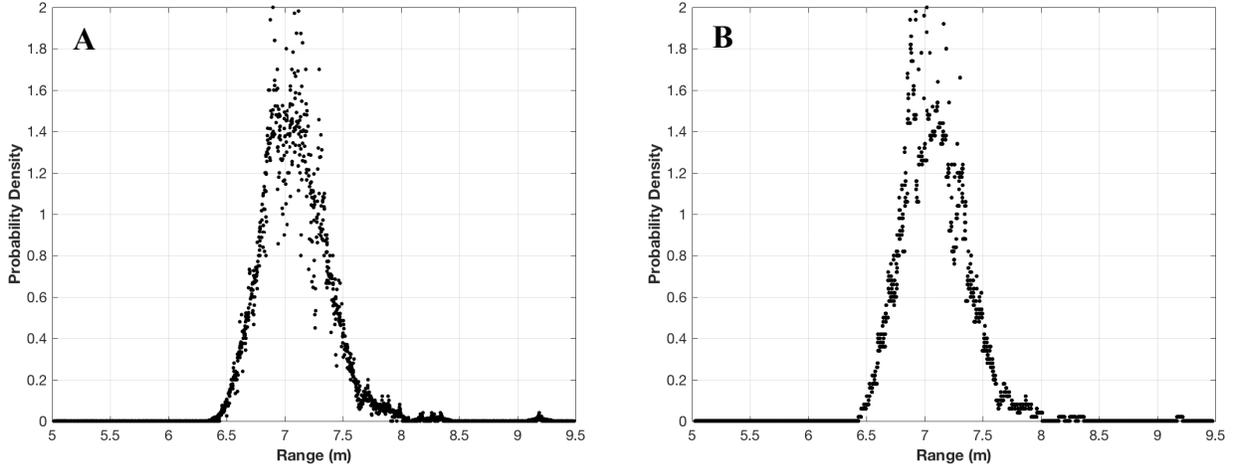
Figure 3.2: (A) Variability in bin center location and height due to incrementally increasing histogram bin width from 2.5 cm to 25 cm. (B) Variability in bin center and height due to incrementally shifting histogram bin locations to the right while maintaining a constant bin width. All histograms use a random sample of 1000 MABEL photons returns from a Spectralon panel.

constant bin width of 5 cm, but increasing the range of the bin centers at 0.5 cm intervals (i.e., shifting the bin centers to the right).

Depending on the application, the variability in the shape or peak of histograms generated from photon data may be undesirable. In this paper, we describe a robust and quantitative method of characterizing MABEL's impulse response function by fitting an exponentially-modified Gaussian function to photon returns. This approach allows us to characterize a return pulse shape with fewer photons than a histogram-based approach, and takes advantage of *a posteriori* knowledge of the distribution of the pulse shape and can calculate the parameters of the distribution from the individual photon returns (e.g., calculating the mean and standard deviation of a Gaussian distribution). We use a Monte Carlo sensitivity analysis to calculate the standard error of the exponentially-modified Gaussian parameters as a function of the

number of photon returns used to fit the exponentially-modified Gaussian function. This provides a means to quantify the error in elevation estimates for flat surfaces based on the number of aggregated photons. Finally, we compare potential surface targets that could be used to measure the impulse response of laser altimeters while on orbit.

3.3 Data and Methods

3.3.1 MABEL data

NASA's MABEL instrument (McGill et *al*., 2013) is a photon-counting laser altimeter capable of laser pulse frequencies between 5 and 20 kHz in both near-infrared (1064 nm) and visible (532 nm) wavelengths. MABEL typically operates on
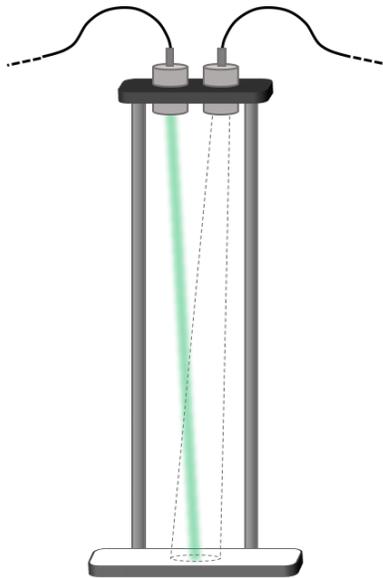
Figure 3.3: MABEL laboratory configuration to measure photons returning from Spectralon panel. The transmit telescope is located on the left, and aligned with the receiver telescope (on right) field of view indicated with dashed lines.

a high-altitude aircraft at a nominal altitude of 20 km, which results in approximately 2 m surface footprints spaced ~4 cm in the along-track direction. In order to minimize the atmospheric and surface effects on return photons, thus enabling a relatively simple characterization of MABEL's impulse response, we adapted MABEL to collect data in a laboratory setting. We used a 12" x 12" Spectralon 99% Lambertian reflectance standard panel as our target surface to eliminate the effects of surface roughness and volume scattering. Since MABEL's telescope is designed for nominal operation at 20 km altitude, we custom built a telescope to ensure that MABEL's field of view overlapped with the transmitted footprint at a range of one to three meters. This required mounting the transmitting, and associated receiving, fiber optic cables for one of MABEL's channels into collimating lenses mounted vertically on an optical bench and aligning the receiving channel's field of view to overlap the transmit footprint on the Spectralon target (Figure 3.3).

We also used MABEL data (NASA Goddard Space Flight Center, 2014) from April 25, 2012 over the Arctic Ocean to measure the IIRF using photons returned from a sea ice lead. During this campaign, MABEL was flown on the NASA ER-2 at a nominal altitude of 20000 m. The sea ice lead we analyzed is the same as in Figure 3 of Kwok et *al*., 2014, and includes the associated digital mapping system (DMS) imagery.

3.3.2 Histogram shape sensitivity to bin width

While Figures 3.1 and 3.2 qualitatively illustrate the issue of histogram shape variability, we quantified the sensitivity of histogram shape (e.g., using mean, standard deviation, skewness, kurtosis, etc.) to histogram bin width and bin location, in order to quantitatively demonstrate the improvement our new method provides. To assess the variability in histogram shape due to bin width, we first created a histogram using MABEL photon returns from a Spectralon reflectance panel (we refer to these photons as the parent population). We then generated a secondary data set from the histogram by assigning the original photon ranges within a histogram bin to that bin's center location. Next, we calculated statistics of this secondary data set (e.g., mean, standard deviation, etc.) that reflect the changing shape of the histogram due to changes in histogram bin width (Figure 3.4). For comparison, we calculated the same statistics for the original photon return ranges (dashed lines).

3.3.3 Definition of the exponentially-modified Gaussian function

We followed the method described by Lacouture and Cousineau (2008) to fit an exponentially-modified Gaussian function to MABEL photon returns. Following Lacouture and Cousineau (2008), we defined the exponentially-modified Gaussian function as:

$$f(x|\mu,\sigma,\tau) = \frac{1}{\tau} exp\left(\frac{\mu}{\tau} + \frac{\sigma^2}{2\tau^2} - \frac{x}{\tau}\right) erf\left(\frac{x - \mu - \frac{\sigma^2}{\tau}}{\sigma}\right) \qquad (3.1)$$

where *erf* is the error function of the Gaussian function and is defined as:

$$erf(x) = \frac{2}{\sqrt{\pi}} \int_0^x e^{-z^2} dz \qquad (3.2)$$

We then fit an exponentially-modified Gaussian distribution to a sample of data points using Matlab's *fminsearch.m* function, which uses an iterative simplex search algorithm to optimize the three defining parameters of the exponentially-modified Gaussian function by minimizing the negative-log sum of the exponentially-modified Gaussian distribution relative to the provided data sample.

The exponentially-modified Gaussian distribution is defined by a set of three parameters: the central tendency (μ), the variability (σ), and the exponential decay (τ). While not explicitly defined for $\tau = 0$, as τ approaches zero the exponentially-modified Gaussian function asymptotically approaches a Gaussian function defined by the μ and σ parameters, which then become the mean and standard deviation of the distribution, respectively.

3.3.4 Sample size influence on parameter stability

Following the method laid out by Lacouture and Coussineau, we assessed the sensitivity of the estimated exponentially-modified Gaussian parameters to different sample sizes by randomly sampling an exponentially-modified Gaussian distribution with prescribed parameter values: $\mu = 10$, $\sigma^2 = 1$, $\tau = 1$ for sample sizes from 10 to

1 million photons. In addition to the three exponentially-modified Gaussian parameters, we also calculated the arithmetic mean (m_1) and standard deviation (m_2) for comparison (solid lines in Figure 3.5). We generate each sample size 1000 times to calculate the mean (solid lines in Figure 3.5) and standard error of each parameter, represented by the shaded region surrounding the solid lines in Figure 3.5.

We also use a Monte Carlo analysis to estimate the probability of calculating a parameter value (e.g., the arithmetic mean, or the exponentially-modified Gaussian mu parameter) within a specified distance of a known population parameter value given a range of sample sizes (Figure 3.6). The equation to calculate the probability of the arithmetic mean of a sample from a larger population having a value within some specified distance (d) of the population mean is given by Thompson (2012):

$$z = \frac{d}{\sigma}\sqrt{\frac{1}{\frac{1}{n}-\frac{1}{N}}} \tag{3.3}$$

where *n* is the sample size (denoted on the x-axis of Figure 3.6), *N* is the population size from which the sample is drawn, and sigma is the population's standard(6) deviation. *Z* is the z-value (standard score) from which we can determine a two-sided probability by referencing a standard statistical table, or by calculating the cumulative probability from the mean and multiplying by two.

3.4 Results

3.4.1 Histogram sensitivity to bin width
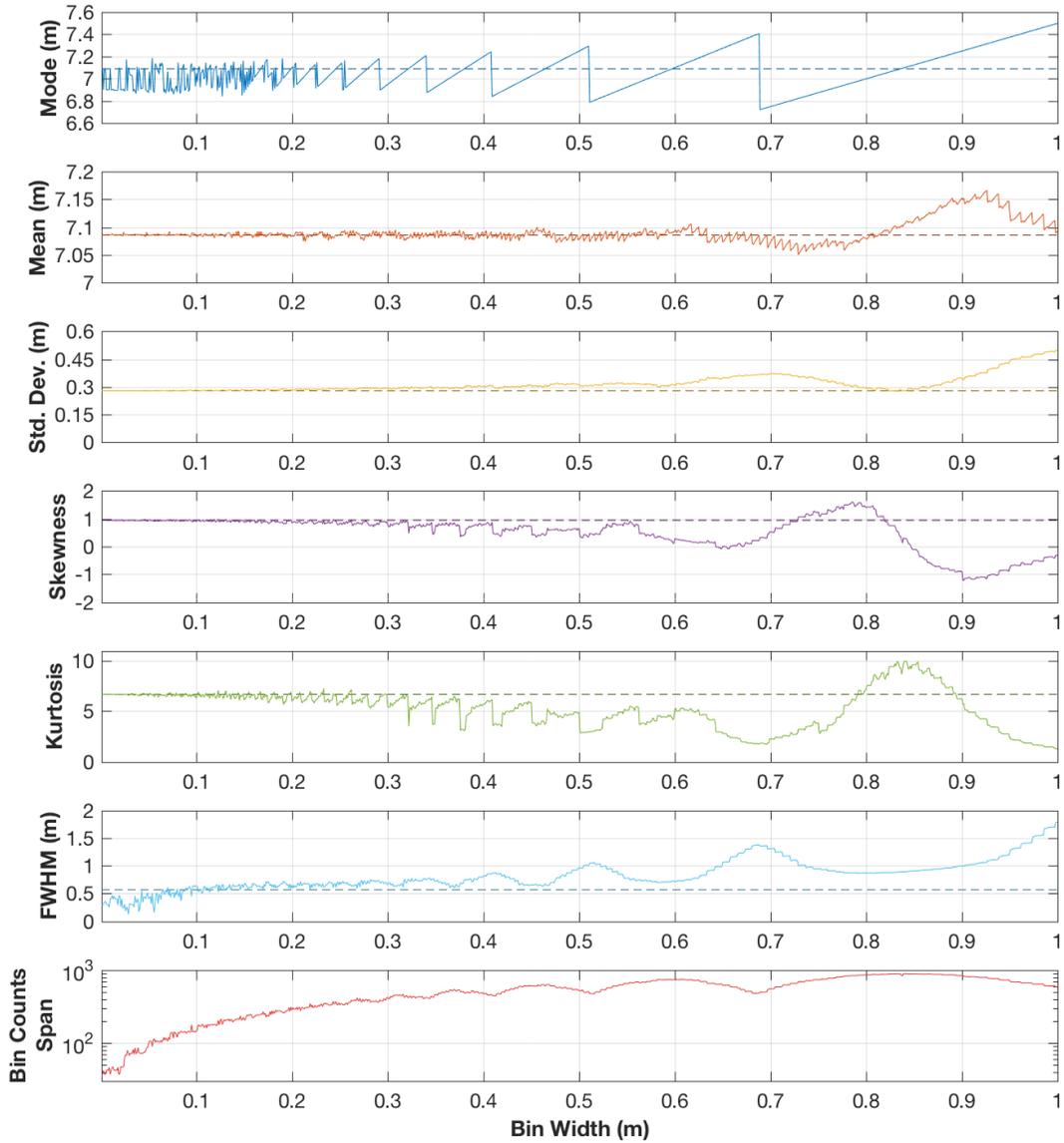
Figure 3.4: statistical moments calculated for the secondary photon return dataset generated from sorting the original photon return ranges into a histogram and then rounding the photon return values in a histogram bin to that bin center's range. This is repeated for multiple histograms with the bin widths used to histogram the original data changed for each new histogram. Dashed lines are the respective statistical moments calculated using the original photon return ranges (i.e., not histogrammed).

While there are no strict guidelines for histogram bin width, our analysis reveals that choice of bin width has a first-order impact on histogram shape. Figure 3.4 shows that variations in histogram shape due to changing bin width are quantifiable using common statistical moments. All moments are relatively stable for small histogram bin widths (approximately 1mm – 30 cm), and converge toward the values calculated directly from the photon ranges, but become variable for larger bin widths (approximately 0.5 m – 1 m). However, the smaller histogram bin widths become, the fewer photons are contained within each histogram bin (Figure 3.4 – bin width span panel). We also calculated the full width at half maximum (FWHM) and mode of the histogrammed photon ranges. While the mode, or peak, of the histogram is not strictly speaking a statistical moment, it is a simple metric for determining returned photons' general location. We found that the histogram peak range shifted location by more than 0.5 meters as the bin width of the histogram changed.

3.4.2 *Fitting exponentially-modified Gaussian function and associated standard errors*

Any number of photons can be used to generate distribution parameters (e.g., mean or standard deviation for Gaussian distributions, or mu, sigma, or tau for exponentially modified distributions); we use a Monte Carlo analysis to investigate the impact of sample size on the stability of these distribution parameters. Our Monte Carlo sensitivity analysis from a prescribed exponentially-modified Gaussian distribution shows similar results (Figure 3.5A) to the sensitivity study done by Lacouture and Cousineau. We also use the Monte Carlo sensitivity analysis with MABEL photon

returns from Spectralon (Figure 3.5B) and find similar results to the randomly sampled exponentially-modified Gaussian data in Figure 3.5A. In both cases, the values of all three of the exponentially-modified Gaussian parameters begin to change, and the standard error increase, for sample sizes less than 5000.
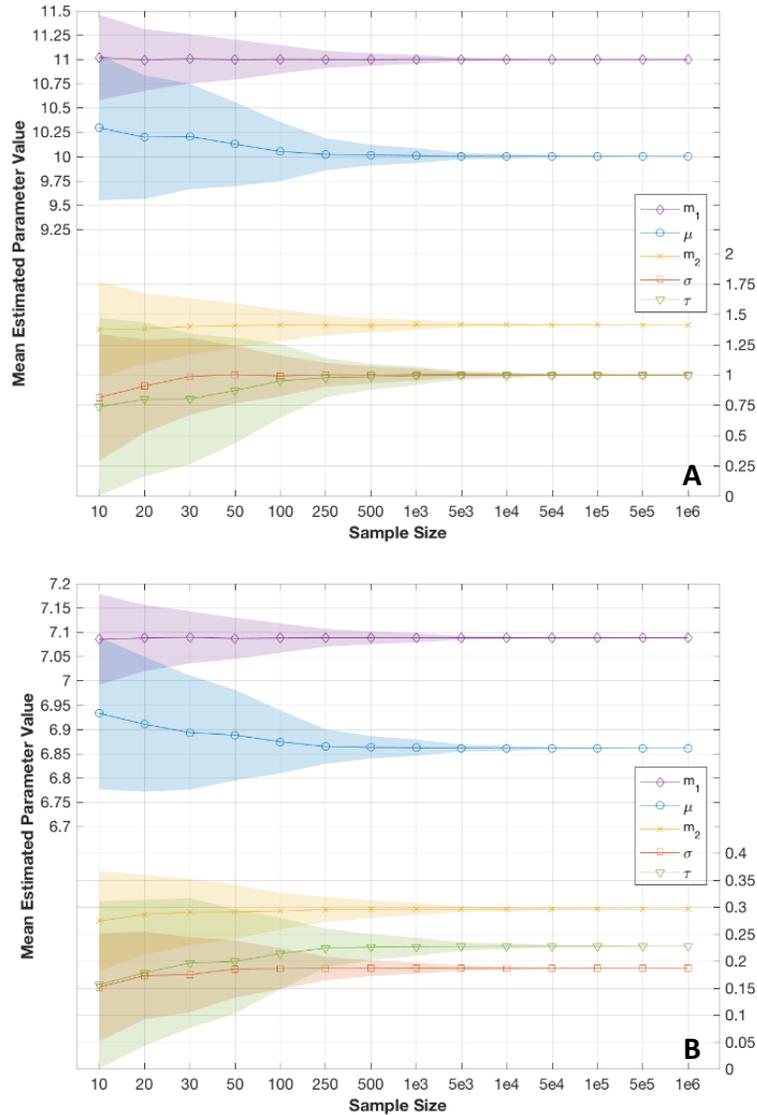
Figure 3.5:   Mean and standard error of estimated exponentially-modified Gaussian parameters (μ, σ, τ), and arithmetic mean (m1) and standard deviation (m2) calculated from a Monte Carlo sampled prescribed exponentially-modified Gaussian distribution (A) and from Monte Carlo sampled MABEL photon returns from a Spectralon reflectance standard panel (B).

3.4.3 Sample size influence on parameter precision

While the standard errors in Figure 3.5 give an indication of how variable a parameter

calculated from a given sample size can be relative to the parameter's expected value,

it doesn't provide the likelihood of a parameter being within a specified distance from
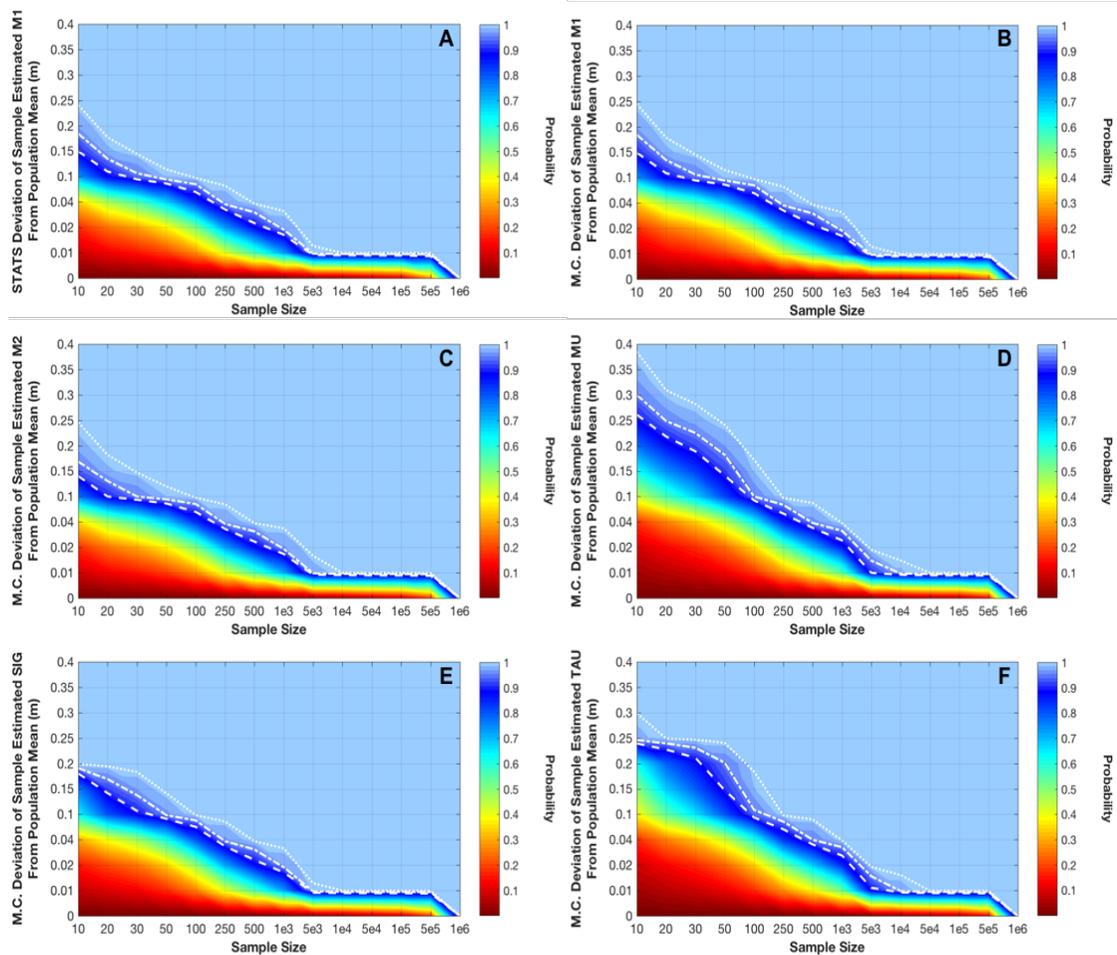
Figure 3.6: probability that a parameter value calculated from a sample with size (n) given by the x-axis is within the distance specified on the y-axis, of the population parameter value (n = 1 million). Probabilities in panel A are calculated using an equation for determining the required sample size for estimating the mean of a population within a specified distance of the population mean with a given probability. Panels B-F calculate probabilities by determining the fraction of our Monte Carlo generated sample parameter estimates within the specified distance of the population mean. The estimated parameter probabilities in panels B-F are: arithmetic mean (B), standard deviation (C), exponentially-modified Gaussian parameters mu (D), sigma (E), and tau (F). The white dashed lines are the 95% probability level, dot-dashed lines the 98% probability level, and dotted line the 99% probability level.

its expected value. We therefore use random sampling principles to compute the probability that the parameter value calculated from a given sample size will fall within a specified distance from the population mean (Figure 3.6). In Figure 3.6A, we calculate the probability (color bar) of the statistical mean calculated from a sample size (x-axis) having a value that lies within +/- a specified distance (y-axis) from the expected population mean using equation 3.3. In Figure 3.6B, rather than computing the probability using a known equation, we determine the fraction of sample means calculated from our Monte Carlo analysis that fall within +/- the specified distance of our population mean. We use this method to calculate the probability that Gaussian parameters, such as the mean (3.6B) and standard deviation (3.6C), as well as exponentially-modified Gaussian parameters mu (3.6D), sigma (3.6E), and tau (3.6F) fall with +/- some distance from the expected parameter value of the population.
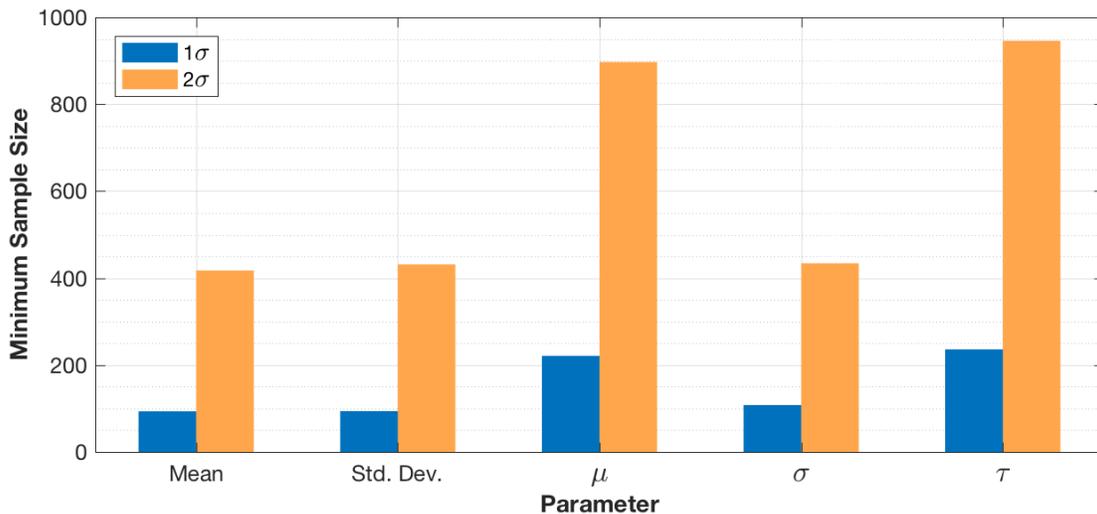
Figure 3.7: Minimum number of photons needed to calculate the specified parameters within 3 cm of their parent population values with a probability equal to the 1-sigma and 2-sigma confidence intervals.

Similarly, we can calculate the sample size needed to calculate each distribution parameter within 3 cm of the expected parameter value from a parent population with a probability equal to the 1-sigma confidence interval. We arrive at this sample size by interpolating the results used to produce Figure 3.6, and plot them in Figure 3.7.

3.4.4 Application to sea ice lead

To apply our methods to a real-world scenario, we use the sea ice lead highlighted in Figure 3 of Kwok et *al.*, 2014, and recreated here in Figure 3.8, to measure the IIRF over a sea ice lead using MABEL data. We use one section of specular photon returns from the lead (highlighted in the blue box) to calculate sample size precision
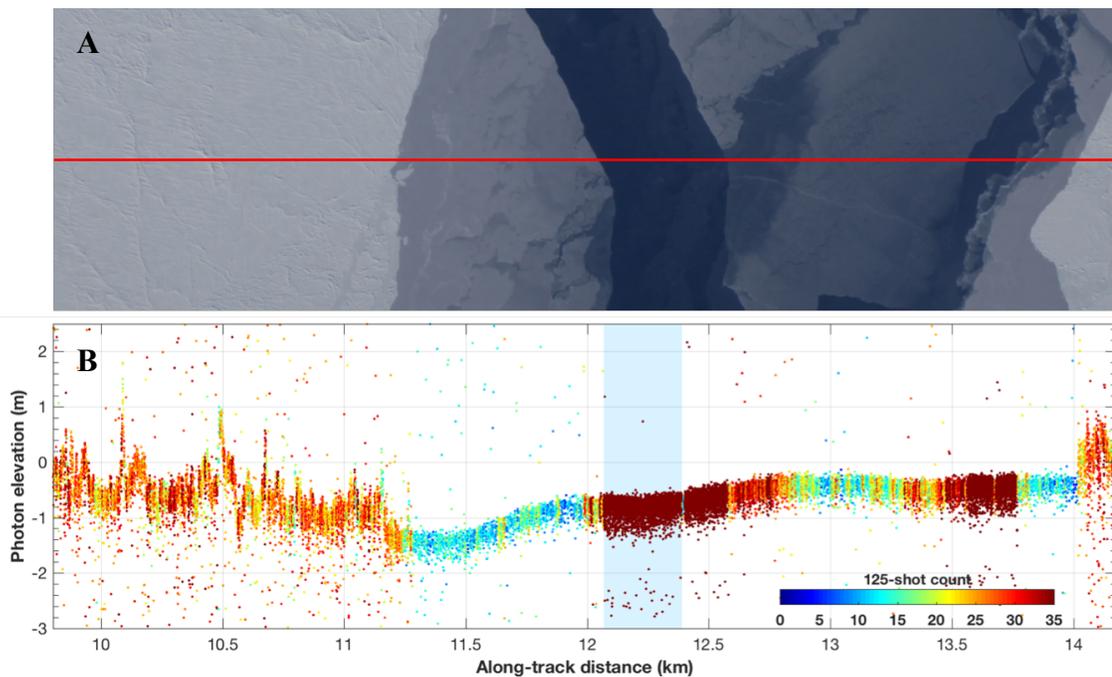
Figure 3.8: (A) DMS image from April 25, 2012 MABEL flight, showing sea ice lead highlighted in Kwok et al., 2014. The red line approximates the ER-2 ground track. (B) MABEL photon returns (dots) over area shown in DMS image. Photon returns are colored respective to the number of neighboring photons within a 125 laser shot range centered on each photon. Light blue box highlights the specular return photons used in our analysis.
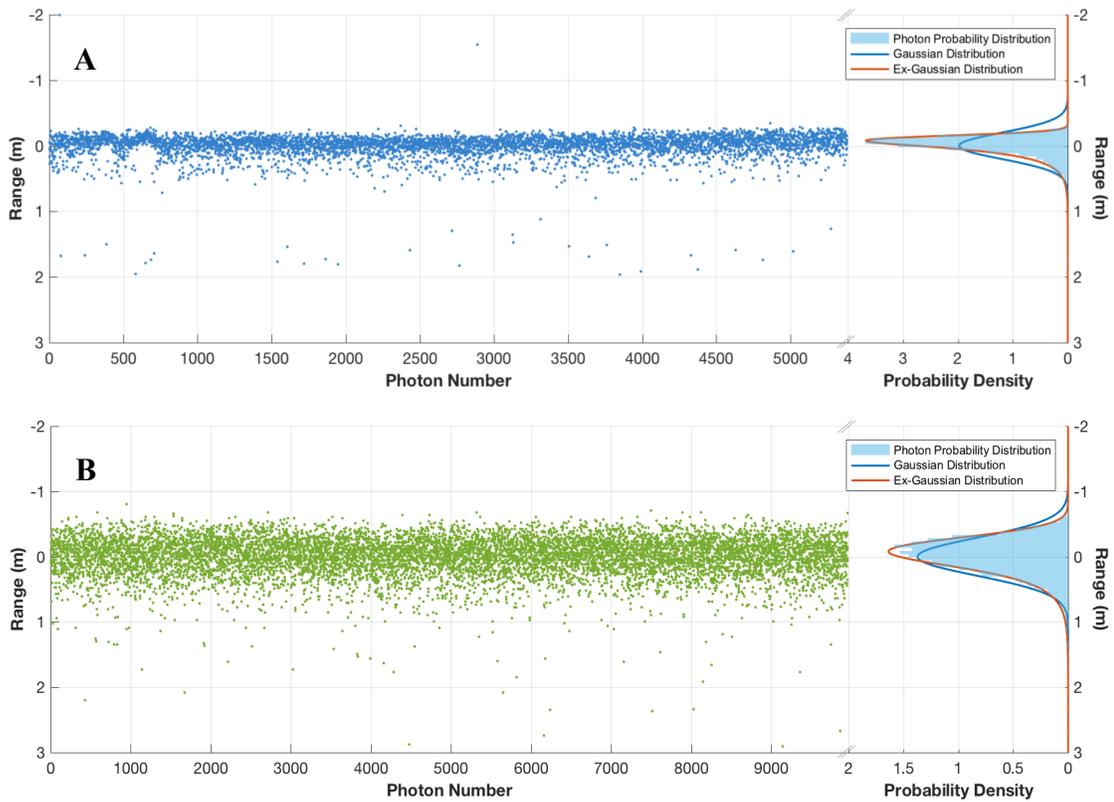
Figure 3.9: (A) MABEL recorded specular photon returns over sea ice lead from the blue highlighted box in Figure 8B, with associated photon probability density (light blue histogram at right). Gaussian probability distribution (blue line at right) is calculated from the mean and standard deviation of photon ranges plotted in the photon cloud. The fitted exponentially-modified Gaussian probability distribution is plotted in red. (B) Same as A, but using MABEL recorded photons in a laboratory using Spectralon as the target surface.

Table 3.1: Distribution parameters calculated from MABEL photon returns over sea ice off of northeast Greenland, and Spectralon in a laboratory

Distribution & Surface	RMSE	Location Moment (mu / mean)	Dispersion Moment (sigma / std. dev.)	Exponential Moment (tau / --)
SEA ICE				
Ex-Gaussian	0.5322	-0.1423	0.0574	0.1443
Gaussian	3.3726	0.0000	0.2018	N / A
SPECTRALON				
Ex-Gaussian	0.4090	-0.2217	0.1777	0.2217
Gaussian	0.9093	0.0000	0.2910	N / A

following the methods used to produce Figure 3.6. Figure 3.8A is a DMS camera image from the ER-2 carrying MABEL with the approximate ground location of beam 6 highlighted in red. Figure 3.8B shows the photon elevation cloud, with each dot representing a photon return. Dots are colored by counting the number of photons detected within the surround 125-laser shots (i.e., the 64 laser shots before and after a given shot). In Figure 3.9A, we zoom in on the highlighted specular return in Figure 3.8B, and plot the photon cloud with photon probability distribution plotted to the right (light blue histogram to the right of the photon cloud). In the same side panel, we also plot the Gaussian probability distribution calculated from the mean and standard deviation of the specular photon returns, and the fitted exponentially-modified Gaussian probability distribution. For comparison, we plot a section of photon returns from laboratory measurements over Spectralon (Figure 3.9B), with associated Gaussian and exponentially-modified Gaussian distributions also plotted to the right.

3.5 Discussion

3.5.1 Histogram sensitivity to bin width and other limitations

There are two competing goals when aggregating photon returns into a histogram to characterize the return pulse measured by a photon-counting instrument: (1) using small histogram bin widths to provide a detailed description of the impulse response, and (2) having enough photons in histogram bins to capture the shape of the impulse response in a statistically meaningful manner. This issue is illustrated in Figures 3.1 and 3.2. We assert that the shape of the histogram is limited by the number of photons used to generate the histogram, and the location and width of the bins used to sort the photon returns. We also show (Figure 3.4) that the statistical values describing the histogram shape vary around the values described by the exponentially-modified Gaussian distribution.

The histogram derived data used to calculate Figure 3.4 is useful for characterizing and quantifying visibly obvious changes in histogram shape. Of particular interest for use in characterizing the impulse response of MABEL are the skewness, kurtosis, and FWHM. The skewness of the histogram changes as a function of bin size, swinging from negatively skewed for bin widths near 0.9 m, to strongly positive skew near bin widths of 0.8 m, and appearing Gaussian (skewness = 0) when bin widths are approximately 0.85 m and 0.65 m wide. In contrast, when the skewness is calculated directly from all of the photons (dashed lines) rather than being histogrammed (solid lines), we see that the photon returns have a skewness of approximately 1. The

FWHM also depends on histogram bin width, changing by approximately 1 m. Particularly noteworthy are the changes seen for bin widths between 0.3 and 0.7 m, where the histogram FWHM deviates approximately 0.5 m from the dashed blue line (the FWHM of an exponentially-modified Gaussian distribution calculated using all the photon returns).

A potential solution to avoiding variability in values of skewness or FWHM is to use smaller bin widths, which appear to converge to the value calculated directly from all photons. However, smaller bin widths result in few photons per bin for a given sample size. This is evident in the last panel (bin count range) in Figure 3.4, which shows the range of photon counts between the histogram bin with the most photons and the histogram bin with the least photons (excluding bins with zero photons). An example of this might be a histogram with the largest histogram bin containing 10 photons, and two bins with one photon each. In this case the "bin count range" would be 9. The significance of having a smaller bin count range with smaller bin widths is that while the horizontal resolution is improved, the shape of the histogram is flattened. Taken to the extreme, given a small enough bin width, a histogram could consist of bins with no more than one photon (provided all photon ranges are unique).

Given the high pulse-repetition rate of photon-counting altimeters (thousands of shots per second), the limitations noted above can be mitigated by aggregating more data. For laboratory-based data (Figure 3.4) this is a plausible solution. However, for data collected from an airborne or space-based platform, additional data aggregation

confounds the effects of surface impulse response heterogeneities (e.g. surface slope, roughness) with the instrument impulse response function. The same limitations exist when using histogram-based approaches to determining elevation from photon data: aggregating more data to generate histograms with small bins width to improve surface resolution can actually reduce the accuracy of the elevation measurement due to changing surface conditions over the period of integration.

3.5.2 Exponentially-modified Gaussian function standard errors

Although developed for substantially different purposes, the exponentially-modified Gaussian method of Lacouture and Cousineau (2008), analysis demonstrates that it is also useful for analyzing photon data. We replicated their Monte Carlo analysis of the standard error for each exponentially-modified Gaussian parameter by randomly sampling an exponentially-modified Gaussian distribution with prescribed parameter values. We also extended this standard error analysis to the arithmetic mean and standard deviation, and extended the range of sample sizes up to 1 million (Figure 3.5A). We repeated the standard error analysis using MABEL photon returns from a Spectralon reflectance panel (Figure 3.5B), in which we see similar increases in standard error with decreasing sample sizes as observed in the standard errors from the prescribed exponentially-modified Gaussian analysis. It is interesting to note, though not surprisingly, that as sample size decreases, the exponentially-modified Gaussian parameter mu appears to approach the value of the arithmetic mean. This analysis confirms that MABEL photons have similar standard errors to random samples from a known exponentially-modified Gaussian distribution, and that the

mean and standard deviation parameters behave similarly to the exponentially-modified Gaussian parameters.

3.5.3 Sample size and parameter precision

Although the standard error provides some estimate of the variability in parameter calculations as a function of sample size, Figure 3.6 shows the Monte-Carlo based probability that a distribution parameter (i.e., the mean or standard deviation for Gaussian distributions, or mu, sigma, or tau for exponentially-modified Gaussian distributions) calculated using a specified sample size would be within some distance (d) of the true value of that parameter given an infinitely large sample size. Statistical methods can be used to calculate the probability of the sample mean being within a certain distance of the true mean of a Gaussian distribution (Equation 6 and Figure 3.6A). To compute the probabilities for other parameters, such as those used by the exponentially-modified Gaussian distribution, we calculate the probabilities from our Monte Carlo analysis by determining the fraction of sample parameter means that lie within +/- d of the population parameter. Our estimations of the parameter probability for the sample mean using Monte Carlo analysis (Figure 3.6B) match well with the probabilities calculated using formal statistical analysis (3.6A). We then calculate parameter probabilities for the standard deviation, as well as the three exponentially-modified Gaussian parameters.

In addition to calculating the probabilities over a range of sample sizes and for several distances from the parent population value, we also evaluate a more practical case of

the sample size required to calculate both the Gaussian and exponentially-modified Gaussian parameters within 3 cm of the parent population value and within the 1-sigma confidence interval (Figure 3.7). We find that a minimum of 236 photons is required to calculate all parameters within this specified range, while 947 are needed to calculate both Gaussian and exponentially-modified Gaussain distribution parameters within the 2-sigma confidence interval. This analysis, along with Figure 3.6, provides a guide to the error due purely to sampling errors associated with sample size, and for calculating the IIRF for photon counting lidars.

3.5.4 Sea ice lead application

We extend this analysis to MABEL photon data collected over a lead in the Arctic Ocean in Figures 3.8 and 3.9. While the lead in this example is approximately 500 m wide, we only analyzed the specularly-reflected photos near the center of the lead covering a distance of approximately 320 m. Using the analysis above, we estimate the average along track distance needed to record 250 specularly-reflected photons within 3 cm of their parent population value and 1-sigma confidence interval to be 15 m. This provides an estimate of the lower width limit required to calculate the IIRF for both MABEL and ATLAS from a sea ice lead. Given the similarity in pulse duration for both MABEL and ATLAS (~1.5 nanosecond), we expect similar results for ATLAS using these methods. In addition to our analytical analysis, Figure 3.9 also highlights the advantage of using an exponentially-modified Gaussian distribution in the panels to the right of the photon clouds. Here, we can see that for both the sea ice lead and laboratory Spectralon photon returns, the received photon

range distribution is well characterized by an exponentially-modified Gaussian. Table 3.1 shows the RMSE between the light blue histogram bins on the right of Figure 3.9 and a Gaussian distribution (dark blue line) versus an exponentially-modified Gaussian distribution (red line), highlighting the exponentially-modified Gaussian distributions better fit.

3.6 Conclusions

The exponentially-modified Gaussian function offers a simple, objective, consistent, and mathematically robust method of describing the MABEL instrument impulse response function. By performing a Monte Carlo sensitivity assessment of the parameters defining an exponentially-modified Gaussian distribution, we are able to provide a standard error, and precision uncertainty estimates related to the sample size of the data used to calculate statistical and exponentially-modified Gaussian parameters. We used our results to analyze photon returns from a sea ice lead and estimated precision uncertainty due to sample size for the arithmetic mean and standard deviation, and for exponentially-modified Gaussian parameters. We found that aggregating 250 photons is required to provide precision uncertainties with 1-sigma confidence of being within the 3 cm precision of the expected parameter value. This analysis provides insight into expected limitations for ATLAS, and other photon-counting laser altimeters, by providing guidance for uncertainties associated purely with sample size when aggregating photons to characterize the IIRF.

Chapter 4: Altimeter measurements of snow in a laboratory

4.1: Introduction

NASA's upcoming ICESat-2 (Ice Cloud and land Elevation Satellite-2) mission (Markus et *al*., 2017) will quantify elevation changes of ice sheets, glaciers, and sea ice free board in Earth's polar regions using the laser altimeter ATLAS (Advanced Topographic Laser Altimeter System). To prepare for ICESat-2, NASA built MABEL (Multiple Altimeter Beam Experimental Lidar; McGill et *al*., 2013) as a simulator laser altimeter for ATLAS. As a single photon counting lidar, MABEL provides an opportunity to test and validate algorithms intended for use with ATLAS over a variety of surface types. Flying onboard the NASA ER-2 aircraft at altitudes of 20 km (above ~95% of Earth's atmosphere) provides MABEL an opportunity to observe the aggregate effects of the instrument system and environmental conditions on measured photon returns.

It is suspected that green light photons volume-scattered in snow could be detected by a laser altimeter system due to snow's low absorption of visible-wavelength light. The aggregation of these volume-scattered photons with photons reflected directly off snow surfaces would result in elevation estimates that are biased toward lower elevations (i.e., a range farther from the altimeter system). While at least one attempt to measure this effect has been made in the field (Gardner et *al*., 2015) using a similar

laser altimeter (SIMPL; Dabney et *al*., 2010), no attempt has been made using MABEL. Additionally, although MABEL has flown several field campaigns over the past several years to collect data for ATLAS algorithm development, there have been no efforts to characterize MABEL's systematic behavior in a controlled laboratory environment.

In this study, I explore the effect of volume-scattered photons on MABEL range measurements by comparing photon returns from a volume scattering surface, snow, and a non-volume scattering surface, a Spectralon reflectance standard panel. Comparing photon returns from these two surfaces in a controlled laboratory setting should provide the best opportunity to quantify effects of volume scattering in MABEL data. I also use several different snow grain size distributions to ascertain if volume scattering within snow is affected by the snow grain size, and if this effect is measureable by the laser altimeter system. Finally, I assess the time-varying stability of MABEL's pulse shape and photon return distribution by analyzing photon returns from a Spectralon panel using a 1-minute moving average.

4.2: Methods

4.2.1 MABEL configuration

We made several modifications to MABEL's viewing configurations to enable measurement of photons in a laboratory setting. MABEL typically flies on the ER-2

at a nominal operating altitude of 20,000 m and aligned so that the transmitted laser footprint and receiving telescope field of view are aligned at the surface. Targets for measurement in the laboratory would, in contrast, only be positioned several meters from MABEL and as such, the receiving telescope field of view would not overlap with the transmitted laser pulse. Additionally, beam divergence results in a laser footprint of 2 m when MABEL is operated at 20,000 m. The resulting footprint in the laboratory would be small enough such that the laser beam directly illuminates only one snow grain. This could cause other snow grains to be "shadowed," producing irregular returns. MABEL is also typically configured to have "range gates" to ignore photons returns outside the expected time of return from the surface. As a result, we had to reset the range gates to accept photons from ranges less than 10 m.

Realigning MABEL's nominal transmitting and receiving telescopes for laboratory was not feasible, as it could adversely affect any future measurements if MABEL was flown on a field campaign again. Instead, we built a simplified transmitting and receiving telescope for individual transmitting and receiving optical fibers (Figure 3.3), so that we could circumvent MABEL's built in telescope assembly. The simplified telescope consisted of an optical fiber mounted into a collimating lens held in an optical
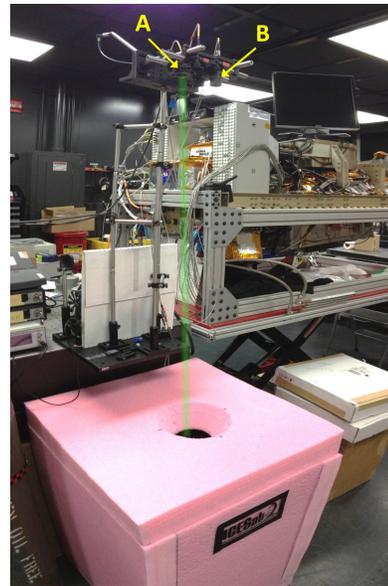
Figure 4.1:   MABEL transmit/ receiver telescope set-up with insulating box. A points to the simple transmit telescope, while B points to the simple receiving telescope.

tilt mount, allowing us to fine tune the pointing of the transmitting and receiving fibers. We used two collimating lenses with different focal lengths to ensure the field of view of the receiving fiber was larger than the footprint of the transmitting fiber. The tilt mounts were attached to a small breadboard (4" by 6") to ensure consistent separation. We used optical posts to raise the breadboard with the simple telescope 1.5 meters above the expected height of target surfaces. The transmitting fiber footprint and receiving fiber field of view were aligned by swapping the receiving fiber with a second transmitting fiber, and producing a receiver footprint on the target surface. We aligned the receiver field of view footprint so that it fully contained the transmitted footprint, and then replaced the second transmitting fiber with the original receiving fiber.

Taking measurements in a laboratory also presented the challenge of preventing saturation on MABEL's detectors. MABEL has one detector, a single photomultiplier tube, for each receiving fiber. The photomultiplier tubes have a "dead time" needed to recover after detecting a photon, during which they are unable to detect additional photons. If the average rate of photons reaching a detector is high enough that a significant number of photons are arriving while the detector is recovering from previous photon detections, the detector considered saturated. While the saturation rate for MABEL is not precisely known, 0.5 photons per shot is generally thought to be the lower average photon return rate needed to saturate MABEL's detectors (personal communication with Bill Cook).

To prevent detector saturation during normal operation on the ER-2, the atmosphere scatters and absorbed enough photons so that saturation is only a concern over highly reflective targets such as snow and ice surfaces. In the laboratory, we are not only using highly reflective snow surfaces as our target, but the laser only travels through approximately 3 m of air on its round trip to the target surface and back to the receiving fiber. As a result, several neutral filters were placed in front of the receiving fiber to ensure the maximum average photon return rate was below the detector saturation rate. For measurements over snow surfaces, I used three neutral density filters to keep the average photon return rate below 0.2 photons per shot.

MABEL's pulse repetition rate (the frequency at which the laser fires) was set to 5 kHz. With a goal of a 0.1 to 0.2 average photon per shot return rate, a 5 kHz repetition rate generated between 30,000 and 60,000 photon returns per minute.

4.2.2 Snow

The snow used for the MABEL laboratory measurements was originally collected at Summit, Greenland in 2008. Originally used to pack ice cores for shipping to the United States, no special care was taken to minimize contamination of the snow during collection, or that the snow was particularly clean to begin with. The methods used to characterize and quantify the impurity content of the snow can be found in more detail in chapter 2, section 2.2.3. The snow sintered after sitting unused for more than two days, requiring it to be "de-sintered" into individual snow grains using a standard household box cheese grater. I mechanically separated the snow into grain

size distributions using a stack of Gilson geological sieves. A detailed description of the de-sintering and sieving process can be found in chapter 2, section 2.2.2. We contained the snow in the same test-bed used to make the transmission measurements in chapter 2 (see section 2.2.1 for test-bed design details). All measurements made with MABEL using snow as the target surface had a snow depth of 7 cm. This depth was dictated by the maximum amount of snow remaining from any one of the snow grain distributions, to ensure the same depth could be made across all snow grain distributions. However, because the snow depth was only 7 cm, I was able to add a fourth snow grain size distribution to our measurements. This fourth distribution was larger than the three used in measuring transmission, with diameters ranging from 1.4 mm to 2.0 mm. The list of snow grain distributions used is listed in Table 4.1.

Figure 4.2: Snow insulation box schematic. Grey ovals on left are cold packs used to maintain sub-freezing temperatures. Test bed holding snow was centered under the lid opening.

Table 4.1: Snow grain distributions used for MABEL laboratory measurements

Distribution short name	Minimum diameter (mm)	Maximum diameter (mm)	Minimum diameter SSA ($m^2 \cdot kg^{-1}$)	Maximum diameter SSA ($m^2 \cdot kg^{-1}$)
small	0	0.5	0	5.5
medium	0.5	1.0	5.5	2.8
large	1.0	1.4	2.8	2.0
extra-large	1.4	2.0	2.0	1.4

The snow was stored in a cold room at -20 C when not used for measurements. While planning to make MABEL measurements of snow in the cold room would be ideal to ensure the snow didn't melt, safety regulations necessitated MABEL be operated in a laboratory certified for using class IV lasers. As a result, I developed a method for insulating the snow to keep the snow from melting. I constructed a double-walled box using insulating foam board (Figure 4.2), designed to fit around the test-bed used for to make the transmission measurements in chapter 2. Two walls of the box had mounts to accommodate cold packs to help maintain sub-freezing temperatures in the box. The cold packs were stored in a -80 C chest freezer to allow for maximum time to take measurements using MABEL. The interior dimensions of the box were 30 cm wide by 30 cm deep, and 68 cm tall. To prevent cold air from pooling at the bottom of the box and warm air melting snow near the top of the box, I placed a computer case fan halfway down one of the interior walls of the box and connected it to a peripheral power port on the data logger used to monitor the air temperature in the box. This provided adequate air circulation to achieve uniform air temperature between the top and bottom of the box. Thermocouples located at the top and bottom of the box, as well as at the surface of the snow, allowed for real time monitoring of the air temperature inside the box while MABEL measurements were made to ensure the air remained below freezing. A conical opening cut into the lid of the foam box allowed MABEL measurements to be made while keeping the snow insulated from the room temperature MABEL laboratory. The opening was subsequently covered when measurements were not actively being taken. The interior walls of the box were painted black to reduce the amount of light scattering off surfaces other than snow.

4.2.3 Data collection and analysis

Measurements were made with the room lighting turned off to minimize the amount of background photons measured by MABEL. To monitor for range walk (i.e., a drift in the recorded photon ranges not associated with a physical change in range to the target surface), I bookended the snow measurements with measurements of a Spectralon standard reflectance panel: a uniform, Lambertian-reflecting surface, with a 99% calibrated reflectance. The Spectralon panels were placed on a cooled, metal ruler just above the snow surface, so as not to disturb the snow surface. The thickness of the ruler and Spectralon panel was measured with a caliper and this distance bias (multiplied by two to account for round trip travel distance for photons) was added to the Spectralon photon return ranges.

While there was no way to monitor the number of photons recorded in real time, I was able to estimate the number of photons recorded by monitoring the rate at which MABEL's hard drive sectors were being written as data was recorded. In this way, I was able to ensure that approximately 1 million photon returns were recorded over snow targets, while recording approximately 500,000 photons from the Spectralon target.

To compare photon returns from Spectralon to those from snow, I fit an exponentially-modified Gaussian function to the photon returns from each surface following the method of Greeley et *al*., 2018. A detailed description of the procedures is also outlined in chapter 3 section 3.3.3 of this dissertation. Additionally, I

calculated the arithmetic mean and standard deviation of the photon return ranges. To assess variations in MABEL's performance while measurements were taken, I calculated a one-minute moving average of the exponentially-modified Gaussian parameters, the mean and standard deviation, the FWHM, and the number of photons recorded per laser pulse (photons per shot).

4.3: Results

I recorded at least 1 million photon returns from each of the four snow grain distributions and compared them to one of the bookending Spectralon returns after
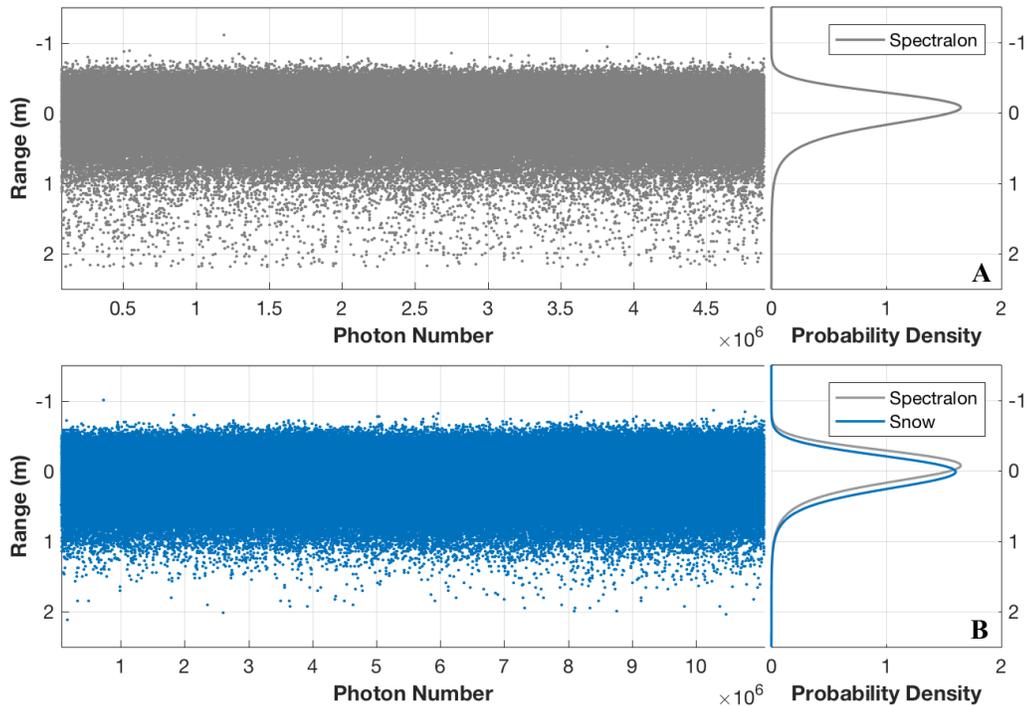
Figure 4.3: (A) MABEL photon return cloud from a Spectralon reflectance panel (left) and fitted exponentially-modified Gaussian function (right). (B) MABEL photon return cloud from the snow from the medium snow grain distribution (left) and fitted exponentially-modified Gaussian function (right). Spectralon exponentially-modified Gaussian distribution also plotted for comparison. Negative range values are closer to the altimeter.

adding the range bias equivalent to the thickness of the Spectralon panel to the Spectralon photon return ranges. A typical Spectralon return is shown in Figure 4.3A. Photon returns from snow from the medium snow grain distribution are show in Figure 4.3B, with the associated Spectralon return plotted in grey for comparison.

I also compute the one-minute moving average of the arithmetic mean (M1), standard deviation (M2), full-width half-max (FWHM), as well as for the exponentially-modified Gaussian parameters mu (μ), sigma (σ), and tau (τ) for the measurements of the medium snow grain distribution and the two bookend Spectralon measurements (Figure 4.4). These show that there is variability on the order of centimeters in each of the parameters over the course of the measurements. These parameter variations are shared for all snow grain distributions and Spectralon measurements. In no case,
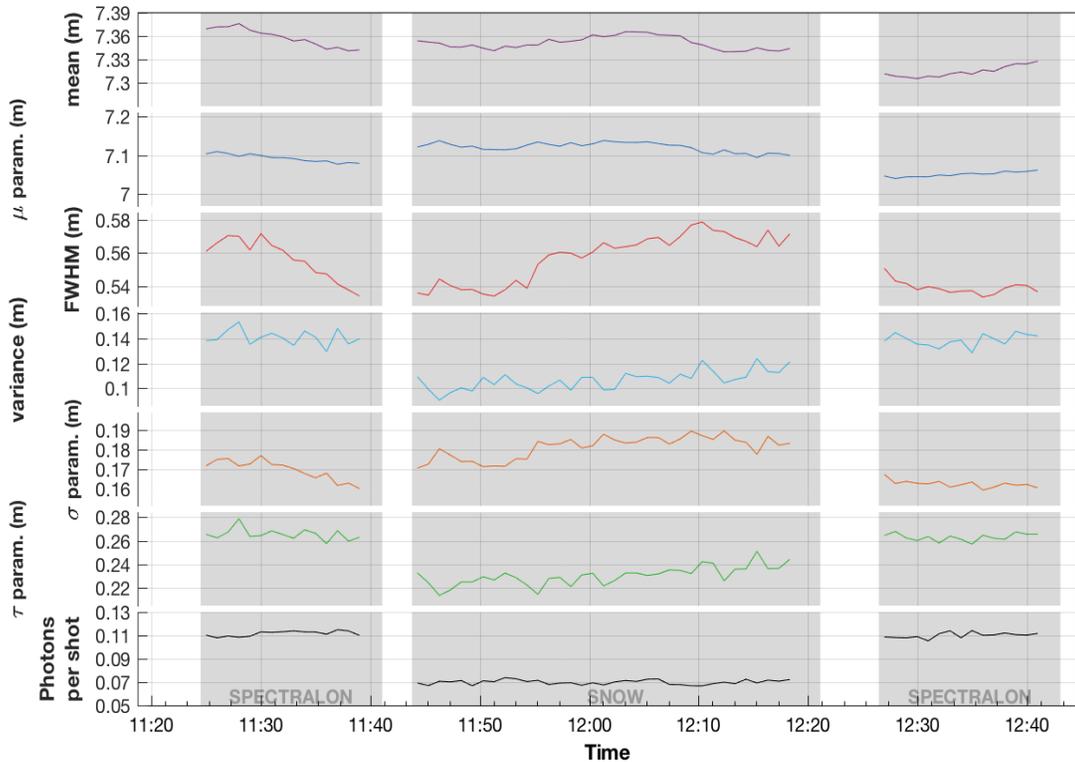
Figure 4.4: Time variations in distribution parameters derived from MABEL photon returns

was there a clearly distinguishable trend in the parameters over the course of measurements.

To compare photon returns from different snow grain distributions made on different days, they must be normalized to a common range. To start, I choose one of the Spectralon bookend measurements and remove the mean photon return range (i.e., the mean range becomes zero). I then remove the mean Spectralon photon range from the photon returns over snow. This was repeated for each snow grain distribution for each snow grain measurement and its associated Spectralon measurement. I then fit an exponentially-modified Gaussian function to the returns from snow and normalized the probability distribution to the ratio of the mean photon return rate for the snow sample relative to the mean photon rate for the associated Spectralon sample (Figure 4.5).
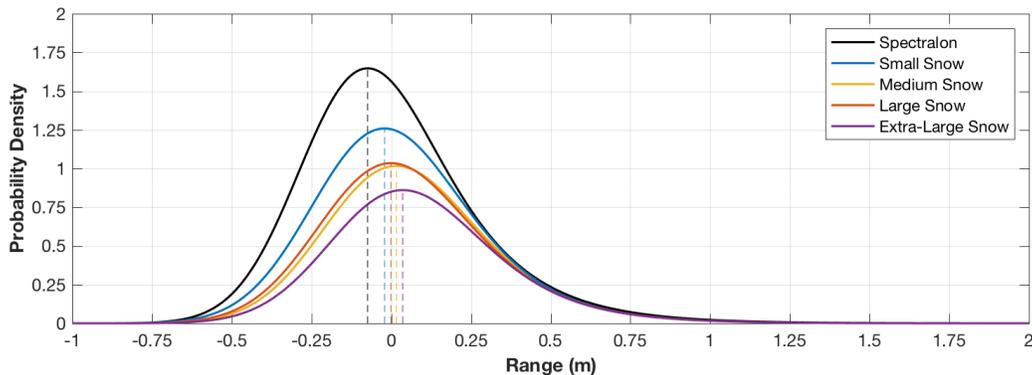
Figure 4.5: Comparison of MABEL photon returns from several snow grain size distributions to Spectralon photon returns. Returns are normalized to the mean photon return rate relative to the Spectralon mean photon return rate. Negative ranges are closer to the altimeter.

The relative photon return intensities generally decrease with increasing grain size, with the exception of the medium and large snow grain size distributions.

Additionally, the offset of the snow return peaks, relative to the Spectralon return peak, increase with increasing grain size, again except for the medium and large snow grain distributions. The separation between return peaks is given below in Table 4.2.

Table 4.2:   Snow size distribution (e.g., small) return peak distance from Spectralon return peak in meters

Small	Medium	Large	Extra-Large
0.053	0.090	0.073	0.110

In addition to comparing the return peak ranges, I also assess how the width parameters (sigma and tau) change between Spectralon and snow targets in Figure 4.6. For Spectralon returns, tau (the measure of how asymmetrical the photon returns are) is larger than sigma (the measure of how symmetric spread in the photon returns). In contrast, sigma is larger than tau for photon distributions returning from
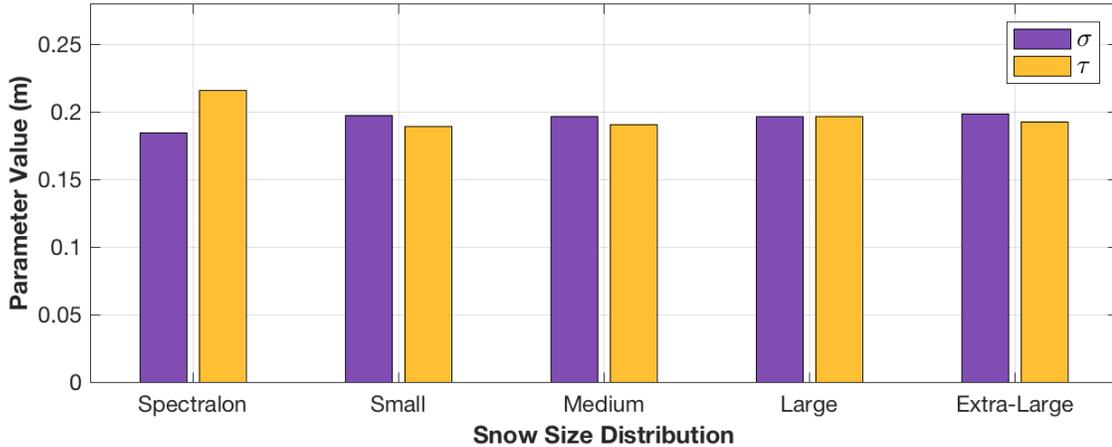
Figure 4.6:   Parameters for exponentially-modified Gaussian distribution parameters sigma (left bar pair) and tau (right bar pair). While the tau parameter is larger than sigma for photon returns from Spectralon, the opposite relationship occurs for photon returns from snow. The exception is for photon returns from the large snow grain distribution in which the parameter values are nearly the same (sigma = 0.1966, tau = 0.1968).

snow, with the exception of large snow grain distributions for which sigma and tau are nearly the same. While there does appear to be a difference in the shape of photons returning from Spectralon compared to snow targets as described by sigma and tau, there does not appear to be a change in these parameter values associated with photon returns from different snow grain size distributions.

4.4: Discussion

The time varying plots of distribution parameters show that there is a significant amount of variability in photon range as measured by MABEL that is not attributable to a physical change in range from MABEL to the target surface. The one-minute moving averages of both the mean photon range and mu parameter calculated from the exponentially-modified Gaussian distribution exhibit range walking of up to 5 cm. This variability is not associated with statistical uncertainty in the calculated parameters as 1-minute of photon returns at a rate of 0.1 photons per shot, with a pulse repetition rate of 5 kHz results in 30,000 photons per minute. As discussed in chapter 3, 30,000 photons produce very robust distribution parameter estimates for both Gaussian and exponentially-modified Gaussian distributions. This suggests that the variations in 1-minute moving average parameter values must be due to electronic, and/or thermal variations of internal MABEL components. Given access to MABEL "house-keeping" data (internal thermal and electronic data), it may be possible to isolate and correct for some of these non-physical variations in photon range, however, that analysis is beyond the scope of the present study.

There is a visible shift in the photon return distributions from snow compared to Spectralon (Figure 4.3B), due to photon volume scattering in the snow. While it appears that most photons return from the snow surface as the main shape of the snow returns is the same as from Spectralon, photons that scatter within the snow before scattering back out are delayed relative to photons that reflect directly off the snow surface. The volume-scattered photons' delay manifests itself as the photons appearing to have travelled farther from the altimeter than those reflected off the surface. As a result, they "drag" the return pulse farther away from MABEL than the Spectralon returns. While I had expected the volume-scattered photons to significantly extend the tail of the snow returns, this effect is not discernable in my measurements. Rather, the distributions of return photons from snow seem to shift farther away from MABEL while broadening slightly as a whole. This is evidenced by the increase in the sigma parameter between Spectralon (indication of symmetric broadening) and snow surfaces in Figure 4.3, while the tau parameter (which defines the asymmetric tail component of the exponentially-modified Gaussian distribution) decreases from Spectralon to snow surface returns.

In addition to a shift in the range of photon returns from different snow grain size distributions, the average photon per shot return rate also appears to change with snow grain size. The average photon per shot return rate is comparable to snow reflectance when compared to a known reflectance standard, such as the Spectralon reflectance panels. Smaller snow grains have a higher average photon returns per shot

rate than larger snow grains. This is consistent with the snow reflectance measurements made with an ASD hyperspectral radiometer in chapter 2. The exception to this are the photon returns from the medium and large snow grain distributions, which are nearly the same.

Figure 4.5 shows that photon returns from the smaller snow grain distribution are shifted away from the altimeter less than the larger snow grain distributions. Larger snow grains transmit more green light than smaller snow grains (as shown in chapter 2), and as such, photons are able to travel longer distances in the larger snow grain distribution without being absorbed, or scattered out of MABEL's field of view. The exception to this are the medium and large snow grain distributions, which appear to have swapped places. The reason for this seeming reversal in expected shift due to volume scattering is not clear. However, the two return distributions are very close to each other in both range and amplitude, so it is possible that experimental uncertainty, or range walk due to internal variations in MABEL, may be the cause of this departure from expectations, rather than a physical mechanism. The issue of range walk, in fact, draws into question the true magnitude in the measured shift of the snow photon returns. With range walking of up to 5 cm visible in the 1-minute moving average of the mean and mu distribution parameters seen in Figure 4.3, and a shift in peak location from 5.3 cm for the small snow grain distribution to 11 cm for the very large distribution, the ability to confidently state that the snow return pulses are truly discernable from each other is questionable.

While range walk complicates the analysis of photon returns range bias from different snow grain distributions, the exponentially-modified Gaussian width and asymmetry parameters (sigma and tau respectively) may still yield some insightful information. Photon returns from Spectralon are characterized by a larger value for the sigma parameter than the tau parameter. This characterization seems to reverse for photon returns from snow targets (with the exception of photon returns from the large snow grain distribution). Additionally, the value for the sigma parameter is consistently larger for photons returning from snow than from Spectralon, while the tau parameter value is consistently lower over snow targets than Spectralon. The physical implications for this suggest that the distribution of photon returns over snow are symmetrically broader than over Spectralon, and that the distribution is overall more symmetrical over snow than Spectralon. This is counter to the expectation that photons scattering in snow would increase the asymmetry of the photon return distribution relative to photons returning from a target without volume scattering, such as Spectralon. One possible explanation is that photons scattering in the snow from the middle of the laser pulse (which has the greatest number of photons) are delayed due to volume scattering such that they overlap and dominate the few trailing photons from the initial laser pulse, making the return pulse look more symmetric.

4.5: Conclusions

MABEL was modified to allow for laboratory ranging measurements to Spectralon and snow target surfaces by building a simplified transmitting and receiving telescope

platform. Ranging measurements to Spectralon and snow targets show that photon volume scattering within snow targets produces a positive range bias in the returning photons that makes the photon return distribution appear 5 to 10 cm farther away from MABEL than the snow surface actually is, depending on the snow grain size. Photon returns from larger snow grains are shifted farther away from the true surface than smaller snow grains. However, uncertainty in the relative change in range associated with snow grain size, due to range walk in MABEL's measurement of photon ranges, prevents the determination of an exact relationship between snow grain size and shift in return photons due to volume scattering. Although range walk complicates the relationship between photon returns from different snow grain size distributions, a clear difference is seen in the relationship between the exponentially-modified Gaussian distribution shape parameters for photon returns from Spectralon versus snow targets: photon return distributions from over Spectralon are more narrow and asymmetrical than distributions from over snow.

Chapter 5: Modeling Photon Scattering in Snow

5.1: Introduction

While measurements from MABEL indicate some influence of volume scattering in snow on recorded photon returns, there does not appear to be an immediate unique solution to the results. For example, a shift in the peak of the measured return pulse could be due to a small number of volume-scattered photons with large path lengths, or a large number of volume-scattered photons with small path lengths. The implications for these two scenarios is that if few photons with large path lengths are creating this shift in the return pulse peak, then it is less likely that these photons will be detected during normal operations in the field. As a result, other factors such as slope and surface roughness will dominate photon returns before enough volume-scattered photons with large path lengths measured in sufficient quantity to affect elevation estimates. On the other hand, if a large number of photons have shorter path lengths, it is more likely they will be recorded by the laser altimeter, and may influence elevation estimates. One method for exploring this difference is to develop a photon scattering model that reasonably replicates the photon scattering process in snow, and use its results to track the paths of individual photons as they scatter through snow.

In this chapter I develop a photon path tracking, radiative transfer model, ELSA (Experimental Light Scattering Application), in Matlab to track the path length of photons scattered in snow. While other models that have been developed to simulate the transmission or albedo of snow packs with varying snow grain sizes and impurity contents, none that I have found have the ability to track and individual photon's scattering path through snow. This tracking of individual photons is necessary for our purposes when comparing results to single photon counting laser altimeters such as MABEL and ATLAS. ELSA is validated using the transmission profile measurements from chapter 2, and is then used to explore the likely path length distribution of photons measured by MABEL. Results indicate that most photons return from the first 1 to 2 cm of snow and have path lengths less than 10 cm. The rate of photon returns with path lengths sufficiently long enough to influence elevation estimates on a shot-by-shot basis is small, and as such, a minimal effect on surface elevation estimates from these photons is expected.

5.2: Model design and implementation

5.2.1 Boundary condition

The model is designed as a 2-dimensional simulation of photons propagating through a scattering medium. To validate the model, I compare model simulations of transmission through snow with the results from the laboratory measured transmission profiles described in chapter 2. The model boundary conditions (Figure 5.1) are designed to match the physical dimensions of the snow test-bed used to make
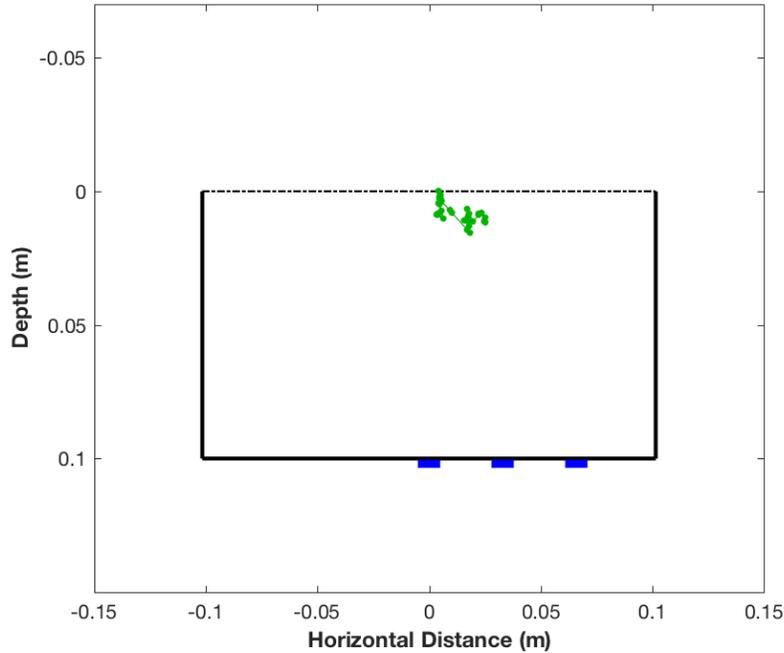
Figure 5.1: ELSA test bed layout. Blue rectangles indicate the position of detectors in the floor. The dashed horizontal line represents the snow surface in the model. The green line indicates the path of a single simulated photon. Green circles are plotted at each scattering event.

the transmission measurements described in chapter 2. Simulated photons are randomly assigned a lateral starting position within a 1 cm range representative of the laser beam impingent on the snow surface. All photons are given a starting vertical position of zero; equal to the top of the snow surface.

During simulations, the model keeps a record of a photon's past and current vertical and horizontal positions while a photon remains within the boundaries of the snow as defined by the snow surface, the test-bed walls, and floor. The diameter of the test-bed was 20.32 cm, with walls and floor painted black to minimize light reflections. Similarly, the side boundary conditions are 20.32 cm apart, while the distance from the floor to the snow surface is dependent on the designated snow depth. For both the

walls and floor in the model, a photon is absorbed completely if either boundary is intersected by the photon path. If a photon's vertical position extends above the snow surface, it is considered lost and simulation of its path is terminated.

5.2.2 Scattering mechanics

With each photon starting at the snow surface, several calculations are made to determine the location of its next scatting event: path length, scattering angle, and whether the photon is absorbed by impurities in the snow. The path length to the next scattering event is controlled by the bulk extinction coefficient for snow (χ) as defined in equation 5.1 (their equation 23) from Bohren and Backstrom (1977):

$$\chi = \left(\frac{3}{4r}\right)\left(\frac{\rho_{snow}}{\rho_{ice}}\right) \qquad (5.1)$$

where r is the snow grain radius, and ρ_{snow} and ρ_{ice} are the bulk densities for snow and ice respectively. This bulk extinction coefficient accounts for light attenuation through snow due to light scattering out of the direct path to the illumination source, and absorption by ice. The snow densities used were measured during the transmission made in chapter 2 (see Figure 2.5 in section 2.3.1). Using the Beer-Lambert law (equation 5.2) and the bulk snow extinction coefficient, the photon path length can be calculated as follows:

$$I = I_o exp^{-\chi s} \qquad (5.2)$$

where s is the photon path length, I_o is the intensity of light incident at the surface of the snow (i.e., no snow cover), and I is the intensity of light for a given snow depth. For the transmission measurements made in the lab, as well as the simulations of transmission made here, I is measured directly below the footprint of the illuminating laser at the snow surface. Equation 5.2 can be rearranged to solve for path length:

$$s = -\frac{\ln\left(\frac{I}{I_o}\right)}{\chi} \tag{5.3}$$

In this configuration, the ratio of I to I_o is always a fraction between 1 and zero. This relationship allows me to calculate a path length to each new scattering event by using a random number generator determine the value of this ratio each time a photon scatters.
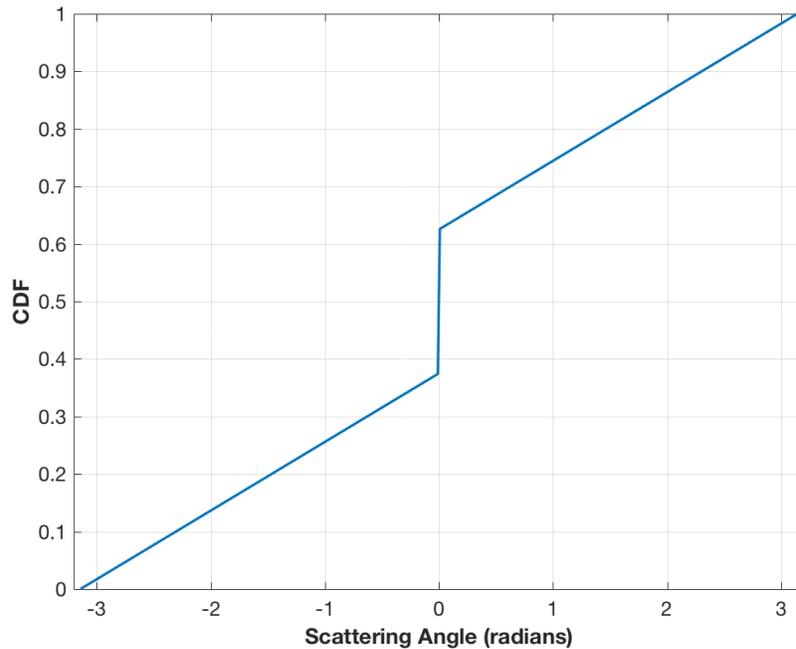
Figure 5.2: Scattering phase functions for medium snow grain distributions

89

Once the path length to the next scattering event has been calculated, the angle the photon leaves the current scattering interaction must be determined. This angle is governed by the scattering phase function for an individual snow grain. Measuring the exactly phase function for an individual snow grain is complex and depends on the shape of the snow grain (i.e., an ice sphere, or a complex fractal), the radius of the snow grain, snow grain orientation, and the wavelength of the radiation being scattered (Kokhanovshy and Zege, 2004). I follow an approach put forth in Duda et al., 2001, which uses the assumption that for scattering particles much larger than the wavelength of light being scattered, the scattering phase function can be approximated by a narrow forward scattering diffraction peak defined by a Gaussian function containing half of the scattering energy, with the other half of the scattering energy isotropically scattered. Since this study focuses 543 nm and 532 nm light, and our smallest snow grains are approximately 250 μm in diameter (three orders of magnitude larger than the photon wavelength), this method of defining the scattering phase function is reasonable for use in ELSA. Once the phase function is calculated, I compute its CDF, which I then normalize to a total sum of 1 (Figure 5.2). Once the scattering phase function CDF is normalized to one, I can again use a random number generator to select a photon exit angle to the next scattering event.

In addition to these scattering processes, absorption of photons by the snow also needs to be accounted for. To do this in a physically quantitative manner, I use the law of distribution to the nearest neighbor for randomly packed particles as described by Chandrasekhar (1943) and assume that the light absorbing impurities in the snow

are black carbon with a density of 2000 kg·m^{-3}. Given a concentration of absorbing

particles present in the snow, and an average absorbing particle radius (assuming a

spherical absorbing particle), an absorber number density is calculated. From here, I

use equation 5.4 (equation 671 from Chandrasekhar, 1943) to compute the probability

of distribution of the distance to the nearest absorbing particle:

$$w(r) = 4\pi r^2 n \cdot exp^{-\frac{4\pi r^3 n}{3}} \tag{5.4}$$

where n is the absorbing particle number density and r is the absorbing particle

radius. A sample probability distribution for distance to the nearest absorbing particle

calculated using equation 5.4 is shown in Figure 5.2. for an absorbing particle with a

radius of 2 µm, and a concentration of absorbing particles equal to 20 pptw. Taking
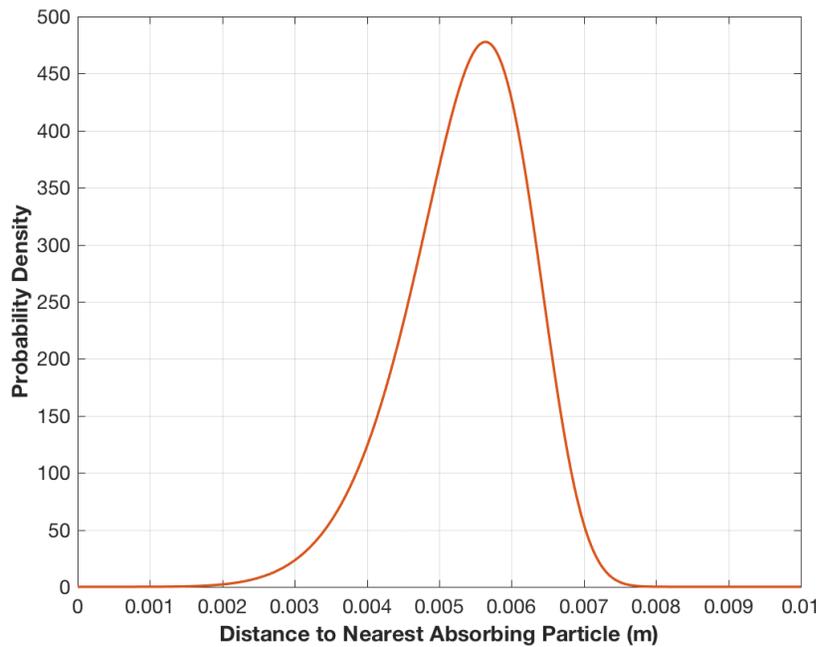
Figure 5.3: Probability distribution for distance to nearest absorbing particle with radius for particles with 2 µm radii, and concentration of 20 pptw.

91

this probability distribution and converting it to a CDF normalized to 1, I once again use a random number generator to select a distance to the nearest absorbing particle. If this distance is less than the photon path length, I assume the photon is intercepted by the absorbing particle on its way to the next scattering event and is completely absorbed. At this point the simulation of the photon is terminated and the model moves on to the next photon.

5.2.3 Photon detection

Once the simulation of a photon's scattering process had been terminated due to it violating at least one of the boundary conditions (e.g., photon's lateral position had intercepted a wall, photon's vertical position had intercepted the floor or exited the snow surface, or the photon was absorbed by a black carbon particle), I had to determine if the photon had reached and been recorded by a simulated detector. The solid-stat photo-diodes used to measure light intensity reaching the bottom of the test bed have an active detection area 3.6 mm by 3.6mm square. To simulate this in the model, I designated 3.6 mm stretches of the floor boundary condition as detector regions, with the same horizontal locations as in the physical test bed: one in the center, one 3.3 cm from the center, and one 6.6 cm from the center of the simulated test bed (see blue rectangles in Figure 5.1). If a photon was calculated to have intercepted the floor within the 3.6 mm stretch of any one of these detector regions, the detected photon count for that detector was increased by one.
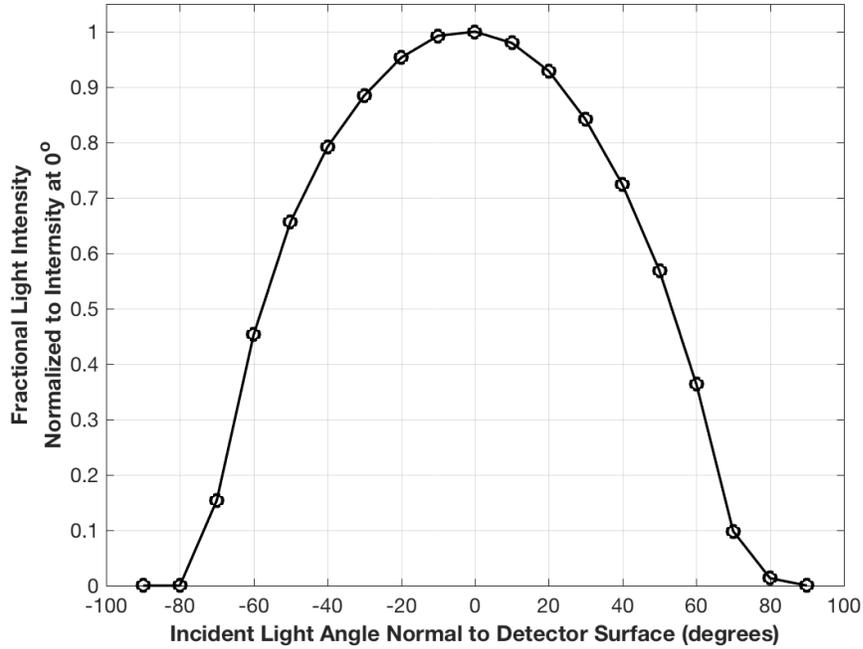
Figure 5.4: Laboratory measured angular dependence of measured light intensity by solid-state photo-diode detectors.

In detecting the photons in the model, we had to correct for the angular detection efficiency of the physical detectors. Calibration measurements of the detectors found there was an angular dependence of the light intensity measured by the detectors (Figure 5.4). Using this calibration data, I scaled the model detected photon by the detection efficiency of the physical detectors. As such, photons that intersected a detector region in the model with an incident angle greater than 80° normal to the detector were not recorded as being detected.

5.3: Results

5.3.1 Model sensitivity

To test ELSA's sensitivity to the parameters described above, I ran the model several times while changing only one parameter. The parameters run to test the model sensitivity were: the phase function ratio (shifting from mostly forward scattering to mostly isotropic scattering), the snow grain size, the concentration of black carbon
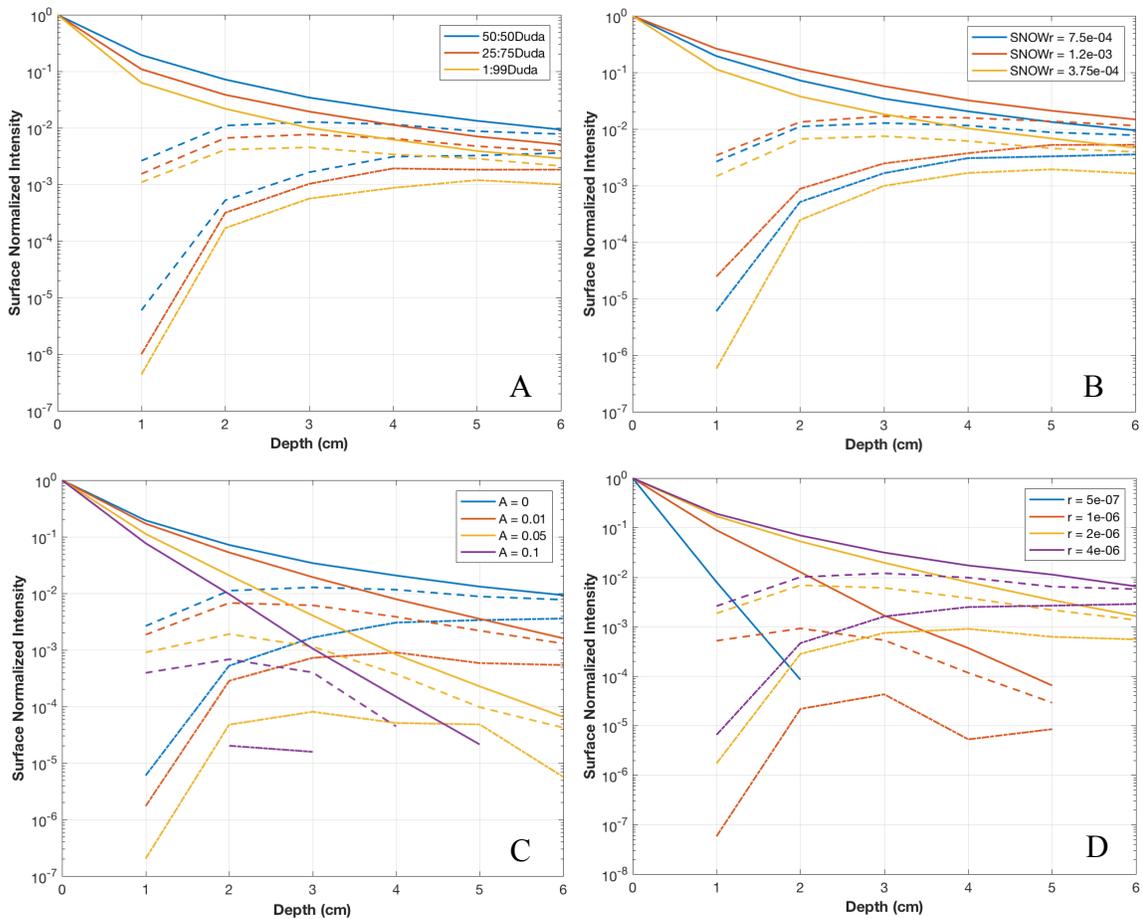
Figure 5.5: ELSA sensitivity to parameters. Solid lines indicate modeled intensities at the center detector, heavy dashed lines indicate intensities at the detector 3.3 cm from the center detector, and dot-dashed lines indicate intensities at the detector 6.6 cm from the center detector. (A) Percent of power in the scattering phase function represented by forward scattering (first ratio number), versus isotropic scattering (second ratio number). "Duda" refers to Duda et al*., 2001 which describes the method used to compute the phase function. (B) Snow grain diameter in meters. (C) Black carbon particle concentration in ppbw. (D) Black carbon particle radius in meters.*

particles in the snow, and the size of the black carbon particles. While the model

shows sensitivity to snow grain size and the ratio of forward to isotropic scattering, it

is highly sensitive to changes in both absorbing particle size and concentration.

5.3.2 Transmission simulations

To test if the model was realistically simulating the radiative transfer processes for

green photons traveling though snow, I compared the model simulated transmission

profiles to those for the medium snow grain distribution measured in chapter 2. In

addition to comparing the model to the transmission profile of the center detector (the

primary focus of chapter 2), I also relied on the transmission profiles of the side

detectors to help constrain the model parameters. For the medium snow grain

distribution, I found that instead of a scattering phase function split evenly in power

between forward and isotropic scattering, a ratio of 75% isotropic scattering and 25%

forward scattering produced most consistent with the laboratory measured

transmission profiles for all three detectors (Figure 5.6A). Additionally, the black

carbon particle concentration that best matched laboratory measured transmission
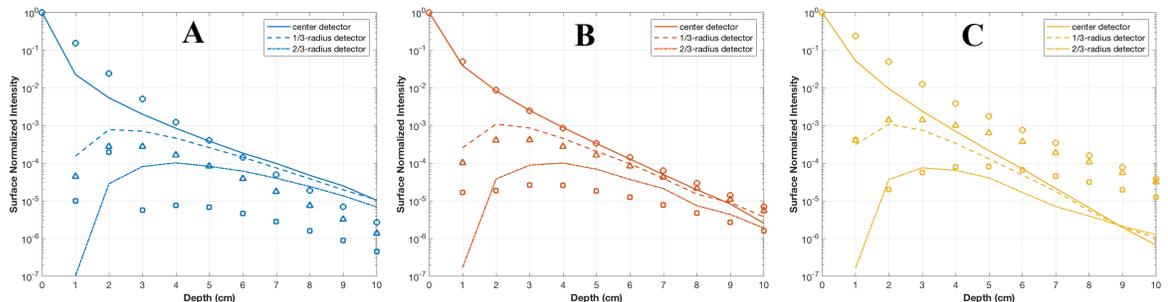
Figure 5.6: ELSA calculated transmission profiles (lines) compared to observed transmission profiles (circles, triangles, and squares) for (A) small, (B) medium, and (C) large snow grain distributions. Circles, triangles, and squares correspond to the center, middle, and outer detectors respectively.

profiles was 20 pptw, with a particle radius of 2 μm. This concentration is approximately 5 orders of magnitude smaller than the concentration measured in the actual snow samples.

I also compare the model simulated transmission profiles for the small and large snow grain distributions with those measured in the lab (Figures 5.6B and 5.6C). Both figures show that the model is indeed sensitive to grain size, however, the smaller grain size exhibits a more rapid decrease in transmitted intensity between zero and 4 cm depth, and a more gradual decrease in transmitted intensity at depth deeper than 4 cm compared to the laboratory measured transmission.

5.3.3 Reflected photons

In addition to comparing transmitted photons, I also compare simulated reflected photons to the reflectance measurements made with the ASD spectroradiometer in the laboratory described in chapter 1 (Figure 5.7). While the ELSA simulated reflectance is slightly higher than those measured by the ASD spectroradiometer, the separation in reflectance between the different snow grain size distributions are similar to those measured in the laboratory.
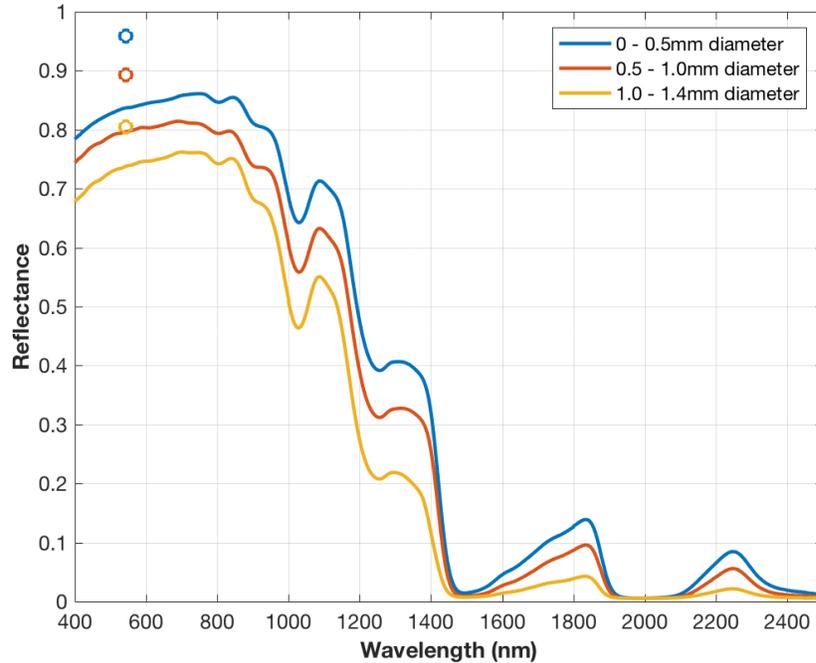
Figure 5.7: Laboratory ASD reflectance measurements (lines) with ELSA calculated reflectance (circles)

5.3.4 Backscattered photons

Using the model, I can directly analyze the aggregate path lengths of 532 nm wavelength photons (the wavelength used by MABEL) that backscatter out of the snow (Figure 5.8). These figures show a relationship between backscattered photon path length distributions and snow grain size, with backscattered photon path lengths inversely related to snow grain size distribution. ELSA simulations show the small snow grain size distribution resulting in backscattered photons with path lengths ranges up to three times longer than back scattered photons from the medium snow grain distribution, and backscattered photons from the medium snow grain distribution with path length ranges three time longer than those backscattered from
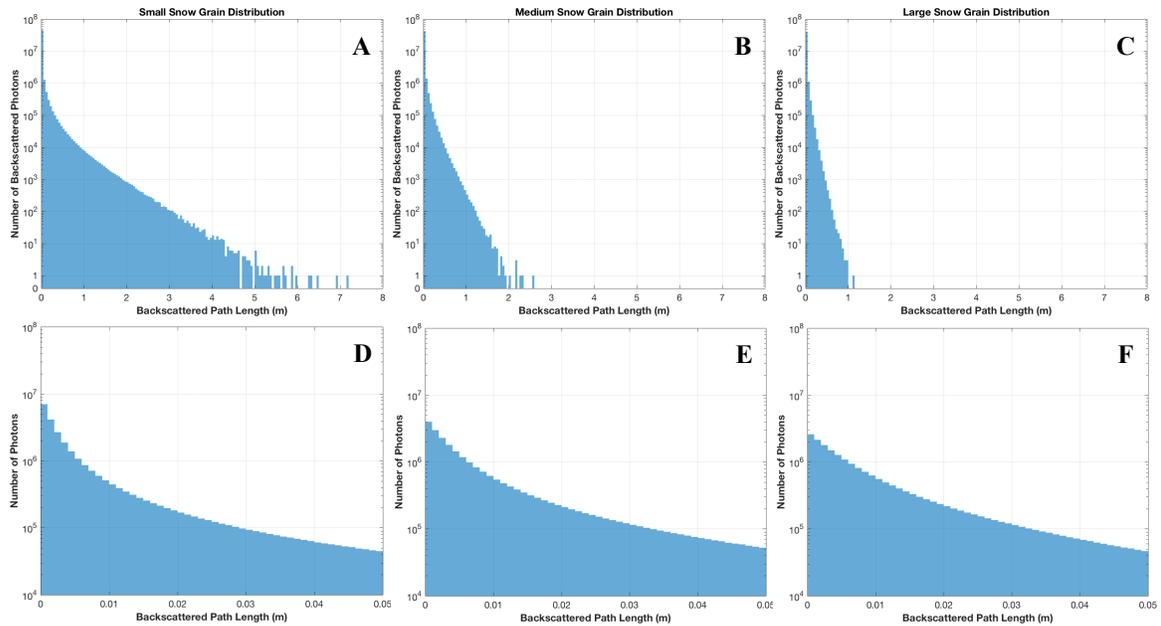
Figure 5.8: Model simulated photon path lengths for (A) small, (B) medium, and (C) large snow grain distributions, (D) Model path lengths for small snow grain distribution from 1 – 5 cm with surface reflected photons removed, (E) same as D, but for medium snow grain distribution, (F) same as D, but for large snow grain distribution.

the large snow grain distribution. It is important to note here, that the y-axis scale in these plots is logarithmic, while the x-axis is linear.

Using a model to simulate backscattered photon path also allows us to separate photons reflected off the snow surface (i.e., only one scattering event) from those that have volume-scattered within the snow. We can then calculate the fraction of backscattered photons that have volumed-scattered within a specified aggregated path length for each snow grain size distribution as is shown in Table 5.1.

ELSA not only allows us to quantify the path length distribution of backscattered photons, it also lets us compare photon path lengths with the maximum geometric depth reached by the same backscattered photons. Figure 5.9 shows the relationship

Table 5.1: Percent of modeled photons backscattered, reflected from the surface, or volume-scattered in the snow, but with path lengths less than 5 cm

	Small Snow Grains	Medium Snow Grains	Large Snow Grains
Backscattered	96 %	89 %	80 %
Surface reflected	39 %	42 %	46 %
Volume-scattered path length < 5 cm	55 %	53 %	50 %

between these two quantities for each simulated backscattered photon. Here, we see that rather than having a two-to-one relationship (which would indicate photons traveling straight down and straight back up and out of the snow), most photons accumulate path lengths approximately an order of magnitude larger than the maximum depth they reach. In other words, most of the backscattered photons are scattering more times closer to the surface of the snow, rather than scattering fewer times, but traveling greater distances into the snow.
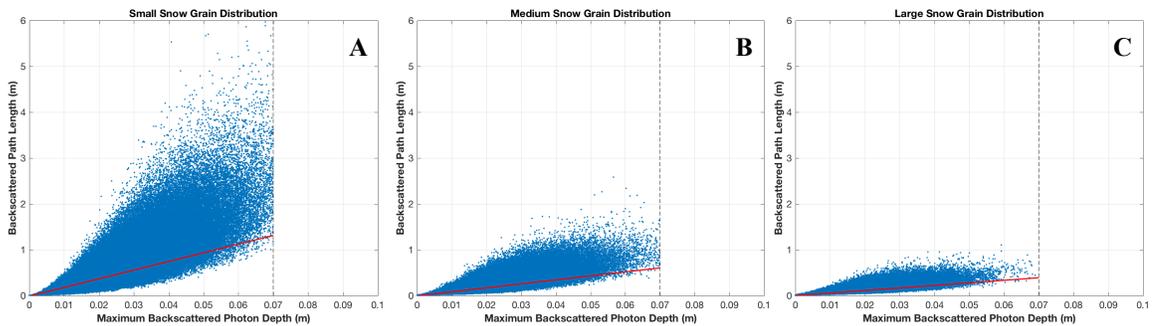
Figure 5.9:   ELSA computed photon path lengths vs. maximum physical depth reached by the photon for (A) small, (B) medium, and (C) large snow grain size distributions. Red line in all plots is a standard linear regression.

5.4: Discussion

5.4.1 Transmission

The ELSA simulations of 543 nm light transmission through snow compare well to the laboratory measured transmission profiles through snow. However, the most glaring discrepancy between the model simulated transmission profiles and those measured in the laboratory is the difference in absorbing particle concentrations. Using the filtration method discussed in chapter 2, I measured the equivalent black carbon concentration in our snow to be 2.3, 1.8, and 1 ppmw for the small, medium and large snow grain distributions respectively. The model simulations were only able to produce results comparable to the transmission measurements made in chapter 2 with a black carbon concentration of 20 pptw; 5 orders of magnitude smaller than what was measured in the snow. There are several plausible explanations for why the model is not able to reproduce the transmission simulations with the impurity loading measured in the snow. One is that the model transmission is sensitive to the absorbing particle size, with large absorber particle sizes producing less absorption than small absorbing particles. This is evident in Figure 5.5D, which shows the model's sensitivity to absorbing particle size. While I was able to measure the concentration of equivalent black carbon in the snow used for the transmission measurements, I was not able to measure the size of the impurity particles. Literature suggests that graphitic or back carbon/soot particles in snow have radii less than 1 μm (Warren and Wiscombe, 1980; Flanner et *al*., 2012). Since I was unable to measure the radius of absorbing particles in my snow, this remains a somewhat tunable parameter in the

model. Additionally, my snow impurity measurements were not able to specify the type of absorbing particle in the snow, only the equivalent amount of black carbon needed to produce the same amount of reduction in transmission. As a result, using a larger absorbing particle radius in the model may be reasonable, given that the absorbing particles in the snow I used may not actually be black carbon.

Similarly, the model represents absorbing particles are perfectly absorbing (i.e., albedo of zero). If the actual absorbing particles in the snow used for transmission measurements is not actually black carbon, or perfectly absorbing, then the model may be over estimating the absorption by absorbing particles.

The model may also not properly represent the likelihood that a photon is intercepted by an absorbing particle on its way to the next scattering event. The current method calculates a photon's path length from the current scattering event to the next scattering event. A distance to an absorbing particle is independently calculated. If the distance to an absorbing particle is less than or equal to the photon's path length to the next scattering event, the photon is absorbed. However, just because an absorbing particle is less than or equal to the path length the photon is traveling to the next scattering event doesn't necessarily mean that the absorbing particle is in the photon's path. That is to say, the absorbing particle could be located at an angle to the photon's path. The fact that the model does not properly account for the absorbing particle's location relative to path being taken by the photon would result in a higher rate of

photon absorption than expected. This may also explain the model's high sensitivity to absorber concentration and size.

5.4.2 Reflected photons

The photons reflected by the snow show a similar dependence on grain size as observed by the ASD in the laboratory. However, the model produces higher reflectance than the ASD measurements. This is likely due to the model counting all reflected photons and not accounting for the viewing angle of the ASD. Given that the model produces reflectance that is higher than expected, restricting the modeled photons that would be considered reflected to those within a field of view comparable to the ASD should reduce the model reflectance while maintaining the separation in reflectance values associated with snow grain size.

5.4.3 Backscattered photons

The photons backscattered in the model provide some interesting insight into the scattering processes of photons within the snow. Having validated the model using 543 nm light, I change the wavelength of modeled light to that of MABEL, 532 nm. While the path length of photons across all grain sizes simulated range from 1 m to 7 m, approximately 95% all the photons come have path lengths less than 5 cm. Furthermore, approximately 40% of these photons are reflected directly off the snow surface (i.e., they have scattered only once and have an aggregated path length of zero). This suggests that while it is physically possible for photons to accrue large path lengths, it is highly unlikely that these photons will be received by the altimeter

102

system and that their aggregated path length will likely be less than 5 cm. Additionally, while these photons may have path lengths of a few centimeters to decimeters, the maximum physical depth they reach is limited to the first few centimeters of snow. This suggests that for altimeters such as ATLAS, which is only expected to receive approximately 10 surface photons per shot over snow surfaces, there is a very low statistical probability that they will measure photons with path lengths exceeding a few centimeters, and that those photons will have come from the near surface of the snow.

5.5: Conclusions and future work

A model is developed here to simulate and track photons propagating though snow. It is able to successfully reproduce transmission intensities for 543 nm light through snow measured in a laboratory setting, including a dependence on snow grain size. The model is also able to produce a reasonable estimate of reflectance for varying snow grain sizes compared with laboratory measured snow reflectance. While the model does a good job at reproducing measured transmission and reflectance values, there is still room for improvement. The model currently underestimated the amount of light absorbing impurities in the snow. This is likely due to an improper parameterization of absorbing particles in the snow, rather than a problem with the physical properties represented in the model itself. Additionally, while the concentration of light absorbing particles is known from measurements made using

filtration, there is also some uncertainty associated with the physical properties of the absorbing particles such as their size.

The model's ability to reproduce these measured values give confidence in its ability to accurately simulate individual scattered photons paths through the snow. The model suggests that while it is statistically possible for photons to accrue path lengths of several meters, most backscattered photons from the snow have relatively small path lengths, less than 10 cm. Additionally, most backscattered photons do not travel significant geometric distances into the snow, but are generally confined to the first few centimeters near the surface.

Chapter 6: Conclusions

The work presented in this dissertation provides a detailed analysis of the physical properties of snow pertinent to the microphysical processes governing the scattering of visible light in snow. The experiments and methods described were designed to provide results directly applicable to the quantities and processes of most interest and concern for laser altimetry applications, particularly with regard to green light penetration in snow. Our results overall show that green light does penetrate into snow, but that volume-scattered photons do not have a significant effect on photons received by laser altimeters.

6.1 Transmission

The methods used to measure transmission of green light though snow in this study are significantly different from previous studies of transmission in the field, which relied on broadband diffuse light sources that illuminated the entire snow surface. Additionally, we provide a unique approach of physically separating the snow into different grain size distributions, allowing us to directly measure the effect of snow grain size on transmission. Laboratory transmission measurements of collimated, narrow-beam green light through snow reveal a rapid decrease in the amount of light transmitted through snow with several different grain sizes. Across all snow grain size distributions, transmission of 543 nm light decreases between 2 and 4 orders of

magnitude in the first 4 cm of snow. While the dependence of transmission on snow grain size is ambiguous in shallow snow, transmission in snow greater than 7 cm is proportional to the snow grain size, with larger snow grains transmitting more light than smaller snow grains.

To fully characterize the physical properties of the snow governing transmission, I made measurements of optical impurity loading in the snow to quantify the absorptive properties of the snow, as well as transmission measurements at locations out of the direct path of the illuminating beam to assess the scattering phase function of the snow. The snow used for transmission measurements contained an equivalent black carbon concentration approximately 3 orders of magnitude higher than expected for snow from Summit, Greenland. This likely resulted in our measurements underestimating the transmission for snow in locations like the interior of ice sheets such as Summit, Greenland, or South Pole, Antarctica. However, they may be informative as to the expected impact of impurities on transmission for areas like the margins of the Greenland ice sheet and mountainous glaciers where impurity loading is higher than the relatively pure interior regions.

While I was unable to measure any detectable influence, the walls and floor of the experimental test bed may have reduced the total transmission by absorbing light that would otherwise have been scattered farther down into the snow. Were this type of measurement to be repeated, I would recommend use of a larger containment structure to ensure there is no effect of the walls and floor on the measured

106

transmission. In addition, I would recommend using snow with varying degrees of impurity loading to constrain the absorbing properties of the snow.

In addition to quantitatively measuring the optical impurity concentration in the snow, we also quantitatively measured the impurity loading via hyperspectral reflectance measurements with an ASD spectroradiometer. While these measurements were not as quantitative as the filter measurements of snow impurities, it did result in a method for measuring snow reflectance using an artificial illumination source in a controlled laboratory environment. While not entirely novel, the vast majority of snow hyperspectral measurements are made relying solar illumination. Our laboratory measurements point to a way forward for making successful hyperspectral measurements for snow surfaces in a controlled environment in the future.

6.2 Fitting an exponentially-modified Gaussian function to MABEL photon returns

The advent of single photon counting detectors for laser altimetry offers significantly more information and detail than full-waveform laser altimeter systems. Developing new methods for characterization of these individual photons remains an ongoing area of research. Histograms have traditionally been used to aggregate photons from several laser shots and estimate both the shape of the laser pulse, as well as surface returns. In chapter 3, I show that using histograms to characterize the laser pulse shape reduces the resolution and information present in the individual photon returns,

and that they contain subjective uncertainty associated with the width chosen for the histogram bins. I present a robust method for estimating the laser pulse shape by fitting the individual photon returns to an exponentially-modified Gaussian distribution, which taking advantage of the single photon detection capability of photon altimeters such as MABEL and ATLAS. This method of fitting an exponentially-modified Gaussian to photon returns from MABEL produces a RMSE more than three times smaller than that using a standard Gaussian fit.

In the process of demonstrating the utilitarian nature of the exponentially-modified Gaussian, I also discuss the influence of sample size on the precision of estimated distribution parameters such as the mean, standard deviation, and the exponentially-modified Gaussian parameters mu, sigma, and tau. Analysis indicates that using groups of photons consisting of at least 250 photons is required to calculate distribution parameters within 3 cm of their true values, with a probability equal to one standard deviation. To ensure a higher probability of the calculated parameters being within 3 cm of their true values, larger sample sizes of photons must be used.

6.3 *Laboratory measurements of green light penetration in snow using MABEL*

To assess the impact of volume-scattered photons on MABEL measured photon returns, I made a series of measurements in a controlled laboratory environment using MABEL to range to both a snow target, which includes volume scattering, and a

Spectralon standard reflectance panel, which does not volume scatter visible wavelength photons. These tests reveal that volume scattering in snow causes the peak of the photon return distribution to shift farther away from the altimeter between 5 and 11 cm, depending on the snow grain size. The results show that the small snow grain distribution produced the smallest shift in the return photon distribution peak, while the largest snow grain distribution produced the greatest shift. The two medium snow grain distributions used for this test produced similar shifts in their return photon distribution peaks.

During the course of measuring the effect of volume scattering in snow on the photon return distributions, I discovered that MABEL's pulse shape has some drift driven by internal processes rather than physical changes in range to the target surface. This complicates the measurements to estimate the effect of volume scattering in the snow as the pulse shape stability measurements suggest there is some inherent uncertainty in the range MABEL measures. The effect of these variations may be evident in the nearly identical photon return distributions from the medium and large snow grain size distributions.

Several steps could be made to improve these measurements. It may be possible to make adjustments in photon return ranges based on the variability in parameters like the mean and exponentially-modified mu parameter while photons are recorded. I also collected coincident range measurements using MABEL's 1064 nm wavelength channel, which is not expected to volume scatter within snow as the 1064 nm photons

are quickly absorbed by snow. While this could produce an interesting comparison between two wavelengths with different volume scattering over the same target surface, any two channels within MABEL have different paths to their respective detectors. This means that the photon ranges for two separate channels will likely not be the same, making comparing a small shift in range due to volume scattering difficult.

6.4 Modeling photons scattering in snow

While direct measurements of volume scattering in snow using MABEL are useful, they don't fully answer the question of how many photons are being volume-scattered, the path lengths of the volume-scattered photons, or the physical depth traveled by volume-scattered photons. To answer these questions, I developed a Monte Carlo photon scattering model to simulate individual photons propagating through snow. To validate that the model produced realistic simulations, I compared model runs against transmission profile measurements, with attention paid to the side detector transmission measurements to constrain the scattering phase function of the model.

Over all the model reasonably simulated the transmission of green light photons through snow, with sensitivity to snow grain size, and absorbing particle concentrations. It underestimates the concentration of absorbing particles needed to reproduce the laboratory measured transmission profiles, but it is suspected that this

is due to an over estimation of the probability for a photon intercepting an absorbing particle on its way to a scattering event in the absorbing particle parameterization.

Having seen that the model was producing reasonable simulations for transmission of 543 nm photons through snow, I turned my focus to photons backscattered out of the snow at 532 nm; the wavelength used by MABEL and ATLAS. Analysis of backscattered photons reveals that photons backscattered from snow with smaller grain sizes have longer path lengths than photons backscattered from large snow grains. While some photons backscattered from small snow grains have accrued path lengths up to 7 m, approximately 95% of these backscattered photons have path lengths less than 5 cm and include photons reflected directly off the snow surface. Using the model, I was also able to track the maximum physical depth reached by backscattered photons. While photons reaching a wide variety of physical depths were back scattered out of the snow, again, an overwhelming majority returned from the first centimeter of snow across all snow grain sizes. This shows that while it is statistically possible for photons to accrue large path lengths and travel several centimeters into the snow, it is highly unlikely that laser altimeters, including ATLAS which is expected to receive approximately 10 photons per shot from snow surfaces, will measure photons that have accrued path lengths that will significantly alter elevation estimates. This is particularly true given that the measurements and analysis performed in this study assume the most ideal situation for volume-scattered photons to be backscattered, i.e., a flat surface, while field measurements will include surface

features such as roughness and slope, which will mask the second order effect of the volume-scattered photons.

Appendix A: Measurement Uncertainties

We found that repeated measurements of transmission through snow with the same grain size distribution gave slightly different profiles. As a result, we measured transmission profiles at least three times for each snow grain size to account for variability in the way snow was added to the test bed. To calculate the light intensity detected at a given depth, we averaged all of the data logger recorded detector voltages:

$$\bar{x} = \frac{\sum x_i}{N} \quad (A1)$$

and accept the uncertainty for this value as the standard deviation of the mean defined as:

$$\sigma_{\bar{x}} = \frac{\sigma_{x_i}}{\sqrt{N}} \quad (A2)$$

where σ_{x_i} is the standard deviation of all the data logger recorded detector voltages and N is the number of recorded detector voltages. These calculations were made at each depth for a specific transmission profile. The standard method for combining several separate transmission profiles is to combine the mean intensity measurements for a given depth by weighting each mean with its associated uncertainty (the standard deviation of the mean, $\sigma_{\bar{x}}$), such that mean intensity measurements with smaller uncertainty are weighted more heavily. However, in nearly all cases, intensity

measurements from one profile are inconsistent with intensity measurements for other profiles at a given depth because the uncertainties associated with the mean intensity measurements are so small that they don't overlap with mean intensity measurements from other profiles (Fig. 2). According to Taylor (1997), "If the discrepancy $|\overline{X}_A - \overline{X}_B|$ between the two measurements is much greater than both uncertainties σ_A and σ_B … we should examine both measurements to see whether either (or both) was subject to unnoticed systematic errors" (Taylor pg. 173). This suggests that there is a systematic error associated with how the snow was sieved into the test bed. We suspect that this systematic error is due to random, uncontrollable differences in the snow that occur each time snow was sieved into the test bed.

We argue that the small uncertainties (Equation A2) associated with each intensity measurement represent the instrument uncertainty. To account for the uncertainty associated with sieving snow into the test bed, we developed a method for combining separate profiles measurements with weights and uncertainties based on the discrepancy between separate profile measurements, and which discounts outlier profiles that likely contain snow that has undergone significant metamorphosis. For each intensity measurement for a given grain size fraction, we computed the mean discrepancy, d_i, relative to the all other profile intensity measurements at the given depth:

$$\overline{d}_\iota = \frac{\sum \sqrt{(p_i - p_n)^2}}{N - 1} \qquad (A3)$$

where p_i is an intensity measurement from one of n profiles for n ≠ i. N equals the total number of profiles, including p_i. This mean discrepancy is used to compute the uncertainty of the profile by first normalizing the mean discrepancy to a fraction (f_i) of the total discrepancies:

$$f_i = \frac{\overline{d_i}}{\sum \overline{d_i}} \qquad (A4)$$

The fractional discrepancy is then transformed into a weight (w_i) for each intensity measurement:

$$w_i = \frac{\frac{1}{f_i}}{\sum \frac{1}{f_i}} \quad (A5)$$

This allows us to combine the intensity measurements from all the profiles into a weighted mean:

$$\mathbb{X} = \frac{\sum \bar{x}_i w_i}{\sum w_i} \quad (A6)$$

The uncertainties for the combined measurements ($\mathbb{X}$) are then computed from these weights:

$$\sigma_{\mathbb{X}} = \frac{1}{\sqrt{\sum w_i}} \quad (A7)$$

We use this value ($\sigma_{\bar{X}}$) as the uncertainty for the mean profiles ($\bar{X}$), which are denoted by the colored shaded areas and thick lines in Fig. 5 respectively. The absolute values for uncertainties depend on the snow grain size and snow depth. Generally, the uncertainties increase with increasing snow depth and larger snow grain sizes.

Bibliography

Awadallah, M., Ghannam, S., Abbott, L., & Ghanem, A. (2014, July). A two-stage
algorithm for extraction of ground and top of canopy in photon-counting
profiling-LiDAR data in preparation for the ICESat-2 mission. In *Geoscience and
Remote Sensing Symposium (IGARSS), 2014 IEEE International* (pp. 1353-1356).
IEEE.

Aoki, T., Aoki, T., Fukabori, M., Hachikubo, A., Tachibana, Y., & Nishio, F. (2000).
Effects of snow physical parameters on spectral albedo and bidirectional
reflectance of snow surface. *Journal of Geophysical Research:
Atmospheres*, *105*(D8), 10219-10236.

Blair, J. B., Rabine, D. L., & Hofton, M. A. (1999). The Laser Vegetation Imaging
Sensor: a medium-altitude, digitisation-only, airborne laser altimeter for mapping
vegetation and topography. *ISPRS Journal of Photogrammetry and Remote
Sensing*, *54*(2), 115-122.

Brunt, K. M., Neumann, T. A., Walsh, K. M., & Markus, T. (2014). Determination of
local slope on the Greenland Ice Sheet using a multibeam photon-counting Lidar
in preparation for the ICESat-2 Mission. *IEEE Geoscience and Remote Sensing
Letters*, *11*(5), 935-939.

Brunt, K. M., Neumann, T. A., Amundson, J. M., Kavanaugh, J. L., Moussavi, M. S., Walsh, K. M., & Cook, W. B. (2016). MABEL photon-counting laser altimetry data in Alaska for ICESat-2 simulations and development. *The Cryosphere*, *10*(4), 1707.

Bøggild, C. E., Brandt, R. E., Brown, K. J., & Warren, S. G. (2010). The ablation zone in northeast Greenland: ice types, albedos and impurities. *Journal of Glaciology*, *56*(195), 101-113.

Bohren, C. F., & Barkstrom, B. R. (1974). Theory of the optical properties of snow. *Journal of Geophysical Research*, *79*(30), 4527-4535.

Casey, K. A., Kääb, A., & Benn, D. I. (2012). Geochemical characterization of supraglacial debris via in situ and optical remote sensing methods: a case study in Khumbu Himalaya, Nepal. *The Cryosphere*, *6*(1), 85-100.

Casey, K. A., Kaspari, S. D., Skiles, S. M., Kreutz, K., & Handley, M. J. (2017). The spectral and chemical measurement of pollutants on snow near South Pole, Antarctica. *Journal of Geophysical Research: Atmospheres*.

Chýlek, P., Johnson, B., Damiano, P. A., Taylor, K. C., & Clement, P. (1995). Biomass burning record and black carbon in the GISP2 ice core. *Geophysical research letters*, *22*(2), 89-92.

Colbeck, S. C. (1983). Theory of metamorphism of dry snow. *Journal of Geophysical Research: Oceans*, *88*(C9), 5475-5482.

Colbeck, S. C. (1982). An overview of seasonal snow metamorphism. *Reviews of Geophysics*, *20*(1), 45-61.

Comiso, J. C., & Nishio, F. (2008). Trends in the sea ice cover using enhanced and compatible AMSR-E, SSM/I, and SMMR data. *Journal of Geophysical Research: Oceans*, *113*(C2).

Cook, B. D., Nelson, R. F., Middleton, E. M., Morton, D. C., McCorkel, J. T., Masek, J. G., Ranson, K.J., Ly, V., & Montesano, P. M. (2013). NASA Goddard's LiDAR, hyperspectral and thermal (G-LiHT) airborne imager. *Remote Sensing*, *5*(8), 4045-4066.

Cook, J. M., Hodson, A. J., Taggart, A. J., Mernild, S. H., & Tranter, M. (2017). A predictive model for the spectral "bioalbedo" of snow. *Journal of Geophysical Research: Earth Surface*, *122*(1), 434-454.

Dabney, P., Harding, D., Abshire, J., Huss, T., Jodor, G., Machan, R., Marzouk, J., Rush, K., Seas, A., Shuman, C., Sun, X., Valett, S., Vasilyev, A., Yu, A. and Zheng, Y. (2010, July). The slope imaging multi-polarization photon-counting

lidar: Development and performance results. In *Geoscience and Remote Sensing Symposium (IGARSS), 2010 IEEE international* (pp. 653-656). IEEE.

Degnan, J. J. (2002). Photon-counting multikilohertz microlaser altimeters for airborne and spaceborne topographic measurements. *Journal of Geodynamics*, *34*(3), 503-549.

Doherty, S. J., Warren, S. G., Grenfell, T. C., Clarke, A. D., & Brandt, R. E. (2010). Light-absorbing impurities in Arctic snow. *Atmospheric Chemistry and Physics*, *10*(23), 11647-11680.

Duda, D.P., Spinhirne, J.D., & Eloranta E.W. (2001). Atmospheric multiple scttering effects on GLAS altimetry – Part I: Calculations of single pulse bias. *IEEE Transactions on Geoscience and Remote Sensing*, *39*(1), 92-101.

Ewert, H., Groh, A., & Dietrich, R. (2012). Volume and mass changes of the Greenland ice sheet inferred from ICESat and GRACE. *Journal of Geodynamics*, *59*, 111-123.

Farrell, S. L., Brunt, K. M., Ruth, J. M., Kuhn, J. M., Connor, L. N., & Walsh, K. M. (2015). Sea-ice freeboard retrieval using digital photon-counting laser altimetry. *Annals of Glaciology*, *56*(69), 167-174.

Gallet, J. C., Domine, F., Zender, C. S., & Picard, G. (2009). Measurement of the

    specific surface area of snow using infrared reflectance in an integrating sphere at

    1310 and 1550 nm. *The Cryosphere*, *3*(2).

Gautam, R., Hsu, N. C., Lau, W. K. M., & Yasunari, T. J. (2013). Satellite

    observations of desert dust-induced Himalayan snow darkening. *Geophysical*

    Research Letters, *40*(5), 988-993.

Gay, M., Fily, M., Genthon, C., Frezzotti, M., Oerter, H., & Winther, J. G. (2002).

    Snow grain-size measurements in Antarctica. *Journal of Glaciology*, *48*(163),

    527-535.

Glenn, N. F., Neuenschwander, A., Vierling, L. A., Spaete, L., Li, A., Shinneman, D.

    J., Pilloid, D.S., Arkle, R.S. & McIlroy, S. K. (2016). Landsat 8 and ICESat-2:

    Performance and potential synergies for quantifying dryland ecosystem vegetation

    cover and biomass. *Remote Sensing of Environment*, *185*, 233-242.

Grenfell, T. C., & Maykut, G. A. (1977). The optical properties of ice and snow in the

    Arctic Basin. *Journal of Glaciology*, *18*(80), 445-463.

Grenfell, T. C., & Warren, S. G. (1999). Representation of a nonspherical ice particle

    by a collection of independent spheres for scattering and absorption of

radiation. *Journal of Geophysical Research: Atmospheres*, *104*(D24), 31697-
31709.

Grenfell, T. C., Warren, S. G., & Mullen, P. C. (1994). Reflection of solar radiation
by the Antarctic snow surface at ultraviolet, visible, and near-infrared
wavelengths. *Journal of Geophysical Research: Atmospheres*, *99*(D9), 18669-
18684.

Gwenzi, D., & Lefsky, M. A. (2014). Prospects of photon counting lidar for savanna
ecosystem structural studies. *The International Archives of Photogrammetry,
Remote Sensing and Spatial Information Sciences*, *40*(1), 141.

Hadley, O. L., & Kirchstetter, T. W. (2012). Black-carbon reduction of snow
albedo. *Nature Climate Change*, *2*(6), 437-440.

Herzfeld, U. C., McDonald, B. W., Wallin, B. F., Neumann, T. A., Markus, T.,
Brenner, A., & Field, C. (2014). Algorithm for detection of ground and canopy
cover in micropulse photon-counting lidar altimeter data in preparation for the
ICESat-2 mission. *IEEE Transactions on Geoscience and Remote Sensing*, *52*(4),
2109-2125.

Hodson, A. J., Nowak, A., Cook, J., Sabacka, M., Wharfe, E. S., Pearce, D. A.,
Convey, P. & Vieira, G. (2017). Microbes influence the biogeochemical and

optical properties of maritime Antarctic snow. *Journal of Geophysical Research: Biogeosciences*.

Holland, P. R., Corr, H. F., Pritchard, H. D., Vaughan, D. G., Arthern, R. J., Jenkins, A., & Tedesco, M. (2011). The air content of Larsen ice shelf. *Geophysical Research Letters*, *38*(10).

Jasinski, M. F., Stoll, J. D., Cook, W. B., Ondrusek, M., Stengel, E., & Brunt, K. (2016). Inland and Near-Shore Water Profiles Derived from the High-Altitude Multiple Altimeter Beam Experimental Lidar (MABEL). *Journal of Coastal Research*, *76*(sp1), 44-55.

Johnson, J. S., Bentley, M. J., & Gohl, K. (2008). First exposure ages from the Amundsen Sea embayment, West Antarctica: The late quaternary context for recent thinning of Pine Island, Smith, and Pope Glaciers. *Geology*, *36*(3), 223-226.

Joughin, I., Smith, B. E., & Holland, D. M. (2010a). Sensitivity of 21st century sea level to ocean-induced thinning of Pine Island Glacier, Antarctica. *Geophysical Research Letters*, *37*(20).

Joughin, I., Smith, B. E., Howat, I. M., Scambos, T., & Moon, T. (2010b). Greenland

  flow variability from ice-sheet-wide velocity mapping. *Journal of*

  Glaciology, *56*(197), 415-430.

Kaspari, S., Painter, T. H., Gysel, M., Skiles, S. M., & Schwikowski, M. (2014).

  Seasonal and elevational variations of black carbon and dust in snow and ice in

  the Solu-Khumbu, Nepal and estimated radiative forcings. *Atmospheric chemistry*

  and physics, *14*(15), 8089-8103.

Khan, A. L., Dierssen, H., Schwarz, J. P., Schmitt, C., Chlus, A., Hermanson, M.,

  Painter, T., & McKnight, D. M. (2017). Impacts of coal dust from an active mine

  on the spectral reflectance of Arctic surface snow in Svalbard, Norway. *Journal of*

  Geophysical Research: Atmospheres, *122*(3), 1767-1778.

Kokhanovsky, A. (2013). Spectral reflectance of solar light from dirty snow: a simple

  theoretical model and its validation. *The Cryosphere*, *7*(4), 1325.

Kokhanovsky, A. A., & Zege, E. P. (2004). Scattering optics of snow. *Applied*

  Optics, *43*(7), 1589-1602.

Krabill, W. B., Abdalati, W., Frederick, E. B., Manizade, S. S., Martin, C. F.,

  Sonntag, J. G., Swift., R.N., Thomas, R.H., & Yungel, J. G. (2002). Aircraft laser

altimetry measurement of elevation changes of the Greenland ice sheet:

Technique and accuracy assessment. *Journal of Geodynamics*, *34*(3), 357-376.

Krichel, N. J., McCarthy, A., & Buller, G. S. (2010). Resolving range ambiguity in a

photon counting depth imager operating at kilometer distances. *Optics*

express, *18*(9), 9192-9206.

Krystek, M., & Anton, M. (2007). A weighted total least-squares algorithm for fitting

a straight line. *Measurement Science and Technology*, *18*(11), 3438.

Kwok, R. (2009). Outflow of Arctic Ocean sea ice into the Greenland and Barents

Seas: 1979–2007. *Journal of Climate*, *22*(9), 2438-2457.

Kwok, R., Markus, T., Morison, J., Palm, S. P., Neumann, T. A., Brunt, K. M., Cook,

W.B., Hancock, W., & Cunningham, G. F. (2014). Profiling sea ice with a

multiple altimeter beam experimental Lidar (MABEL). *Journal of Atmospheric*

and Oceanic Technology, *31*(5), 1151-1168.

Lacouture, Y., & Cousineau, D. (2008). How to use MATLAB to fit the ex-Gaussian

and other probability functions to a distribution of response times. *Tutorials in*

Quantitative Methods for Psychology, *4*(1), 35-45.

Lyapustin, A., Tedesco, M., Wang, Y., Aoki, T., Hori, M., & Kokhanovsky, A. (2009). Retrieval of snow grain size over Greenland from MODIS. *Remote Sensing of Environment*, *113*(9), 1976-1987.

Markus, T., Stroeve, J. C., & Miller, J. (2009). Recent changes in Arctic sea ice melt onset, freezeup, and melt season length. *Journal of Geophysical Research: Oceans*, *114*(C12).

Markus, T., Neumann, T., Martino, A., Abdalati, W., Brunt, K., Csatho, B., Farrell, S., Fricker, H., Gardner, A., Harding, D., Jaskinski, M., Kwok, R., Magruder, L., Lubin, D., Luthcke, S., Morison, J., Nelson, R., Neuenschwander, A., Palm, S., Popescu, S., Shum, C.K., Smith, B., Yang, Y., & Zwally, J. (2017). The Ice, Cloud, and land Elevation Satellite-2 (ICESat-2): Science requirements, concept, and implementation. *Remote Sensing of Environment*, *190*, 260-273.

Martonchik, J. V., Bruegge, C. J., & Strahler, A. H. (2000). A review of reflectance nomenclature used in remote sensing. *Remote Sensing Reviews*, *19*(1-4), 9-20.

McGill, M., Markus, T., Scott, V. S., & Neumann, T. (2013). The multiple altimeter beam experimental Lidar (MABEL): An airborne simulator for the ICESat-2 mission. *Journal of Atmospheric and Oceanic Technology*, *30*(2), 345-352.

NASA Goddard Space Flight Center: MABEL lidar data, MABEL ICESat-2
simulation data, Version 10, Greenbelt, Maryland USA,
https://icesat.gsfc.nasa.gov/icesat2/data/mabel/mabel_docs.php, 2014

United States. National Bureau of Standards, & Nicodemus, F. E.
(1977). *Geometrical considerations and nomenclature for reflectance* (Vol. 160).
US Department of Commerce, National Bureau of Standards.

Nolin, A. W., & Dozier, J. (1993). Estimating snow grain size using AVIRIS
data. *Remote sensing of environment*, *44*(2-3), 231-238.

Nolin, A. W., & Dozier, J. (2000). A hyperspectral method for remotely sensing the
grain size of snow. *Remote sensing of Environment*, *74*(2), 207-216.

Painter, T. H., Duval, B., Thomas, W. H., Mendez, M., Heintzelman, S., & Dozier, J.
(2001). Detection and quantification of snow algae with an airborne imaging
spectrometer. *Applied and Environmental Microbiology*, *67*(11), 5267-5272.

Perovich, D. K. (2007). Light reflection and transmission by a temperate snow
cover. *Journal of Glaciology*, *53*(181), 201-210.

Pope, A., & Rees, G. (2014). Using in situ spectra to explore Landsat classification of glacier surfaces. *International Journal of Applied Earth Observation and Geoinformation*, *27*, 42-52.

Pritchard, H. D., & Vaughan, D. G. (2007). Widespread acceleration of tidewater glaciers on the Antarctic Peninsula. *Journal of Geophysical Research: Earth Surface*, *112*(F3).

Pritchard, H. D., Luthcke, S. B., & Fleming, A. H. (2010). Understanding ice-sheet mass balance: progress in satellite altimetry and gravimetry. *Journal of Glaciology*, *56*(200), 1151-1161.

Qunzhu, Z., Meisheng, C., Xuezhi, F., Fengxian, L., Xianzhang, C., & Wenkun, S. (1983) A study of spectral reflection characteristics for snow, ice and water in the north of China. *Hydrological Application of Remote Sensing and Remote Data Transmission*, 145, 451-462.

Rignot, E. (2008). Changes in West Antarctic ice stream dynamics observed with ALOS PALSAR data. *Geophysical Research Letters*, *35*(12).

Rignot, E., & Kanagaratnam, P. (2006). Changes in the velocity structure of the Greenland Ice Sheet. *Science*, *311*(5763), 986-990.

Rott, H., Müller, F., Nagler, T., & Floricioiu, D. (2011). The imbalance of glaciers after disintegration of Larsen-B ice shelf, Antarctic Peninsula. *The Cryosphere*, *5*(1), 125.

Scambos, T. A., Hulbe, C., Fahnestock, M., & Bohlander, J. (2000). The link between climate warming and break-up of ice shelves in the Antarctic Peninsula. *Journal of Glaciology*, *46*(154), 516-530.

Scambos, T. A., Bohlander, J. A., Shuman, C. U., & Skvarca, P. (2004). Glacier acceleration and thinning after ice shelf collapse in the Larsen B embayment, Antarctica. *Geophysical Research Letters*, *31*(18).

Scambos, T. A., Haran, T. M., Fahnestock, M. A., Painter, T. H., & Bohlander, J. (2007). MODIS-based Mosaic of Antarctica (MOA) data sets: Continent-wide surface morphology and snow grain size. *Remote Sensing of Environment*, *111*(2), 242-257.

Schaepman-Strub, G., Schaepman, M. E., Painter, T. H., Dangel, S., & Martonchik, J. V. (2006). Reflectance quantities in optical remote sensing—Definitions and case studies. *Remote sensing of environment*, *103*(1), 27-42.

Schutz, B. E., Zwally, H. J., Shuman, C. A., Hancock, D., & DiMarzio, J. P. (2005). Overview of the ICESat mission. *Geophysical Research Letters*, *32*(21).

Seigman, A. E. (1986) *Lasers*, University Science Books, USA.

Sergent, C., Chevrand, P., Lafeuille, J., & Marbouty, D. (1987). Caractérisation
optique de différents types de neige. extinction de la lumiere dans la neige. *Le Journal de Physique Colloques*, *48*(C1), C1-361.

Shepherd, A., Ivins, E. R., Geruo, A., Barletta, V. R., Bentley, M. J., Bettadpur, S., ...
& Zwally, H. J. (2012). A reconciled estimate of ice-sheet mass
balance. *Science*, *338*(6111), 1183-1189.

Skiles, S. M., & Painter, T. (2017). Daily evolution in dust and black carbon content,
snow grain size, and snow albedo during snowmelt, Rocky Mountains,
Colorado. *Journal of Glaciology*, *63*(237), 118-132.

Smith, D. E., Zuber, M. T., Jackson, G. B., Cavanaugh, J. F., Neumann, G. A., Riris,
H., ... & Katz, R. B. (2010). The lunar orbiter laser altimeter investigation on the
lunar reconnaissance orbiter mission. *Space science reviews*, *150*(1-4), 209-241.

Takeuchi, N. (2009). Temporal and spatial variations in spectral reflectance and
characteristics of surface dust on Gulkana Glacier, Alaska Range. *Journal of Glaciology*, *55*(192), 701-709.

Taylor, J. R. (1997) An Introduction to Error Analysis: The Study of Uncertainties in
Physical Measurements, 2nd ed. University Science Books, USA.

van den Broeke, M., Bamber, J., Ettema, J., Rignot, E., Schrama, E., van de Berg, W.
J., ... & Wouters, B. (2009). Partitioning recent Greenland mass
loss. *science*, *326*(5955), 984-986.

Wang, X., Doherty, S. J., & Huang, J. (2013). Black carbon and other light-absorbing
impurities in snow across Northern China. *Journal of Geophysical Research:
Atmospheres*, *118*(3), 1471-1492.

Warren, S. G. (1982). Optical properties of snow. *Reviews of Geophysics*, *20*(1), 67-
89.

Warren, S. G., & Wiscombe, W. J. (1980). A model for the spectral albedo of snow.
II: Snow containing atmospheric aerosols. *Journal of the Atmospheric
Sciences*, *37*(12), 2734-2745.

Warren, S. G., Brandt, R. E., & Grenfell, T. C. (2006). Visible and near-ultraviolet
absorption spectrum of ice from transmission of solar radiation into snow. *Applied
optics*, *45*(21), 5320-5334.

Wiscombe, W. J., & Warren, S. G. (1980). A model for the spectral albedo of snow. I: Pure snow. *Journal of the Atmospheric Sciences*, *37*(12), 2712-2733.

Young, D. A., Lindzey, L. E., Blankenship, D. D., Greenbaum, J. S., Garcia De Gorordo, A., Kempf, S. D., Roberts, J. L., Warner, R. C., Van Ommen, T., Siegert, M. J., & Le Meur, E. (2015). Land-ice elevation changes from photon-counting swath altimetry: first applications over the Antarctic ice sheet. *Journal of Glaciology*, *61*(225), 17-28.

Zwally, H. J., Jun, L. I., Brenner, A. C., Beckley, M., Cornejo, H. G., DiMarzio, J., ... & Donghui, Y. I. (2011). Greenland ice sheet mass balance: distribution of increased mass loss with climate warming; 2003–07 versus 1992–2002. *Journal of Glaciology*, *57*(201), 88-102.

Curriculum Vitae

Name: Adam P. Greeley

Date: December 20, 2017

Education

B.S.: Atmospheric and Oceanic Sciences, Stony Brook University, 2009

M.A.: Climate and Society, Columbia University, 2010

M.S.: Atmospheric and Oceanic Science, University of Maryland, 2015

Ph.D.: Atmospheric and Oceanic Science, University of Maryland, 2017

Dissertation Title: Estimating surface elevation biases from subsurface scattered photons for laser altimeters

Publications

Ruane, A.C., Cecil, L.M., Horton, R.M., Gordon, R., McCollum R., Brown, D., Killough, B., Goldberg, R., **Greeley, A.P.**, & Rosenzweig, C. (2013). Climate change impact uncertainties for maize in Panama: Farm information, climate projections, and yield sensitivities. *Agr. Forest Meterol.*, 170, 132-145.